PROTON INDUCED REACTIONS ON LIGHT NUCLEI

BY

P.M. PORTNER

Physics Department:
Ph.D. Degree

ABSTRACT

A particle identification system consisting of a 14^{o} uniform field sector magnet, a momentum defining slit and a plastic detector telescope has been used to study the reactions: $^{6}Li(p,p')^{6}Li$, $^{7}Li(p,p')^{7}Li$, $^{6}Li(p,d)^{5}Li$, $^{7}Li(p,t)^{5}Li$, $^{6}Li(p,t)^{4}Li$, $^{4}He(p,p')^{4}He^{*}$, $^{4}He(p,d)^{3}He$ and $^{4}He(p,t)2p$. The angular distributions for elastic scattering from ^{6}Li and ^{7}Li were fitted with an optical model analysis. The ground state transitions for the two-neutron pick-up reactions were compared with a preliminary DWBA analysis. The $^{6}Li(p,t)^{4}Li$ reaction provided new, although inconclusive, evidence for an unbound ground state in ^{4}Li. The results of the pick-up reactions were discussed within the framework of the LS coupling shell model and the Cluster Model. A search for unbound levels in ^{3}He and ^{4}He yielded negative results for ^{3}He and only the broad 22 MeV level in ^{4}He was observed. Investigation of the $^{4}He(p,t)2p$ reaction indicated a strong final state interaction between the two protons, at small angles.

PROTON INDUCED REACTIONS ON LIGHT NUCLEI

by

Peer M. Portner

A thesis submitted to the Faculty of Graduate Studies and Research in partial fulfilment of the requirements for the degree of Doctor of Philosophy.

Foster Radiation Laboratory
McGill University
Montreal.

November 1967

ABSTRACT

A particle identification system consisting of a 14^o uniform field sector magnet, a momentum defining slit and a plastic counter telescope has been used to study several reactions induced by 100 MeV protons on light nuclei.

Elastic and inelastic scattering from ^{6}Li and ^{7}Li has been studied over a large angular range and the elastic scattering fitted with an Optical Model Analysis. One and two-neutron pick-up reactions were studied with ^{6}Li and ^{7}Li. Angular distributions for the ground state transitions were obtained for the reactions: ^{7}Li(p,t)^{5}Li, ^{6}Li(p,d)^{5}Li and ^{6}Li(p,t)^{4}Li, and the distributions for the (p,t) reactions were compared with a preliminary DWBA analysis. The ^{6}Li(p,t)^{4}Li reaction provided new, although, inconclusive evidence for the existence of an unbound ground state in ^{4}Li. The strong excitation of the 16.65 MeV level in ^{5}Li was observed via the ^{6}Li(p,d)^{5}Li reaction but not via the (p,t) reaction on ^{7}Li. The results were discussed within the framework of the L-S coupling shell model and the cluster model.

The existence of unbound levels in ^{4}He and ^{3}He was investigated by a study of inelastic scattering and the deuteron pick-up reaction on ^{4}He. Only the broad 22 MeV level in ^{4}He was observed and no evidence was found for excited states in ^{3}He. The ^{4}He(p,t)2p reaction has been studied and a strong final state interaction between the two protons observed at small angles.

ACKNOWLEDGEMENTS

The author wishes to thank Professor R. B. Moore for his encouragement and assistance while directing this work.

The continued interest and many valuable suggestions of Professor R. E. Bell, Director of the Foster Radiation Laboratory, are gratefully acknowledged.

The author expresses his appreciation to Dr. S. K. Mark for many illuminating discussions and for his encouragement.

Dr. J. C. Hardy is thanked for the preliminary DWBA analysis of some of the data in this work.

Thanks are also due to Dr. J. E. Crawford and Mr. K.S. Kuchela for helpful discussions concerning electronics.

Mr. J. E. Traynor of the Eaton Electronics Research Laboratory is acknowledged for co-operation in providing a liquid helium supply when needed.

Mr. S. Doig, foreman of the machine shop, is thanked for his ready co-operation, Mr. G. Belley for his excellent work on the helium cryogenic target and Mr. S. Smith for his construction of the scattering chamber.

Mr. D. Tam is thanked for his willing assistance.

Finally, financial assistance provided by the laboratory on behalf of the Atomic Energy Control Board of Canada is gratefully acknowledged.

TABLE OF CONTENTS

LIST OF ILLUSTRATIONS

LIST OF TABLES

CHAPTER 1. INTRODUCTION

1.1 Background:

A complete understanding of the theory of nuclear reactions would involve the solution of the nuclear many body problem and this is still far from being achieved (To61). Two models which have been particularly successful in describing nuclear reactions are the compound nucleus model and the direct interaction model. The first model, due to Bohr (Bo36), assumes the capture of the incident particle by the target nucleus into a metastable state and the subsequent decay of the compound nucleus through one of many channels into the reaction products. On the other hand, the direct interaction model, as its name implies, involves a one step reaction mechanism where no intermediate state occurs. Austern (Au60) has defined a direct interaction process as one which involves only a few degrees of freedom of the nuclear system.

The compound nucleus treatment of nuclear reactions is most appropriate for low energies (say 10 MeV and lower). In the energy region considered in the experimental work that follows, the direct interaction description of the reaction mechanism is dominant. One of the distinctive features of the direct reaction is the strong angular dependence of the cross-section, which is usually characteristic of the specific mechanism involved in the reaction.

In recent years much experimental and theoretical attention has been focussed on direct reactions induced by particle (especially proton)beams of intermediate energies (in the region of 100 MeV to several hundred MeV). These reactions often exhibit very simple features and have provided much valuable information in the study of nuclear structure. In nucleon induced reactions at these energies the wavelength of the incident nucleon becomes comparable with and smaller than the average spacing between nucleons in a nucleus (Serber Se47) and thus the incident nucleon will frequently interact with only one nucleon in the nucleus at a time.

Probably the most thoroughly investigated, both experimentally and theoretically, of these direct reaction processes is elastic and inelastic scattering from nuclei. Elastic scattering gives information on the general properties of the nuclear ground state and in particular examines the nucleon distribution within the nucleus. Inelastic scattering provides spectroscopic information about nuclear states and is particularly useful in the study of collective states. Experimentally, the techniques for studying elastic and inelastic scattering of protons have improved considerably from the earlier work done at Harvard by Strauch and co-workers (St56) using a range telescope which limited observation to gross structure in the spectra. Present work at Orsay (Ja64) and Uppsala (Ha65) with high resolution is providing much information on the excitation of individual levels in the residual nuclei.

Another direct reaction which has received a great deal of attention is the pick-up reaction (and its time reversal: the stripping reaction) in which the reaction mechanism involves the transfer of one or more nucleons between the incident particle and the target nucleus.

Single neutron pick-up reactions were first observed by Hadley and York (Ha50) and Selove (Se56). Since the first pick-up experiments, much spectroscopic information has been obtained from the study and analysis of these reactions. Much of the early work done at low energies was analysed successfully using plane wave (Butler) theory (Bu57) in which distortion of the incoming and outgoing waves was neglected. At higher energies where the Butler analysis fails to correctly predict the experimental results, the distorted wave Born approximation (Sa64a) has been successfully used to analyse pick-up and stripping reactions. Two nucleon transfer reactions such as the (p,t) pick-up reaction, have several additional interesting features. Nuclei and levels not easily studied by other means can be excited (Gr65). Levels having two nucleons excited can also be formed, a process which to first order cannot be achieved by either single nucleon transfer or inelastic scattering. In both one and two-nucleon transfer reactions, the angular distributions are characterized by the orbital angular momentum transferred. In single-nucleon transfer, the reaction cross-section is proportional to the probability that the nucleon transferred has the particular angular momentum in the nucleus. In the two-nucleon transfer the angular momentum is carried by the nucleon pair and in general many different configurations of the two nucleons can contribute, (Gl65). Finally the two nucleon transfer reactions such as the (p,t) reaction will be enhanced by collective effects, like nucleon pairing. If a complete two-nucleon transfer reaction theory were available, including both finite-range two-body forces and finite-size triton, the cross-sections would provide information about the short range spatial and momentum correlations of nucleon pairs (neutron pairs in the case of p,t) in the target ground state (Ba64). Very little experimental work has been reported for two nucleon transfer reactions in the 100 MeV energy region, and in general very little data exists for these reactions on light nuclei. (p,t) reactions on several light nuclei have been studied by the Orsay group at 156 MeV (Ba66, Ba65). At lower energies both (p,t) and (p,^{3}He) reactions have been investigated at 44 MeV by Cerny et al (Ce66). Single nucleon pick-up reactions, such as the (p,d) reaction have been studied quite extensively and summaries of recent experiments have been given by Mark (Ma65) and Lee (Le65).

Two of the main experimental limitations in the study of nuclear reactions are the finite energy spread of the particle beam and the intrinsic resolution of the detector system. Reaction studies with the McGill Synchrocyclotron (and in fact most other synchrocyclotrons) are generally limited to light nuclei where the level spacing is sufficiently great to allow identification of individual levels of the residual nucleus. The work reported here is a natural continuation of earlier reaction studies made by Lee (Le65) and in collaboration with Mark (Ma65). The reactions studied were ^{6}Li(p,p')^{6}Li, ^{7}Li(p,p')^{7}Li, ^{7}Li(p,t)^{5}Li, ^{6}Li(p,d)^{5}Li, ^{6}Li(p,t)^{4}Li, ^{4}He(p,p')^{4}He*, ^{4}He(p,d)^{3}He*, and ^{4}He(p,t)2p. Light nuclei were chosen because of the resolution limitation previously mentioned and also in the hope that interpretation of the results would be simplified by having few nucleon systems. Elastic scattering from ^{6}Li and ^{7}Li was done primarily to provide optical model parameters for the DWBA analyses of the pick-up data for the two lithium isotopes. The $^{6}Li(p,t)^{4}Li$ reaction and the inelastic scattering from ^{4}He were of particular interest because of the continued investigation both experimental and theoretical, of the four nucleon system (Ja67, Mf65). The study of final state interactions has also been the subject of a great deal of interest in recent years because of the information on the two-body interaction which can be extracted (Oe67) from reactions such as the $^{4}He(p,t)2p$ reaction investigated here.

1.2 Experimental Method:

The problem of identifying charged particles from a nuclear reaction is basic to all reaction studies. A number of different techniques have been used of which the most common are:

a) Magnet analysis using large spectrometers. This technique has, at least at high energies, provided the best energy resolutions (Ha65) although its disadvantages include: small solid angle, complications involved in obtaining an energy spectrum and the large size and cost of the installation for beams of energies of 100 MeV or more.

b) Range telescope techniques, which by measuring both the energy and rate of ionization of a particle allow identification within a limited range of energies. and,

c) Electronic identification systems which utilize pulses from ΔE and E counters in a counter telescope to generate an analog function which is characteristic of the particle species. These methods use empirical range-energy relationships; typical examples are the logarithmic function generator of Goulding et al (Go64, Go66) and the multiplication method of Mark (Ma65, Ma66a).

Method (a) is impractical for this laboratory; however the technique which was used did employ magnetic selection. The identification system selected for this work consisted of a 14^{o} uniform field sector magnet which together with a slit preceding the magnet defined a range of particle momenta. The detector was a two element plastic counter telescope. Final particle identification was achieved by ΔE discrimination. The magnet analyser has already been described by Lee (Le65). Modifications made to improve its performance and a detailed analysis of its properties are given in a subsequent chapter. The identification system was chosen over the method (c) described above (which has been used in this laboratory by Mark (Ma65)) for two main reasons: the inherent separation of particle species is superior to method (c) over a limited (about 20 MeV) energy range, and even more important the counter telescope sees only the particles of interest (with some small feed-through of other species) and is not, therefore, subject to counting rate limitations imposed by high cross-section competing reactions. Plastic scintillators were chosen for their fast response since for most of the reactions studied, the resolution was not critical.

CHAPTER 2. APPARATUS AND EXPERIMENTAL METHOD

2.1 General Experimental Set-Up:

The experiment was performed using the external beam facility of the McGill Synchrocyclotron. A schematic diagram of the beam transport system showing only those features pertinent to this experiment is provided by fig. 1. The beam energy is $100.3 \pm .2$ MeV with the cyclotron magnet current at 640 amps and the energy spread is about 0.4 MeV. The phase space area of the entire extracted beam is about 2 to 5 cm-milli radians both horizontally and vertically, the maximum beam current being about 50 nAmps. By collimating the beam to a few nanoamps with the horizontal and vertical beam defining slits (shown in fig. 1) very good beam quality in the experimental area is possible, allowing small spot size at a target as well as small divergence. The proton duty cycle is low, the beam having a pulsed structure of approximately 10μsec bursts at a repetition rate of 400 sec^{-1}, and in addition an R.F. fine structure of 10 nsec wide pulses 46 nsec apart. This factor was an important consideration leading to the choice of plastic scintillators for the detectors in this experiment, as instantaneous counting rates were more than two orders of magnitude higher than the average observed rates. The beam transport system itself consists of three bending magnets, the first two directing the beam into the experimental beam hall and the third steering the beam to the various experiments, and two quadrupole doublets for beam focussing. Two viewing boxes containing remotely controlled zinc sulphide fluorescent screens, and a closed circuit television system facilitated aligning and focussing the beam. A more detailed description of the system has been given elsewhere. (Po64)

The experimental system, itself, consisted of: a scattering chamber mounted on a post, and directly connected to the external beam system; an "analyser" magnet and counter telescope which served as the particle selection and detecting system and was pivoted about the scattering chamber post; a Faraday cup some two meters downstream from the target; and a monitor counter telescope which was also pivoted about the scattering chamber post. A schematic diagram of the experimental layout is shown in fig 2 and a photograph in fig 3. Each part of the experimental system is described in some detail in the following sections.

2.2 Scattering Chamber:

The scattering chamber was basically an aluminum cylinder 40 cm in diameter and 20 cm deep. A thin window 3.8 cm high extended to a scattering angle of about 110 degrees on each side of the beam line. In the early stages of the experiment 0.05 mm thick mylar was used for the window. However, it was found that radiation damage produced by the unscattered beam leaving the chamber made the mylar extremely brittle, the resultant loss of strength and flexibility necessitating frequent window changes due to failure at the weakened spot. This occurred after doses of the order of 10^{15} protons/cm^2 (occasionally reached in a single long run). The solution simply involved changing the window material to H-film, a polyamide (chemical composition $(C_{22}\,H_{10}\,N_2\,O_4)_n$) made by E. I. Du Pont de Nemours and Co., with texture and mechanical properties very similar to those of mylar but considerably more radiation resistant. Tests performed with the Harvard cyclotron (Ko65) indicated that H-film was at least 10 times less sensitive to radiation damage than mylar. Over the course of this experiment it was found necessary to change the 0.05 mm thick H-film window only once and this was for a reason unrelated to radiation damage. A very rough estimation of the total dose accumulated by the H-film during the experiment indicates that H-film is at least a factor of 50 times less sensitive than mylar to proton irradiation.

The proton beam entered the scattering chamber through a 3.8 cm port in the front of the chamber. For measurements at the backward angles, beyond the extent of the chamber window, the scattering chamber was rotated on its support post through 180° and the entry port (now exit) and beam pipe were covered with 0.025 mm thick H-film windows to maintain the vacuum. Relative scattering angles were marked off on the base circumference of the scattering chamber in one degree steps with milling table precision. A target holder was designed which could accomodate four targets, (insert fig 2) and could be rotated to any angle with respect to the incident beam. One of the target positions contained a fluorescent screen which was used in conjunction with the closed circuit television to align the proton beam at the target centre. Usually the other three target positions contained a carbon (or sometimes CH) target for calibration purposes and targets of ^{6}Li and ^{7}Li. The entire target assembly could be removed, the chamber adapting easily to the use of the liquid helium cryogenic target, which is described in a later section. During the experiments with the liquid helium target, the scattering chamber was provided with its own independent vacuum system and separated from the external beam system by a 0.025 mm H-film window. This allowed the realization of pressures in the scattering chamber of 10^{-6} mm of Hg; at least an order of magnitude lower than those obtained with the main vacuum system, and of some importance in minimizing helium losses due to gas conduction.

2.3 Analyser Magnet:

a) Preamble:

The basic analyser magnet, used in this experiment, and its design as a "crude" particle separator has been discussed by Lee (Le65), and for the sake of completeness, a summary of the theory of operation is presented in Appendix I. A number of modifications and improvements have been made to the system, extending its performance and reliability, and a comprehensive analysis made of its particle separation properties. The following sections describe the physical set up of the analyser magnet system, analysis of its design properties, and its alignment and calibration.

b) Physical Set Up:

The analyser magnet system consisted basically of a wedge magnet preceded by a momentum defining slit and followed by a counter telescope. The set up is shown schematically in fig. 2. and in more detail, in the photograph of fig. 3. The C-Frame magnet had special pole tips, designed for a 14° deflection with normal entry and exit. The pole tip assembly was fixed relative to the main yoke of the magnet by means of an aluminum table which also served as a support for the counter telescope and lead shielding and greatly facilitated alignment. A vacuum chamber in the 3 cm pole gap extended from a distance of 10 cm from the scattering chamber window to the counter telescope, minimizing the energy degradation and multiple scattering of detected particles. This vacuum chamber had entry and exit windows of 0.013 mm mylar and was maintained at a pressure of a few microns. A new adjustable momentum defining slit located about 2.5 cm before the entry pole face and an additional vertical limiting slit were incorporated into the magnet vacuum chamber. Both slits were thick enough to completely stop the most energetic particles. The vertical slit at the chamber entrance had an aperture of 1.3 cm and reduced scattering from the walls of the vacuum chamber. The magnet was supported on a table which in turn was pivoted on wheels about the scattering chamber post. A pointer attached to the magnet carriage and an angular scale marked on the floor allowed selection of the scattering angle to an accuracy of about 0.1°. The power supply for the magnet used a motor generator set with series regulation.

c) Magnet Separation Properties:

Analysis of the magnet properties followed the general format described by Lee and outlined in Appendix I, with one major difference: Lee's analysis assumed a path from the target to the detector consisting of a drift space (zero magnetic field) followed by a well defined uniform field region and then another drift space, and making no allowance for fringing field effects. A better analysis requires either the use of an "effective" field region; the usual approximation being to extend the uniform field region by a distance equal to one pole gap width on each side, or; treatment of the fringing field on the same basis as the uniform field region. The second alternative was chosen although comparison with the first yielded similar results.

The magnetic field was mapped along the central path from the target to the detector over the entire range of magnetic excitation, using a Hall probe. The field shape was found to be constant, within measurement errors, over the whole useful range, saturation producing distortion in the shape only at excitations higher than the maximum required. The absolute field, and in fact uniformity of the field, are not important considerations and no effort was therefore made to obtain anything but a relative field shape. The field shape is shown in fig. 4 and the fringing field is quite evident. The effective transfer matrix for the path from the target, through the magnet and to the detector, was then obtained by dividing the path into small segments, calculating a matrix for each segment and multiplying all these matrices together. The modifications to the derivations of Appendix I introduced by this method are presented in Appendix II, and the resulting momentum selection characteristics for the analyser magnet system are summarized in the graph of fig 5. The curves S_{max} and S_{min} represent, for any particular momentum defined by $\Delta p/p$, the limits at the slit position for particles originating from the beam spot at the target and reaching the detector. As can be seen from the diagram, the effect of introducing a slit at the slit position is to define a range of momenta for which particles will be transmitted. Also illustrated in fig. 5 is the effect of the finite beam spot size on the transmission characteristics of the system. The necessity of a small beam spot to ensure the maximum range of total transmission is readily evident. The slit width used throughout most of this experiment was 15 mm. The momentum "bite" selected in this way corresponds to a fixed range of magnetic rigidities and different energy "bites" for different particles. An example of the particle separation afforded by this momentum selection is shown in fig. 6 where the transmission is plotted for magnet settings corresponding to a central path rigidity for 90 MeV protons, 80 MeV deuterons and 70 MeV tritons respectively. Similar curves for ^{3}He particles and alphas were also obtained but are not shown here. Finally, since the transmitted momentum range $\Delta p/p$ is determined by the geometry and is therefore a constant of the system, the size of the selected energy range (fully transmitted) varies with energy of the particle (and slightly with particle species). This is shown in fig. 7 for several beam spot sizes, again illustrating the strong effect of spot size on transmission. The beam spot size was a particularly important factor in determining the transmission in the experiments with the liquid helium target due to its extended size. The finite width of the lines in fig. 7 are indicative of the small differences in transmission for the different particles.

d) Alignment and Calibration:

The magnet was initially aligned with a theodolite to ensure that the magnet gap was in the horizontal plane and centered vertically on the target centre. Final alignment was made with the beam itself, using fluorescent screens and closed circuit television. Horizontal and vertical alignment were checked, as well as was the normal entry to the pole tip (with the magnet vacuum chamber removed).

The absolute calibration of the analyser magnet was achieved in the following way. The momentum defining slit was set to $\pm$ 1 mm and a 3 mm wide (horizontally defining) slit was placed in front of the counter telescope (to be described in the following section). Using a target of Naton 136 scintillator (composition $CH_{.997}$), the magnet was adjusted to select the protons elastically scattered from the hydrogen content of the target. This was repeated at several scattering angles, and the scattered proton energies calculated from the proton-proton kinematics. When setting the magnet the current was always cycled to minimize variations due to hysteresis effects. Additional proton calibration points were obtained from elastic and inelastic scattering off carbon. A deuteron calibration point was obtained from the $^{12}C(p,d)\,^{11}C$ reaction, the magnet setting being adjusted to accept the ground state deuterons. These calibrations were extended by calculation to tritons, alphas, and ^{3}He's and the final energy calibration thus obtained is shown in fig. 8. This empirical calibration was in good agreement with calculations based on the known trajectory and rough measurements of the magnetic field. Later careful measurements with tritons from the $^{7}Li(p, t)^{5}Li$ reaction were consistent with the calculated triton calibration.

Finally the size of the energy "bite" plotted in fig. 7 was checked experimentally, again using the CH target. The transmissions for elastically scattered protons from the $^{12}C(p,p)$ and $^{1}H(p,p)$ reactions were simultaneously measured as a function of the magnet setting. Spectra were accumulated with the counter telescope and peak areas were extracted for the two groups of elastic protons at each magnet setting. Relative normalization was obtained by counting for the same unit of incident beam. This was done at a scattering angle of 30° lab. where the two groups of protons differ in energy by 23.7 ± .6 MeV (the uncertainty arising from the angular uncertainty). The regions of total transmission for the two proton groups did not quite overlap and this is consistent with a value of 21 MeV obtained from fig. 7 for a 1mm beam spot and the appropriate magnet setting.

2.4 Counter Telescope:

a) Detector geometry:

The detector was a simple two counter telescope consisting of a brass collimator followed by a dE/dx (ΔE) counter and an E counter. The main function of the collimator which was located 6 cm in front of the ΔE counter was to limit the counting rate in the E counter whose cross-sectional area was several times the shadow of the ΔE counter. The collimator dimensions (width and height) were 0.8mm larger than those of the ΔE scintillator.

The ΔE counter was a scintillator of NE 102, 1.2 cm wide, 1.9 cm high and of variable thickness mounted in a reflector in the shape of a truncated cone (see fig. 9), and viewed on edge by a Phillips 56 AVP photomultiplier. The thickness of the ΔE scintillator was chosen so that the detected particle would lose about 1.5 MeV in passing through it, this providing adequate pulse height resolution. Typically, a thickness of 2 mm was used for protons and 1 mm for deuterons and tritons. The ΔE scintillator also defined the solid angle. The total energy (E) counter was a 3.8 cm diameter, 9 cm long cylinder of NE 102 plastic optically coupled with an epoxy cement (Epon 812) to an RCA 8575 photomultiplier.

b) Magnetic Shielding:

Due to the close proximity of the counter telescope to the Analyser magnet, necessitated both by space limitations and the desired characteristics of the magnet separation system, both photomultipliers were subjected to fields of several tens of gauss. An adequate magnetic shield was obtained with single concentric layers of netic and conetic high mu magnetic shielding (Magnetic Shield Division, Perfection Mica Co) enclosed in a 6 mm wall iron pipe extending to about 4 cm beyond the photocathodes. A small variation in pulse height was observed in the E counter when rotated about its axis and the counter fixed in the orientation producing maximum pulse height. No such variation was observed for the ΔE counter which was parallel to the field. During the course of the experiment the effect of the fringing field on the pulse height and pulse height resolution was found to be negligible.

c) Counter Alignment:

Initially the position of the counter telescope was determined with the magnet aligned in the direct incident beam (i.e. at 0^{o} scattering angle). This was accomplished by mapping the trajectory of the beam along the central (design) path using a fluorescent screen and closed circuit television. Vertical alignment was checked with a theodolite to ensure that the centres of the target, magnet gap and counter telescope were aligned to within about 0.5 mm. Alignment of the axis of the telescope in the direction of the central path was achieved with the magnet set at an arbitrary scattering angle of 15^{o}. The slit at the entrance to the magnet was set at $\pm$ 1 mm with respect to the central path and a vertical slit 3 mm wide was placed in front of the E counter which was withdrawn to a distance of about 12 cm from the ΔE scintillator. Protons, elastically scattered from a carbon target (identified by the pulse height spectrum from the E counter) were swept across the counter telescope by varying the magnet excitation, and the counting rates of both counters obtained as a function of magnet setting. This provided a simultaneous profile of the width of the ΔE scintillator and the vertical slit centered in front of the E counter. Correct alignment was then simply obtained by ensuring that the centroids of these profiles coincided. Vertical alignment was quite critical due to the limited aperture of the magnet and the desire to obtain the maximum possible solid angle for the detector while at the same time minimizing kinematic spread. Consequently, a final, more stringent test of the vertical alignment was made by accurately measuring the cross section for elastic scattering with different vertical slices of the ΔE scintillator. This was done by using a scintillator of the same width as the standard ΔE scintillator, but of one third its height. The smaller scintillator was successively mounted at different vertical positions in the reflector, corresponding to the top, centre, and bottom, of the standard ΔE, and in each position the relative cross sections accurately measured. The three cross - sections obtained in this way and the cross section obtained with the standard ΔE were found to be the same within statistical errors.

d) Pulse Height Resolution:

The main limitation in the pulse height resolution of the ΔE counter was due to the Landau spread. The light reflector (fig. 9) with the free mounting of the ΔE scintillator was found to give substantially better light collection efficiency than more conventional light guides. It was also found that the light output (pulse height) was slightly higher for a rough, or diffuse surface than for a polished scintillator. The most probable explanation for this is a reduction in the number of internal reflections and therefore reduction of light losses due to self absorption.

Some time was spent in optimizing the energy resolution of the E counter since this is a very important criterion in such a detector. The best previously reported resolution for the detection of intermediate energy protons with plastic scintillators was 1.6 MeV at 100 MeV (Ma65, Ma66). A more typical figure would be of the order of 2%. A very rough estimate of the possible resolution obtainable with a counter using a plastic scintillator such as NE 102 gives a value of about 0.6%. This estimate uses a value of 3 detectable photons per keV energy loss in the scintillator (Ri61) and a photocathode efficiency of 10% for the photomultiplier. The estimate also assumes that the only significant contribution to the resolution is photoelectron statistics, which is a reasonable assumption for a scintillator used in a scattering experiment, where the variation in light collection is minimized by localization of the detected particles (Be66). A systematic improvement of the energy resolution resulted in a final resolution of 1.04% in the direct 100 MeV proton beam. This is only slightly inferior to resolutions previously obtained at this laboratory with the NaI(TL) counters. The main factors contributing to this improvement were: good light collection efficiency, selection of the photomultiplier and a fairly strongly tapered dynode chain. Light collection efficiency was improved quite considerably by using a truncated-cone-shaped scintillator with a diffuse reflector of TiO_2 paint (Nuclear Enterprises NE560) on the sides. The front face of the scintillator had a reflector of aluminum foil.

The E counter finally used in the detector telescope had a cylindrical scintillator, since a truncated cone would have considerably limited the solid angle. The overall resolution for the entire system, obtained during the experiment was typically 1.3% for protons, 1.6% for deuterons and 2.2% for tritons. This includes contributions from the beam spread (about 0.4 MeV - Po64), kinematic broadening due to finite detector size, energy straggling in the target, windows and ΔE counter, and the electronics. The inferior resolution obtained with deuterons and tritons is primarily due to the intrinsically lower light output from plastic scintillators for heavier charged particles (Go60) although the increased straggle due to greater energy losses in the target, windows and ΔE scintillator also contributed. In fact the light output for alphas and ^{3}He particles is of the order of 40% of that for protons and this, together with their high rate of energy loss, made the present system quite unsuitable for their detection. Finally, provision was made for electronically adding back the energy lost in the ΔE scintillator to the E counter, however, the improvement in resolution was very small and so generally this was not done.

e) Signals:

Fast timing pulses were fed directly into 50 ohm cables from the anodes of both the E and ΔE counters and clipped to 8 nsec. at the anode. Linear information pulses were obtained from the 10th dynode for the E counter (RCA 8575) and the 12th dynode for the ΔE counter (Phillips 56AVP), using White cathode followers to drive 50 ohm cables. The duration of the information pulses was kept reasonably short (about 60 nsec.) to minimize pile up at high counting rates.

f) Photomultiplier Supply Voltages:

The supply voltage for the ΔE photomultiplier was determined using protons scattered off a carbon target at a small angle (10°): high energy protons producing the smallest ΔE pulses. The voltage was increased in steps and the usual plateau of counting rate as a function of phototube H.T. was obtained, with the ΔE discriminator at its lowest setting (100 mv). The supply voltage was then fixed at a value comfortably in the plateau region but somewhat below the noise threshold, ensuring that all proton pulses were above the minimum discriminator level. The supply voltage for the E counter photomultiplier was chosen while optimizing the pulse height resolution, to provide good pulse height, at the same time maintaining linearity of the dynode information pulses.

g) Pulse Height Linearity and Calibration:

The pulse height linearity of the E counter was checked for protons, deuterons and tritons by using absorbers of various thicknesses in front of the telescope. The differential linearity over the energy region of interest was better than 2% which was adequate. Energy calibrations obtained during the course of the experiment from the kinematic variation of particle energy with scattering angle provided an independent check of the pulse height linearity which was in good agreement with the range method.

h) Angular Resolution:

The contribution to the angular resolution due to the finite detector size was 0.6 degrees. Other contributions to the angular resolution will be discussed in another section.

2.5 Beam Monitor:

a) Faraday Cup:

The primary beam monitor was a Faraday Cup located about six feet downstream of the target (see fig. 2) to avoid interfering with the magnet at small scattering angles and to reduce background in the vicinity of the counters. The cup itself was a 9 cm diameter brass cylinder supported in teflon insulators inside an outer evacuated cylinder which served as a grounded shield. The cup was deep to minimize losses due to back scattering of electrons, and was made with a detachable bottom containing a plexiglas beam stopper to reduce neutron background. A self contained independent vacuum system with a diffusion pump backed by a mechanical pump maintained the pressure in the cup at 10^{-5} mm Hg thereby ensuring negligible errors due to the ionization of residual gas in the cup. A bias ring was provided at the cup entrance for electron suppression, but tests with voltages up to $\pm$ 500 volts showed no observable effects. To avoid collection of electrons ejected from the thin front window (0.5 mm aluminum), the window was separated from the cup entrance by about 20 cm and permanent bar magnets provided a sufficiently strong magnetic field to deflect the most energetic electrons. The entire cup was shielded from the counter telescopes with lead to reduce gamma backgrounds. A fluorescent screen on the front window allowed periodic checks of cup alignment. Initial alignment of the faraday cup on the beam was made with the back removed. Typically the beam spot at the cup entrance was about 2.5 cm in diameter, the size being due to divergence of the beam and multiple scattering in the target, chamber window and air path.

b) Calibration Faraday Cup:

A second Faraday Cup (whose back could be withdrawn and inserted remotely) was designed and installed in the external beam system just upstream of the second viewbox (see fig. 1). This cup possessed all the features incorporated in the main cup for minimization of possible errors in charge collection. The function of this cup was to provide an accurate calibration of the primary cup and thus allow corrections for beam loss after the target. This was an especially important consideration in this experiment partly because of the extended air path to the cup, but also due to small deflections of the unscattered proton beam in the fringing field of the analyser magnet. The calibration procedure required the use of an intermediate monitor for the comparison of the two cups. This was achieved by monitoring the beam intercepted by the horizontal defining slits which were insulated with teflon from their housing. Adequate accuracy could be obtained by taking the mean of several short measurements. A considerable improvement both in convenience and accuracy would have been possible had a transmission monitor such as an ionization chamber been available.

c) Current Integrator:

The current from the Faraday cup was recorded by a commercial micromicro ammeter (EH model 240), and the integrated current measured by feeding the output of the micromicro ammeter into a voltage-to-frequency converter (Hewlett Packard Model 2210) whose output was scaled with a fast counter. This provided a very convenient system for current integration, the main limitation in accuracy being due to drift and noise pick-up in the electrometer. The calibration of this integrator was checked at various times in each run using a Keithley picoampere source (model 261). Absolute calibration was obtained at the beginning and end of the experiment by comparing a known current with the picoampere source. The absolute current was produced by feeding the linear ramp voltage (dv/dt) from a

Tektronics 547 'scope into a precision capacitor providing a current Cdv/dt which could be very accurately determined, (Be66).

d) Monitor Counter Telescope:

At scattering angles smaller than 30°, the Faraday cup could not be used, as the magnet blocked the beam path, making the use of a secondary beam monitor necessary in this angular region. A plastic dE/dx - E counter telescope similar to the main detector telescope and pivoted on an arm about the chamber support post served this purpose. The ΔE scintillator was a 9.5 mm diameter and 1 mm thick disc of NE102 plastic; the brass collimator 11 mm in diameter and the E counter a 9 cm long truncated cone of NE102 plastic scintillator optically coupled to an RCA 6342A photomultiplier. Other physical details and the photomultiplier supply voltage adjustments were the same as in the main counter telescope. The monitor counter was positioned at an angle of 60° on the side of the incident proton beam opposite the magnet. At this angle the fringing field of the analyser magnet was found to have a negligible effect on the monitor counting rate. In this configuration the beam leaving the scattering chamber was stopped in a plexiglas block which was surrounded with lead bricks to provide shielding for the counter telescopes. At angles of 30° and larger both the monitor telescope and the Faraday cup were used to monitor the beam, providing normalization for the monitor.

2.6 Electronics:

A block diagram of the electronic system is shown in fig. 10.

The fast coincidence units, discriminators, and the linear gates were commercial modules manufactured by E. G. & G. Inc. The remainder of the electronics was built by the author, transistorized circuitry being used throughout. A brief description of the system is as follows: fast timing pulses of 8 nsec duration from the anodes of the ΔE and E counters triggered fast discriminators whose standard outputs were used to form the fast coincidence. The coincidence resolving time was determined by adjusting the pulse lengths of the discriminator outputs and was typically 15 nsec. Correct timing of the coincidence inputs was achieved with a standard time delay curve. True and chance coincidences were obtained simultaneously as shown in the diagram; chance coincidences being detected by delaying the ΔE timing pulse by a multiple of the cyclotron RF time structure (usually one RF cycle). Output pulses from the coincidence (true) unit were regenerated by the gate driver which opened the two linear gates allowing the appropriate E and ΔE information pulses through. The gate driver which was basically a fast emitter timing monostable was necessary to provide standard pulses for the linear gates which remained open for the duration of the gating pulse. The output pulse duration from the coincidence units was determined by the overlap of the input pulses and was therefore not only variable but also too short. The gate driver provided a gating pulse for the multichannel analyser. This was required only for two parameter analysis. The amplifier shapers and delay amplifiers shaped the E and ΔE information pulses for the analyser (TMC 4096 channels). The E and ΔE spectra could be routed into separate quadrants of the analyser memory and accumulated simultaneously; or, as will be discussed in a later section, stored in the two parameters mode to aid in particle identification.

The electronics for the monitor telescope was essentially the same as that for the main counter telescope, with the exception that only the timing pulses were used. Fast common base amplifiers of rise time less than 3 nsec and gain of approximately 8 were constructed for the timing pulses from the E counters to provide pulses large enough to trigger the lowest discriminator setting for low energy particles.

The true coincidence and monitor coincidence rates were counted with a fast (100 MHz) dual scaler which was also useful when checking very high singles rates. The chance coincidence rate was scaled with a slower scaler.

2.7 Lithium Targets:

The lithium targets were both enriched separated isotopes obtained in metallic form from Oak Ridge. The ^{6}Li was 99.3% enriched and the ^{7}Li 99.99% enriched. The targets were made by rolling the lithium immersed in mineral oil to thicknesses of approximately 1 mm, (50 to 60 mg/cm^2) and then cutting the targets with a sharp knife to fit the target holder. The thickness was measured with a micrometer gauge, the average of a number of readings providing adequate accuracy ($\pm$ 0.005 mm). The uniformity of the target thickness was surprisingly good and found to always be within the uncertainty of the measured thickness. Several targets were made over the course of the experiment and were stored in mineral oil between runs.

Prior to insertion in the target holder the bulk of the oil was removed with absorbent tissue and the thin film remaining evaporated in the scattering chamber. Very little deterioration of the targets was observed over the entire period in which they were used and it is believed that oxygen and nitrogen contamination was negligible.

2.8 Liquid Helium Target:

a) Description:

Cryogenic targets for liquid gases of varying degrees of sophistication have been described in the literature. The helium target built for this experiment was very simple in design and was modeled on a hydrogen cryostat used at Harvard (Pa58) as was a previous helium target constructed at this laboratory by Goldstein (Go67). Several modifications were incorporated in the design of the present target which resulted in greatly improved performance over previous liquid helium targets.

A diagram of the helium target is shown in fig.11. The essential components of this target were: the helium reservoir and target appendage enclosed within a heat shield which was maintained at liquid nitrogen temperature to minimize heat transfer by radiation, and an outer vacuum jacket to provide thermal insulation.

The materials used in the construction of the cryostat were copper and stainless steel, copper being used where good thermal conductivity was necessary and stainless steel where good insulation was required. All joints were silver soldered to withstand stresses due to the extreme temperatures and to ensure a reliable vacuum tight system. Problems due to differential contraction were minimized by the use of copper and stainless steel whose thermal contractions are almost equal, and by hanging the internal cold structure freely from the outer container which was at room temperature. The use of brass in the cryostat was avoided for several reasons: its thermal contraction is about 20% higher than that of stainless steel; its thermal conductivity at liquid nitrogen temperature is an order of magnitude lower than that of copper (two orders of magnitude at liquid helium temperature) and finally, brass has poor vacuum properties, having a tendency to outgas.

The outer container of stainless steel provided a vacuum environment and support for the target assembly. The lower flange was designed to fit directly into the top of the scattering chamber, replacing the regular target assembly. The liquid nitrogen reservoir which served to cool the radiation shield, was partially thermally insulated by a stainless steel upper section between the reservoir and the copper flange at the top. The heat shield was divided into an upper section which was an integral part of the liquid nitrogen reservoir and extended down below the target flange, and a lower section which could be removed to provide access to the target. Both sections of the heat shield were made of copper with 1.5 mm walls to ensure good thermal conductivity and a uniform low temperature. The lower heat shield was attached to the upper section simply by a tight pressure fit. To present thin windows to the incident beam and scattered particles, a 2.5 cm diameter hole for the incident beam and a 2.5 cm high slot extending 100 degrees to either side of the beam direction for particles scattered from the target, were cut into the lower heat shield and covered with thin (2.3 mg/cm^2) aluminum foil. A two layer baffle at the bottom of the lower heat shield provided a path for pumping on the interior of the cryostat while at the same time providing a continuous radiation shield.

The liquid helium reservoir which had a capacity of 1.6 litres was suspended from the heat shield assembly by its filling tube. This tube was thin walled and of stainless steel to minimize heat transfer by thermal conduction. The temperature gradient and subsequently the thermal conduction was also reduced quite appreciably by extending the length of the filling tube between the points of contact with the liquid helium and liquid nitrogen reservoirs as shown in the diagram.

The helium target itself was attached to the helium reservoir flange, good vacuum being maintained at these low temperatures by the use of an indium vacuum seal. The helium target finger consisted of a 12.7 mm cylinder of 0.025 mm thick H-film with an aluminum flange and end cap, and was assembled with an epoxy using equal parts of Epon 828 resin (Shell Chemical Co.) and Versamid 125 resin (General Mills Inc.). The use of a detachable target finger was very convenient, greatly facilitating replacement, and represents an improvement over previous targets.

Special care was taken when assembling the cryostat to keep the helium reservoir, heat shields and outer container concentric, to ensure correct and reproducible target alignment.

The entire heat shield assembly and the helium reservoir were silver plated and highly polished to minimize heat transfer by thermal radiation. To prevent deterioration due to tarnishing of the polished silver surfaces, the cryostat was always stored under vacuum in a special vacuum chamber.

b) Performance:

Apart from an initial vacuum leak in the liquid nitrogen reservoir which was successfully repaired with epoxy (Epon-Versamid), no problems were encountered with the cryostat. The rate of helium consumption was determined in each run by periodically monitoring the liquid level. The liquid level indicator was a simple device consisting of a long 3 mm o.d. stainless steel tube with a larger o.d. brass reducer section at the top. Its operation makes use of the fact that when the cold end of a tube containing an oscillating gas column passes from the helium vapour into the liquid, the frequency and the intensity of oscillation decrease by about 30 and 60 per cent respectively (Ga55). The liquid level is found by holding the thumb lightly over the end of the tube and recording the point at which an abrupt frequency-intensity change occurs. With care helium levels could be measured to within $\pm$ 1 mm. The helium consumption rate, after correction for evaporation due to the beam itself (typically an average of 2 to 5 cc/hour), was found to be approximately the same in all three runs in which the target was used. The rate of evaporation was observed to decrease with time, the average consumption rate for the first half of the reservoir being about 45 cc/hour;

dropping by about 30 per cent for the lower half. The decrease in consumption rate can be understood qualitatively by the following considerations: As the liquid level in the helium reservoir drops, some of the heat which previously went into evaporation of the liquid, is now absorbed by the saturated helium vapour above the liquid by slightly raising its temperature. The immediate consequence of this heat sharing is a reduced evaporation rate. In fact the specific heat of helium vapour (per $^{\mathrm{o}}$K) at temperatures near the boiling point is somewhat less than a quarter the latent heat of vapourization (Ke42). The overall average consumption rate was 40 cc/hour and this represents a significant improvement over other similar cryostats where typical consumption rates for helium of 250 to 300 cc/hour have been reported (Se58, Go67). More sophisticated systems have been reported with consumption rates as low as 200 cc/hour (Mo64).

It is difficult to explain the large difference in performance quantitatively, but some conclusions of a qualitative nature can be drawn. Goldstein (Go67) has made a detailed analysis of the various sources of heat transfer which contributed to the helium evaporation rate of his cryostat. His analysis was subject to a number of fairly serious arbitrary assumptions; however it is of interest to compare the two cryostats. The sources of heat transfer in the present cryostat, as in Goldstein's, can be divided into two categories: thermal conduction down the filling tube and gas conduction; and thermal radiation both down the filling tube and from the heat shield to the helium reservoir and target appendage. The contributions to the total heat transfer from conduction and from radiation down the filling tube are small; being of the order of a few cc/hour and probably not greater than about 10 cc/hour (Go67). The remainder of the heat transfer can be attributed to radiative transfer from the heat shield, although an accurate analysis is difficult in the absence of a reliable estimate of the emissivity of H-film.

The earlier cryostat used by Goldstein had two additional features which contributed to heat transfer to the target and reservoir. The first was the use of nylon centering screws to position the reservoir, providing a path for thermal conduction from the heat shield. The second was in the design of the lower heat shield which was constructed entirely (except for a silvered brass baffle) of 0.025 mm aluminum foil and was therefore able to support a relatively large temperature gradient, increasing radiation. Goldstein attributed about 70 percent of his evaporation rate to the radiation from the lower heat shield. Earlier cryostats have also used thin aluminum foil heat shields, although the use of centering screws has generally been avoided.

In an attempt to try to isolate the various effects contributing to the heat transfer, and in particular to try to simulate some of the (undesirable) features of the earlier cryostats, two additional tests were performed. The tests were conducted with the cryostat in the same environment as during the actual experimental runs, but without the proton beam. In the first test, the liquid helium consumption rate was measured with a 25.4 mm diameter target replacing the previous 12.7 mm target. In the second test, the lower heat shield was replaced by a heat shield of 0.025 mm aluminum foil (with a silver plated copper baffle). It was hoped that the first test would indicate the target contribution to the radiative transfer, however, a poor vacuum during this test (about 12×10^{-6} mm Hg) largely obscured the effect being investigated. The measured consumption rate was 67 cc/hour. The second test yielded a rate of 77 cc/hour (with the vacuum back at 10^{-6} mm Hg). A rough analysis of these results, assuming an emissivity of 0.9 for H-film leads to the observations that: radiative transfer to the target is about 20 per cent of the transfer to the reservoir (the ratio of the areas is about 3 per cent); conductive gas transfer increases the consumption rate by about 1.5 cc/hour per 10^{-6} mm Hg pressure; and the inferior heat shield increased the radiative transfer of heat by about 50 per cent. It should be noted that the lower heat shield of Goldstein's cryostat was at least twice the area of the one used here, and an appropriately greater increase in radiation transfer would be expected.

To summarize, it may be concluded that the major contributions to heat transfer in the earlier cryostat were due to the heat shield construction and to the use of centering screws. The extremely low consumption rate of the cryostat constructed for this experiment may be largely attributed to the fact that these features were avoided.

FIGURE 1

EXTERNAL BEAM TRANSPORT SYSTEM

FIGURE 1

This schematic diagram illustrates the main features of the external beam transport system of the McGill Synchrocyclotron, as used in the present experiment.

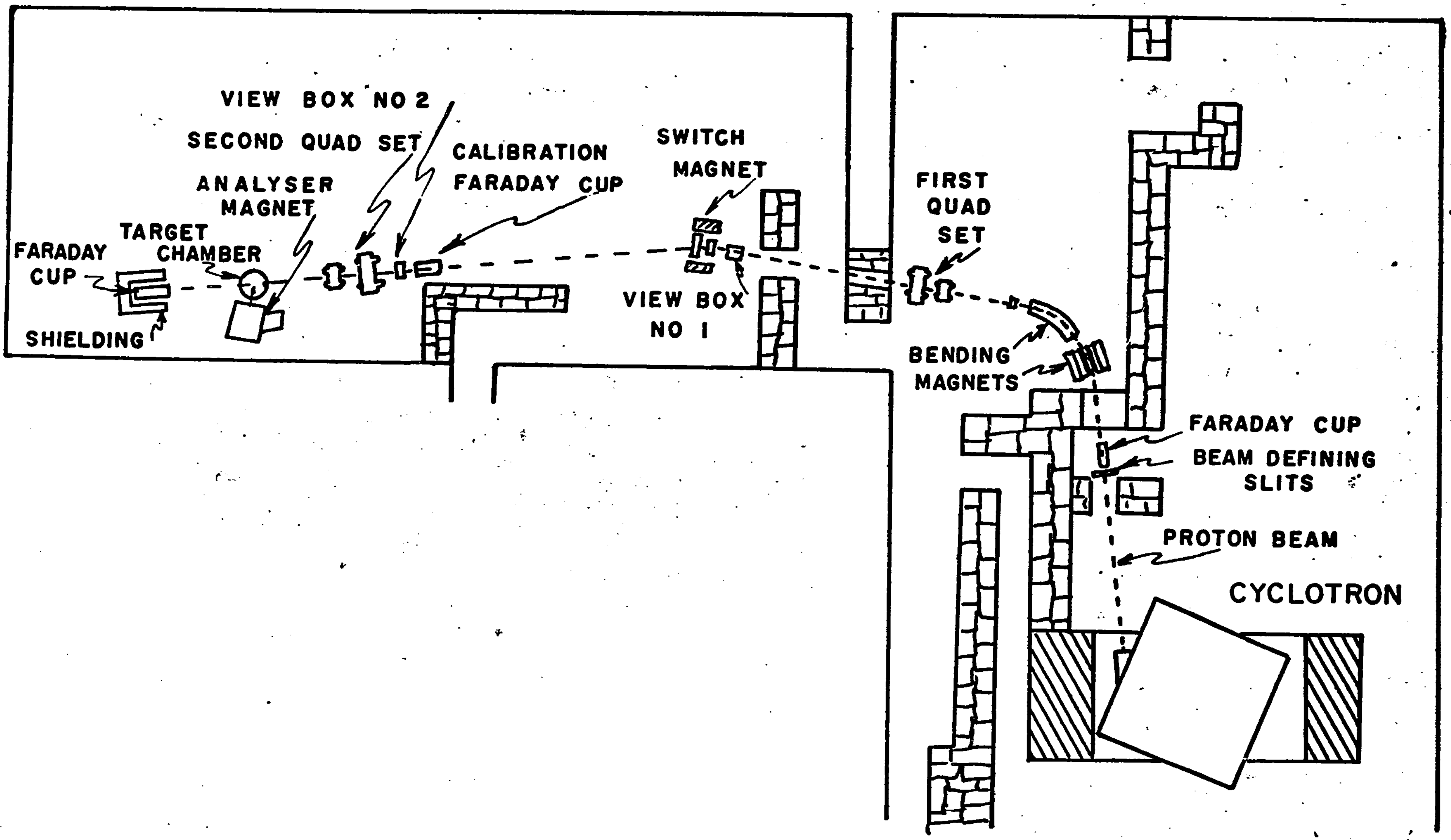
VIEW BOX NO 2
SECOND QUAD SET
CALIBRATION FARADAY CUP
SWITCH MAGNET
FIRST QUAD SET
ANALYSER MAGNET
TARGET CHAMBER
FARADAY CUP
SHIELDING
VIEW BOX NO 1
BENDING MAGNETS
FARADAY CUP
BEAM DEFINING SLITS
PROTON BEAM
CYCLOTRON

FIGURE 2

EXPERIMENTAL LAYOUT

FIGURE 2

This diagram illustrates, schematically, the experimental layout (not to scale). The insert shows the target holder which enabled the interchange of up to four targets without breaking the vacuum. One target position contained a fluorescent screen which was viewed by closed circuit television and facilitated alignment of the beam. The target assembly was directly interchangeable with the liquid helium cryogenic target.

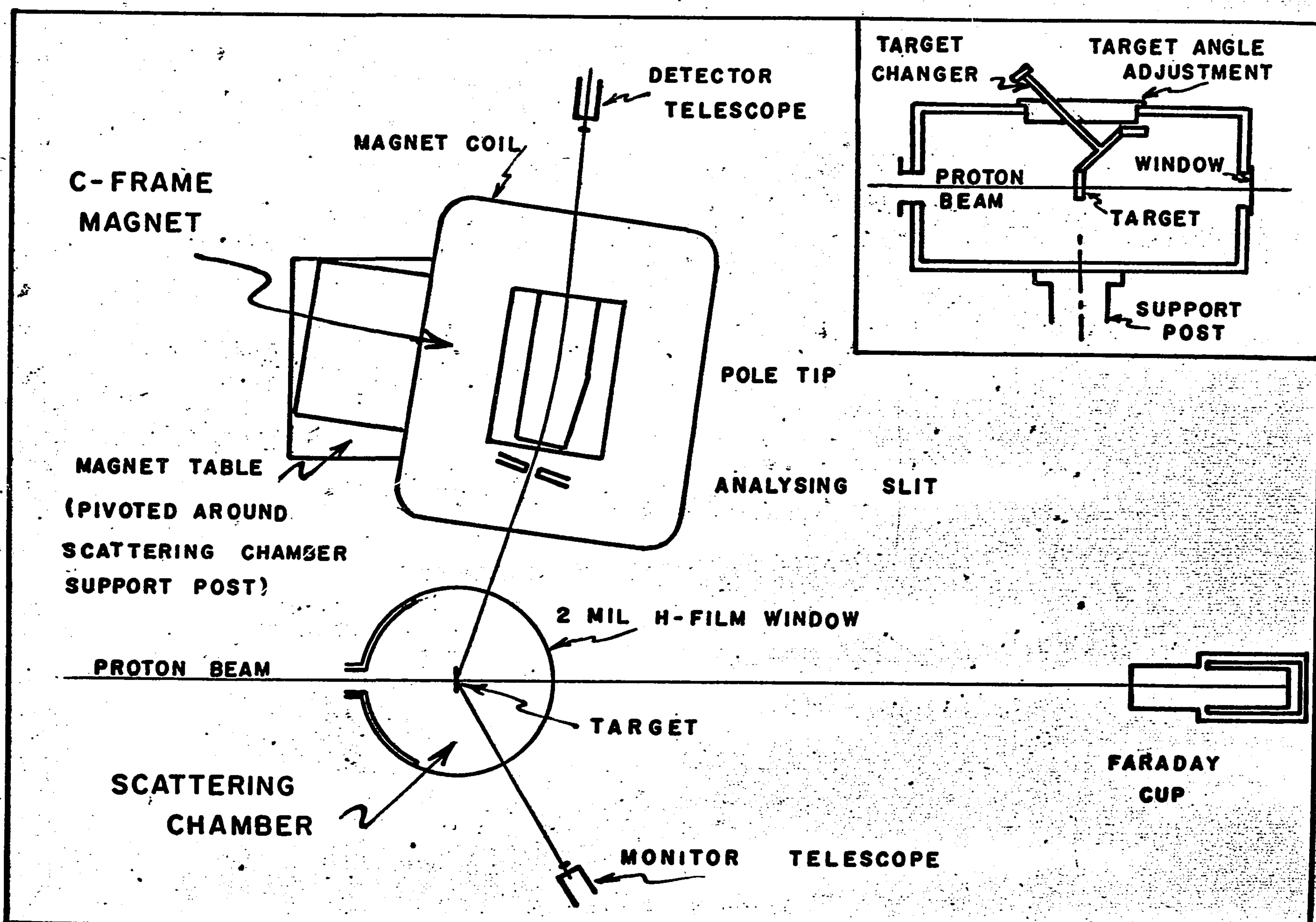
DETECTOR
TELESCOPE
MAGNET COIL
C-FRAME
MAGNET
POLE TIP
MAGNET TABLE
(PIVOTED AROUND
SCATTERING CHAMBER
SUPPORT POST)
ANALYSING SLIT
2 MIL H-FILM WINDOW
PROTON BEAM
TARGET
SCATTERING
CHAMBER
MONITOR TELESCOPE
FARADAY
CUP
TARGET
CHANGER
TARGET ANGLE
ADJUSTMENT
WINDOW
PROTON
BEAM
TARGET
SUPPORT
POST

FIGURE 3

EXPERIMENTAL SYSTEM

FIGURE 3

This photograph shows all the main features of the experimental set-up. The scattering chamber with its H-film window and the C-frame Analyser Magnet are seen in the centre, with the monitor telescope pivoted about the chamber support post on the left and the main counter telescope behind the magnet on the right. The Faraday Cup, surrounded by lead shielding blocks is evident in the foreground. Some of the lead shielding has been removed from the magnet and the Faraday Cup to show these features more clearly. The vacuum chamber in the magnet pole gap, the pole tips, and the analysing slits are just visible.

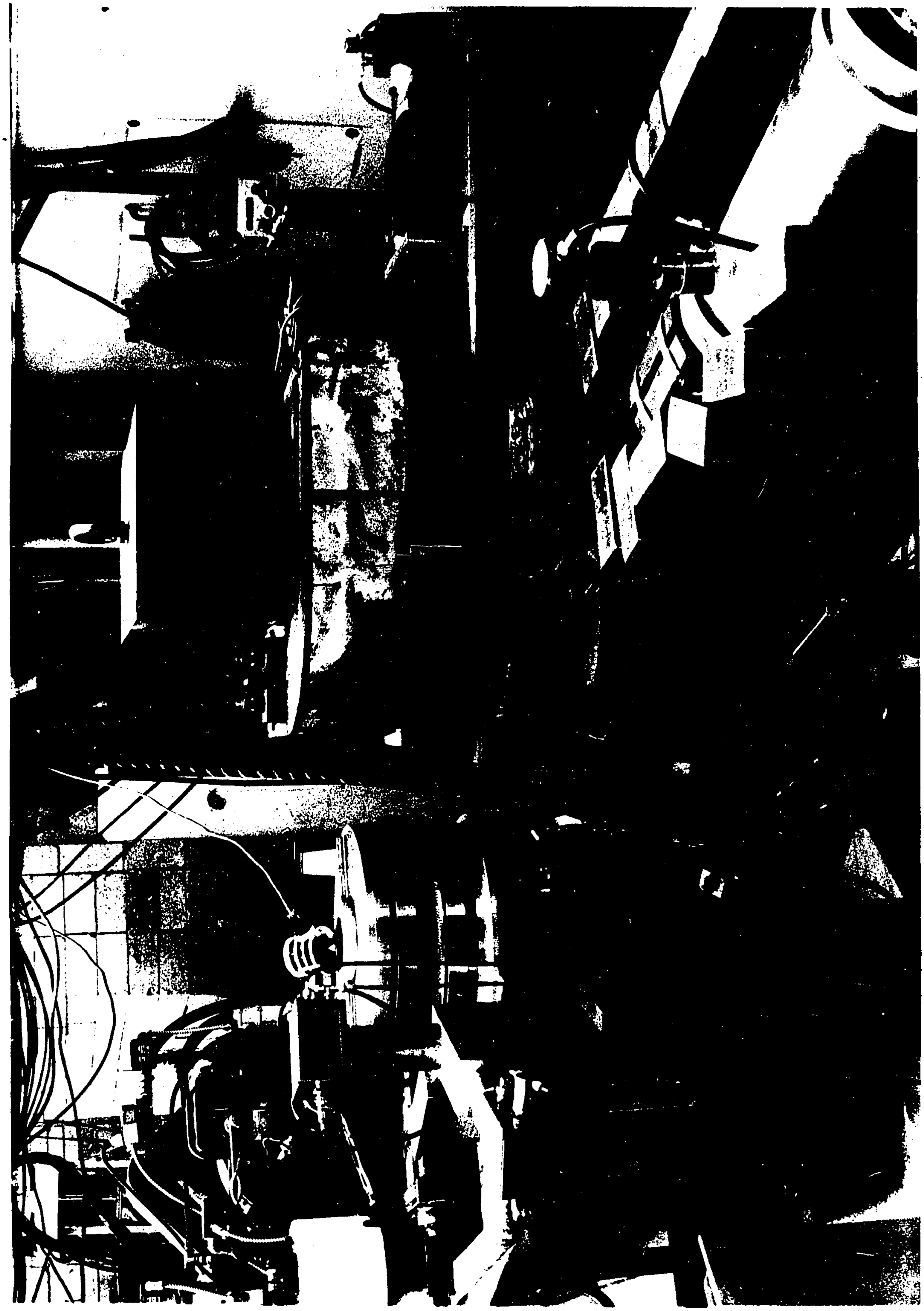

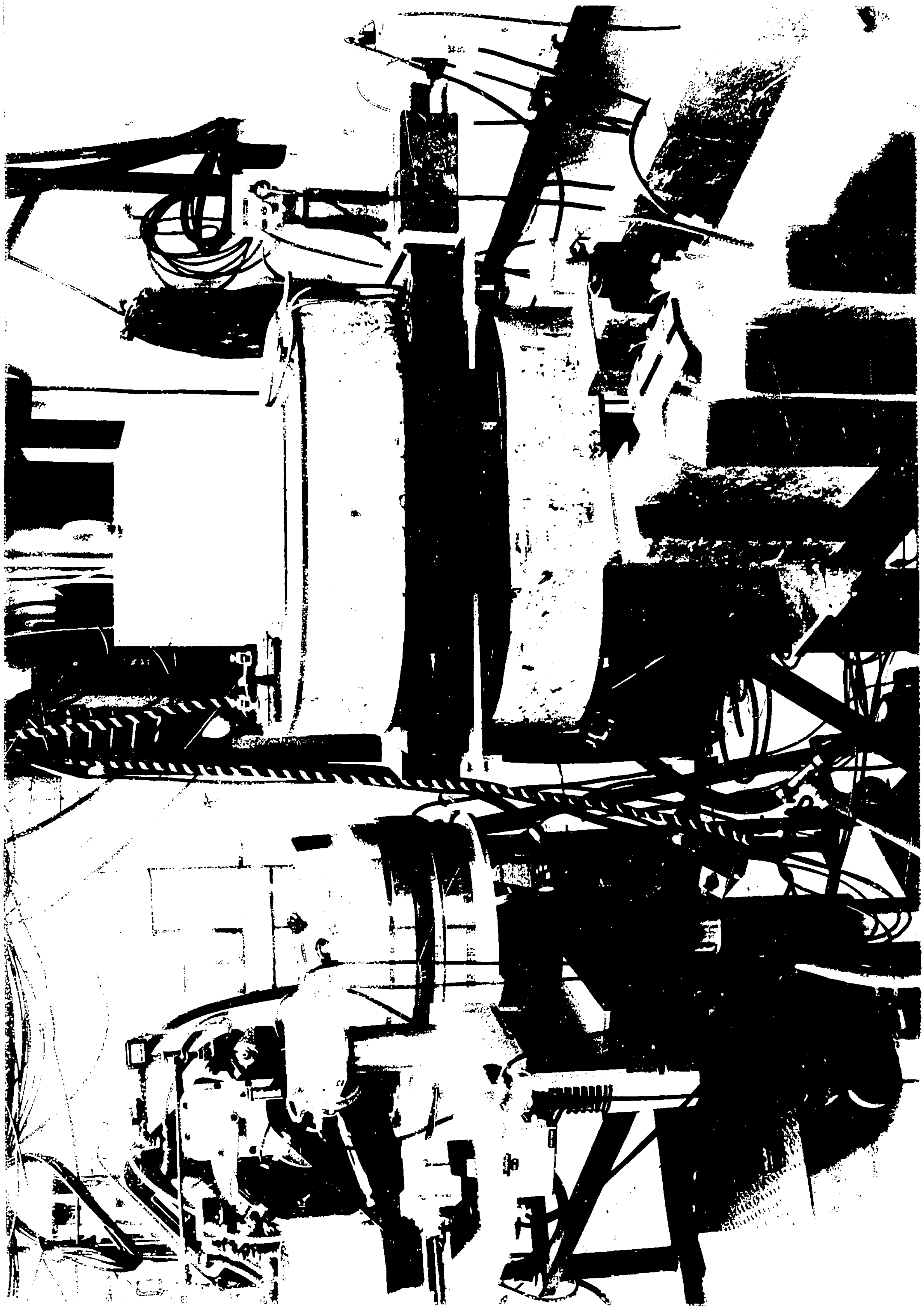

FIGURE 4

ANALYSER MAGNET FIELD MAP FOR CENTRAL PATH

FIGURE 4

This figure shows graphically the field map of the analyser magnet from the target position to the detector along the central path. It is arbitrarily normalized to unity, and the shape remains unchanged over the range of magnetic excitation used. The fringing field is quite evident. The division of the path into sectors for analysis of the magnet (described in the text) is shown, the sectors being labeled M_1, M_2.. etc.

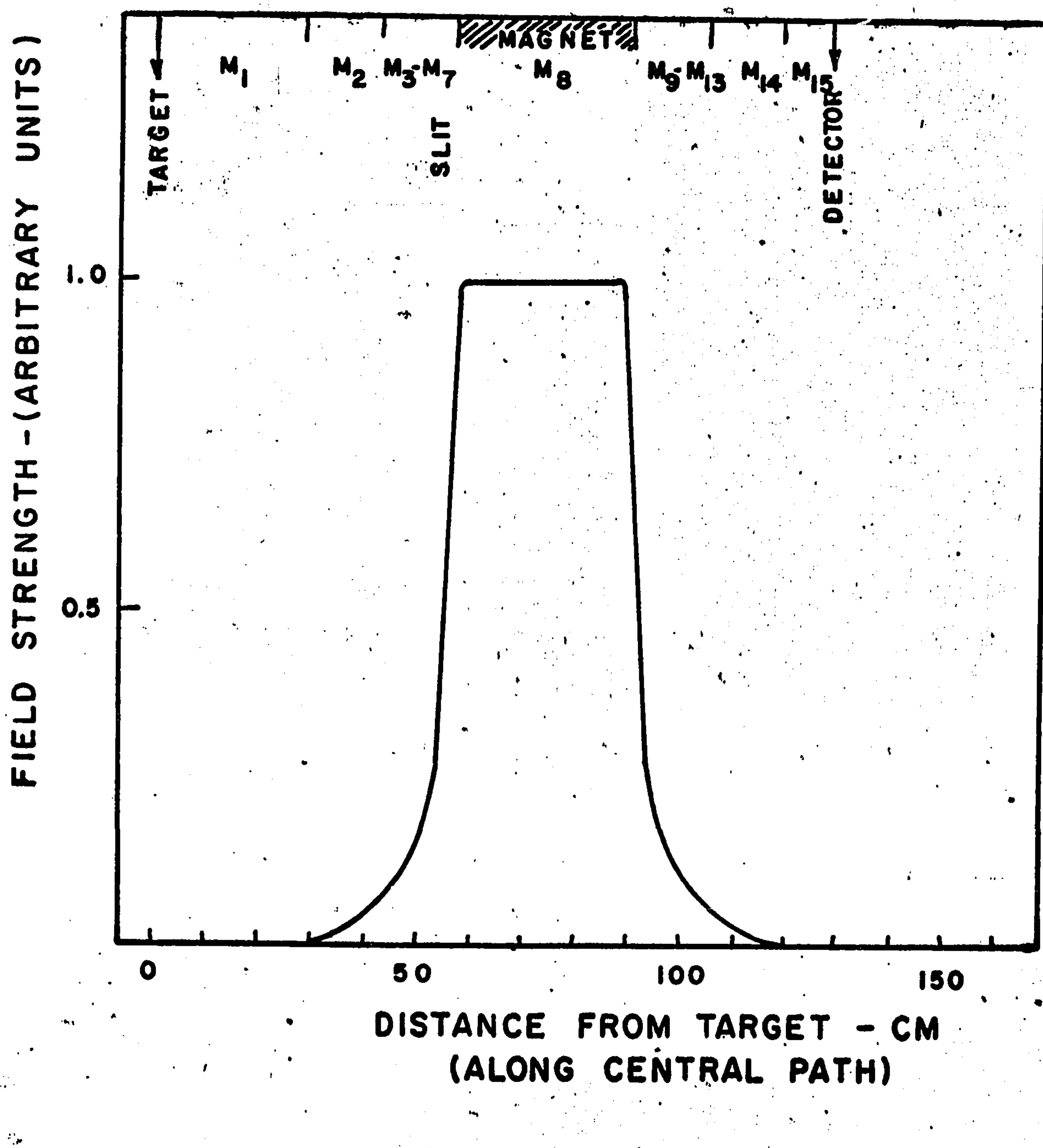
MAGNET
TARGET
M_1
M_2
M_3-M_7
SLIT
M_8
M_9-M_{13}
M_{14}
M_{15}
DETECTOR
FIELD STRENGTH - (ARBITRARY UNITS)
1.0
0.5
0
50
100
150
DISTANCE FROM TARGET - CM
(ALONG CENTRAL PATH)

FIGURE 5

MAGNET MOMENTUM SELECTION CHARACTERISTICS

FIGURE 5

The momentum selection characteristics of the analyser magnet showing regions of total and partial transmission for a 1 mm (and 4 mm) beam spot and slit settings of $\pm$ 7.5 mm. Details are discussed in the text.

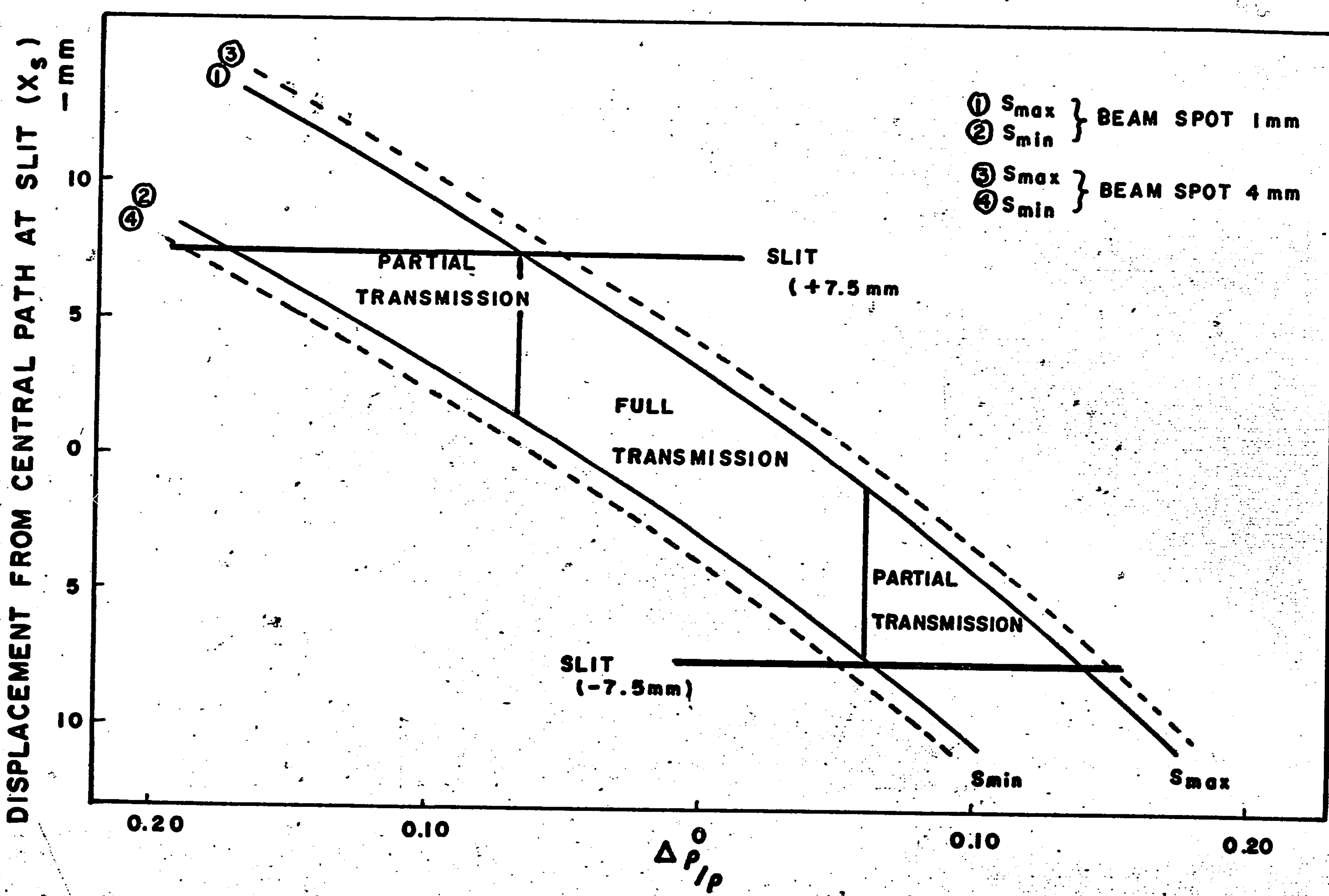

DISPLACEMENT FROM CENTRAL PATH AT SLIT (X_s) — mm
10
5
0
5
10
0.20
0.10
0
0.10
0.20
$\Delta \rho / \rho$
1 S_{max}
2 S_{min}
BEAM SPOT 1 mm
3 S_{max}
4 S_{min}
BEAM SPOT 4 mm
1
3
2
4
SLIT
(+7.5 mm
PARTIAL
TRANSMISSION
FULL
TRANSMISSION
PARTIAL
TRANSMISSION
SLIT
(-7.5mm)
S_{min}
S_{max}

FIGURE 6

ANALYSER MAGNET TRANSMISSION FOR PROTONS, DEUTERONS AND TRITONS

FIGURE 6

The transmission of selected momentum "bites" by the analyser magnet, is shown, where the central ray has the magnetic rigidity appropriate to a) 90 MeV protons, b) 80 MeV deuterons and c) 70 MeV tritons. These are representative of the requirements of the present experiment and have been calculated for a 1 mm beam spot. Alpha and ^{3}He transmission are not shown.

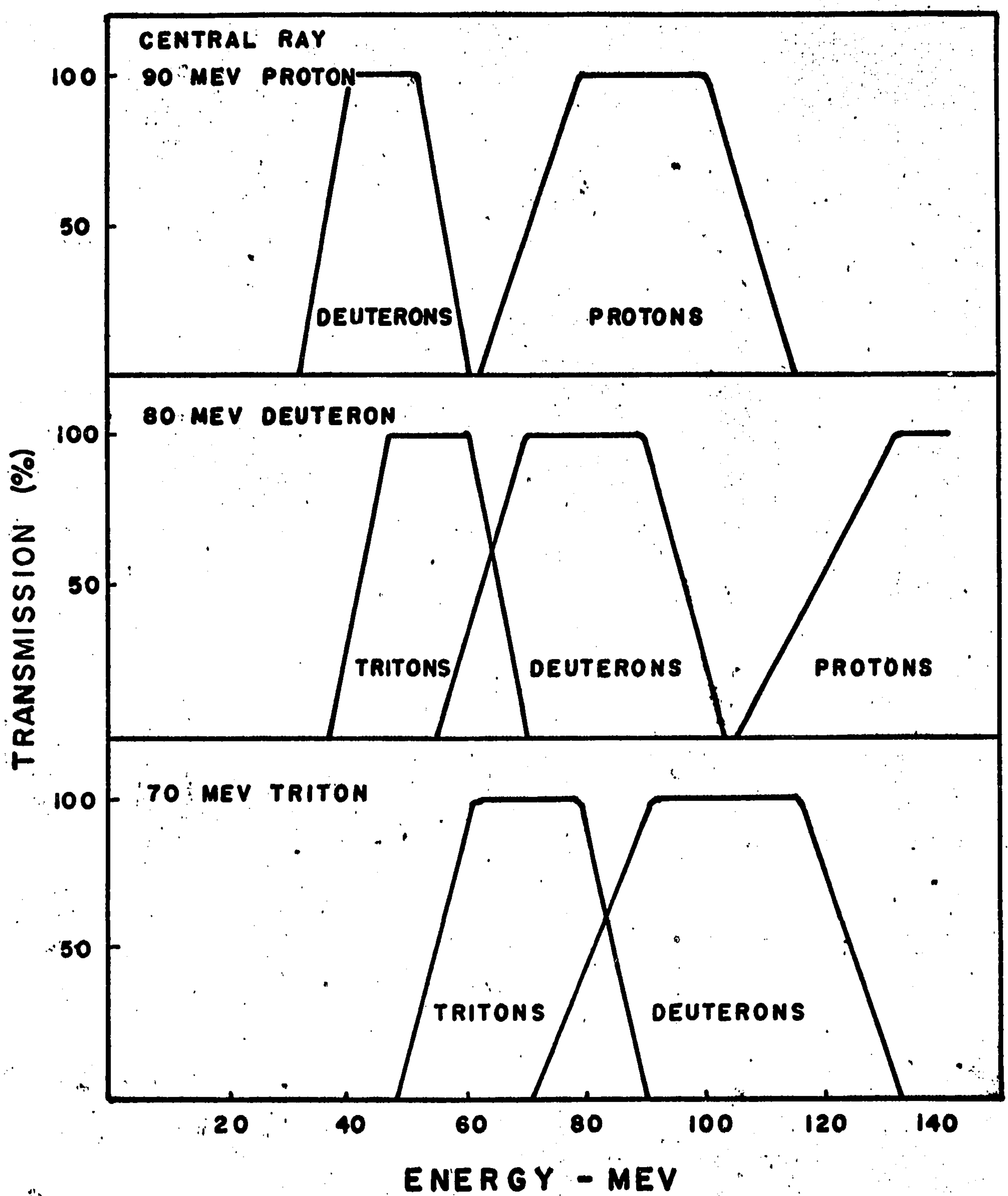
CENTRAL RAY
90 MEV PROTON
DEUTERONS
PROTONS
80 MEV DEUTERON
TRITONS
DEUTERONS
PROTONS
70 MEV TRITON
TRITONS
DEUTERONS
100
50
100
50
100
50
TRANSMISSION (%)
20
40
60
80
100
120
140
ENERGY - MEV

FIGURE 7

DEPENDENCE OF ENERGY "BITE" ON PARTICLE ENERGY AND BEAM SPOT SIZE

FIGURE 7

This figure shows graphically the size of the energy "bite" (i.e. region of 100% transmission) as a function of particle energy, for several beam spot sizes. The finite thickness of the curves reflects the slight difference between the various particle species. (Tritons have slightly larger energy "bites" than protons).

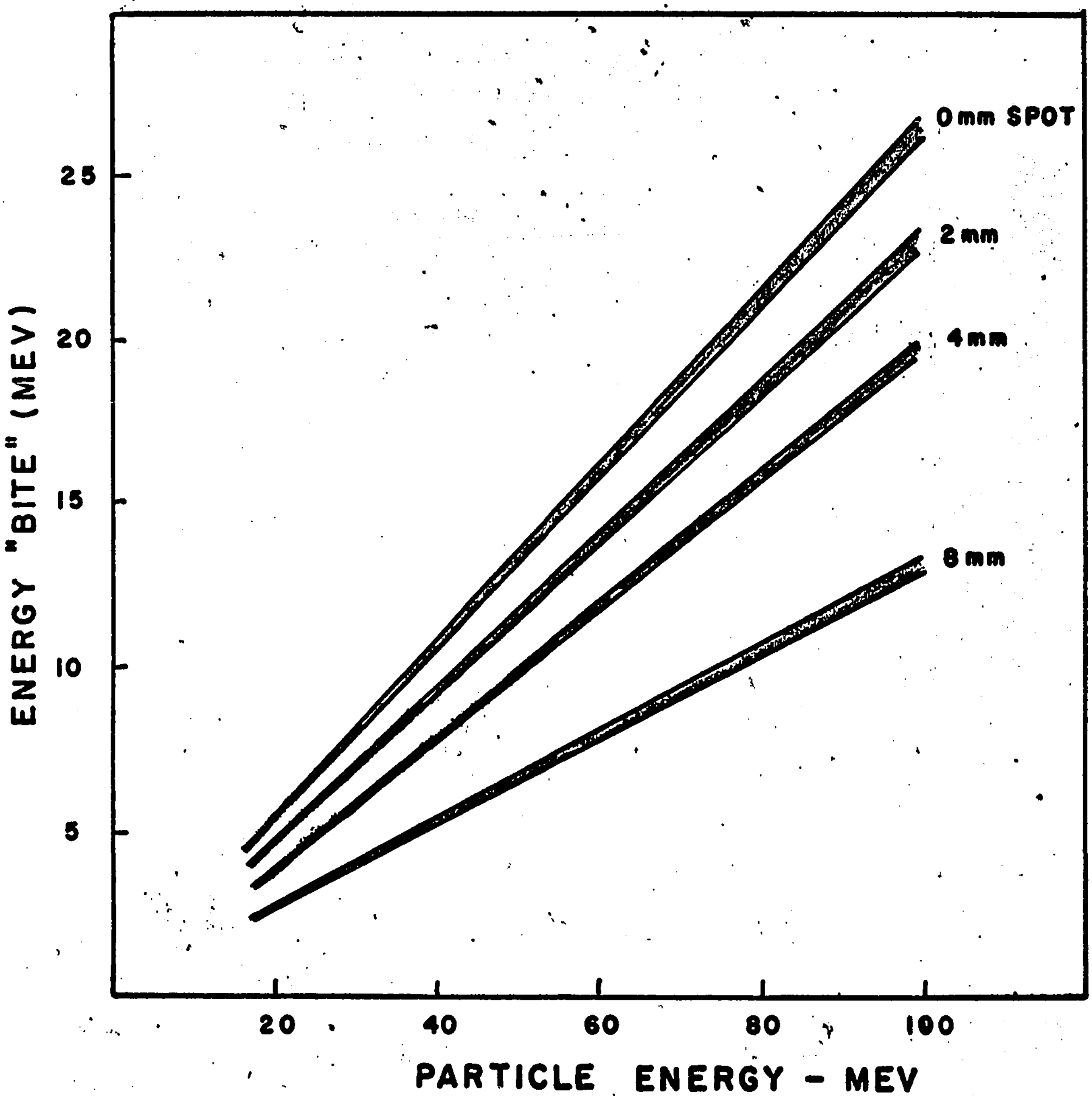

0 mm SPOT
2 mm
4 mm
8 mm
25
20
15
10
5
20
40
60
80
100
ENERGY "BITE" (MEV)
PARTICLE ENERGY - MEV

FIGURE 8

ANALYSER MAGNET ENERGY CALIBRATION

FIGURE 8

The magnet excitation current settings are plotted as a function of the central path particle energy for protons, deuterons, tritons, ^{3}He's and alphas. The proton calibration was obtained empirically as described in the text, the others being derived by calculation. The experimental points for the protons and one point to check the deuterons are also shown.

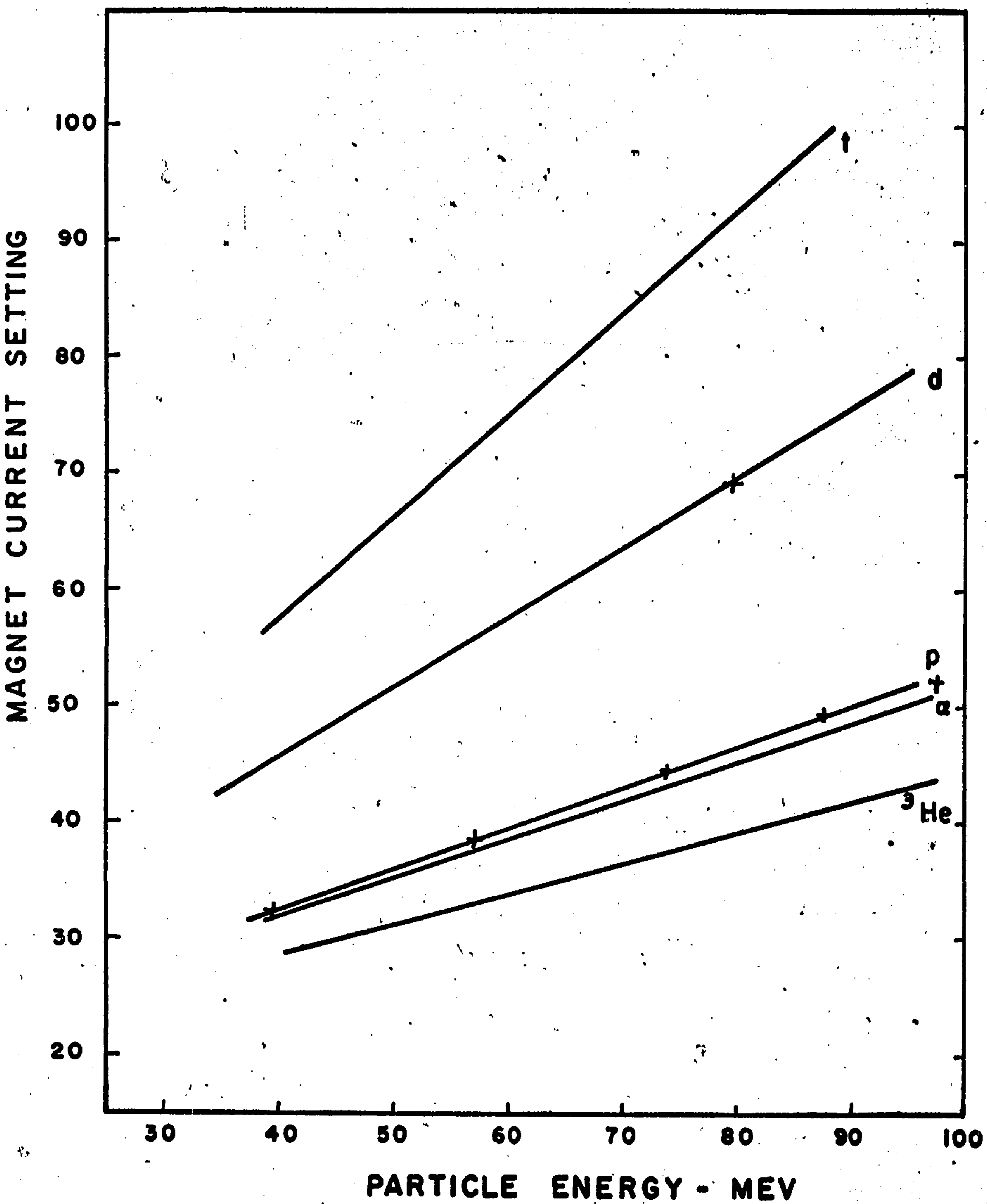
MAGNET CURRENT SETTING
100
90
80
70
60
50
40
30
20
t
d
p
α
^{3}He
30
40
50
60
70
80
90
100
PARTICLE ENERGY - MEV

FIGURE 9

COUNTER TELESCOPE GEOMETRY

FIGURE 9

The geometry of the counter telescope is shown schematically, illustrating in particular the reflector for the ΔE scintillator. (The geometry for the monitor counter telescope was essentially the same).

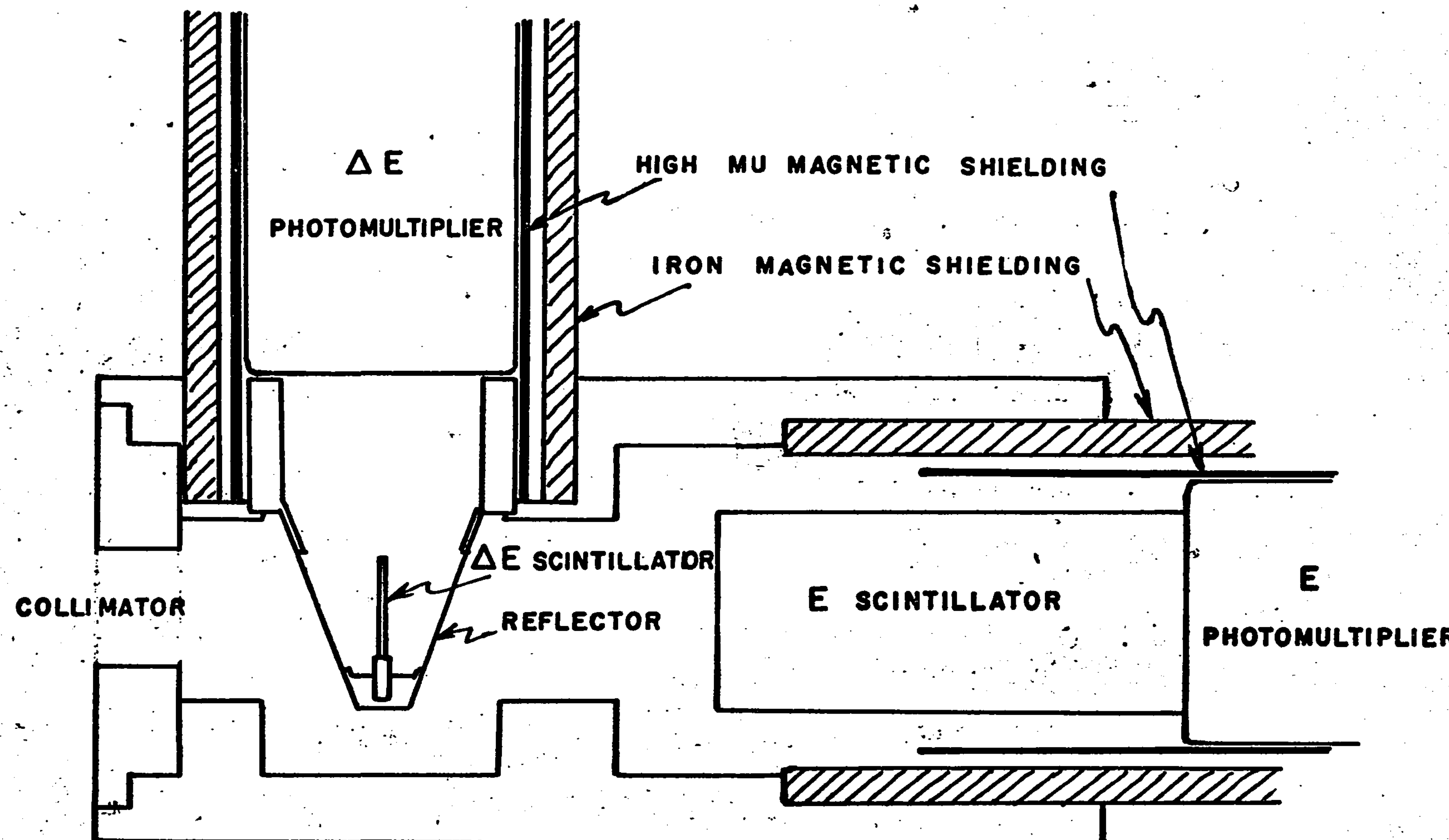
ΔE
PHOTOMULTIPLIER
HIGH MU MAGNETIC SHIELDING
IRON MAGNETIC SHIELDING
ΔE SCINTILLATOR
COLLIMATOR
REFLECTOR
E SCINTILLATOR
E
PHOTOMULTIPLIER

FIGURE 10

ELECTRONICS

FIGURE 10

This figure shows a block diagram of the electronics associated with both the main detector telescope and the monitor counter telescope.

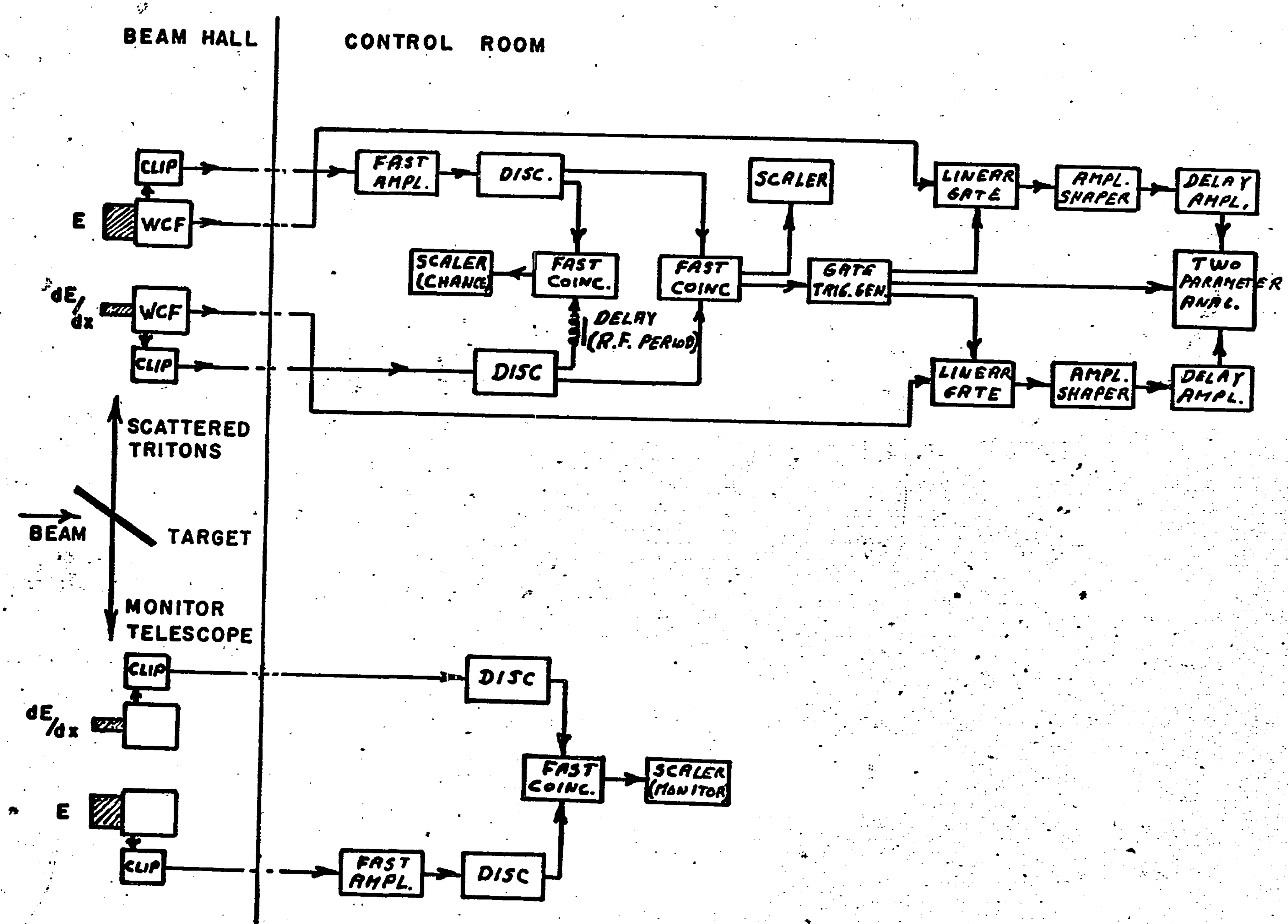

BEAM HALL
CONTROL ROOM
CLIP
E
WCF
dE/dx
WCF
CLIP
FAST AMPL.
DISC.
SCALER
LINEAR GATE
AMPL. SHAPER
DELAY AMPL.
SCALER (CHANCE)
FAST COINC.
FAST COINC
GATE TRIG. GEN
TWO PARAMETER ANAL.
DELAY (R.F. PERIOD)
DISC
LINEAR GATE
AMPL. SHAPER
DELAY AMPL.
SCATTERED TRITONS
BEAM
TARGET
MONITOR TELESCOPE
CLIP
DISC
dE/dx
FAST COINC.
SCALER (MONITOR)
E
CLIP
FAST AMPL.
DISC

FIGURE 11

LIQUID HELIUM CRYOGENIC TARGET

FIGURE 11

This diagram shows the main details of the liquid helium target and its placement in the scattering chamber. The diagram is approximately to scale.

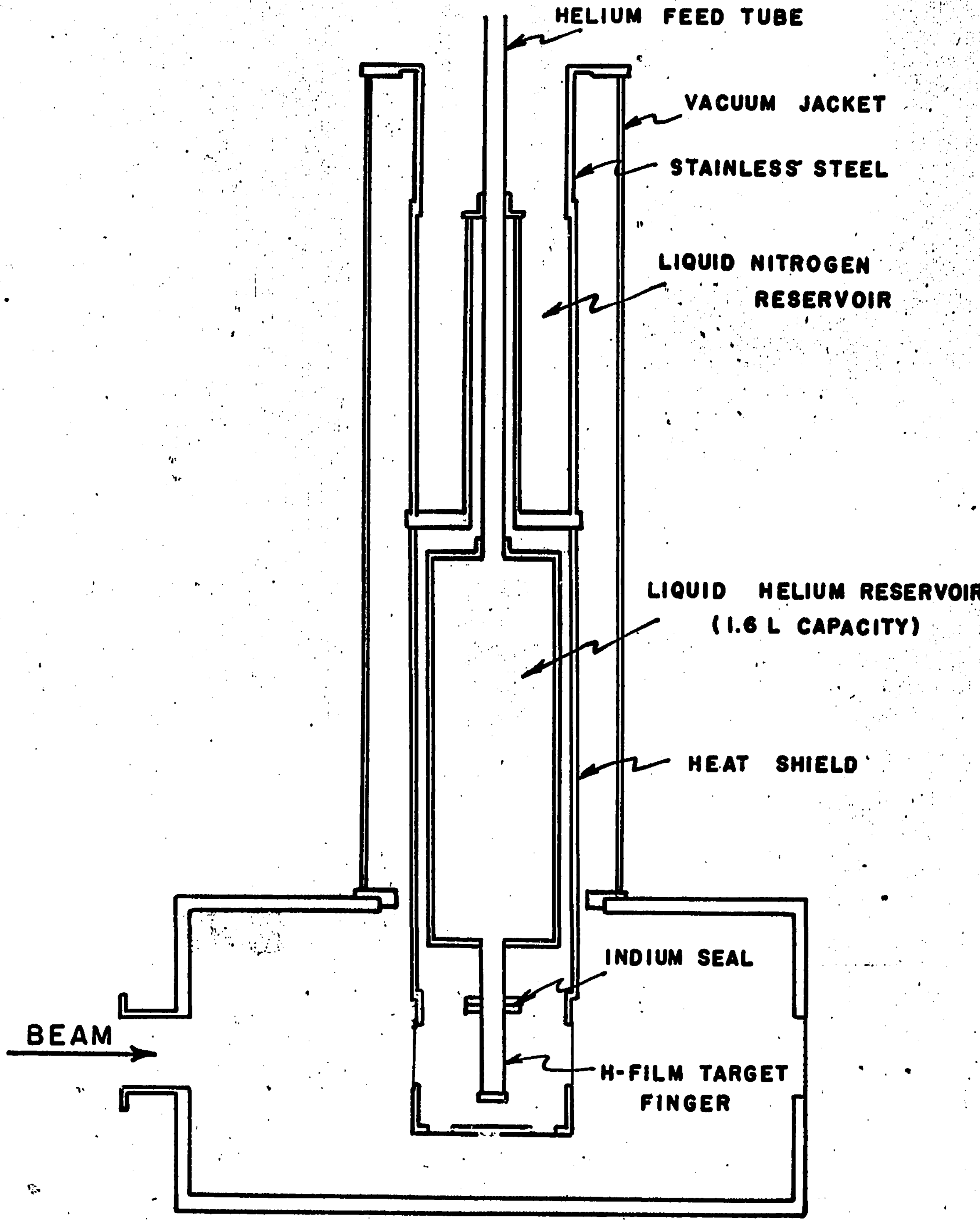

SCATTERING CHAMBER

CHAPTER 3. EXPERIMENTAL PROCEDURE

3.1 Proton Beam Alignment:

At the start of each run the proton beam was aligned on the target centre with the aid of the two viewing boxes in the beam transport system and the fluorescent screen in the target position. The position and direction of the beam at the target were easily reproducible by ensuring that the beam spot was centered at both viewing boxes as well as at the target. The beam spot size was typically 1 mm to 2 mm in diameter and centered on the target to better than 0.5 mm. The divergence of the beam varied with beam intensity, since the intensity was itself determined by the horizontal size of the beam defining slits. The maximum total divergence was about 1° and more usually about 0.5°. The beam position was checked at both viewing boxes several times during a run for possible changes due to magnet power supply drifts.

In the experiments with the liquid helium target a different procedure for alignment was used, due to the absence of a fluorescent screen at the target position. The monitor counter telescope was set at a scattering angle of about 60° and the incident beam was swept across the helium target finger in small steps by varying the switching magnet field. For each step the counting rate from the monitor telescope was scaled for a unit of incident beam collected by the Faraday cup. To first order, the counting rate is proportional to the thickness of helium traversed by the beam, the maximum counting rate occurring for a beam centered on the target. In practice the only difficulty associated with this method was the problem of reproducing magnet settings due to hysteresis. This was solved by cycling the magnet. An example of the target profile obtained by this method is shown in fig. 12a. The solid curve represents the variation of the counting rate expected for the 12.7 mm diameter target, calculated on the basis of the known spot size and target thickness, and arbitrarily normalized to 1 at the maximum. The experimental points, similarly normalized, can be seen to be in excellent agreement with the expected profile. The spatial position of the beam corresponding to the various magnet settings was obtained with the target screen in place of the helium target.

3.2 Zero Angle Calibration:

An absolute calibration of the zero angle, or incident beam direction was made for each run prior to data accumulation. The method was essentially to compare the cross-section for scattering on either side of the incident beam, finding left and right scattering angles at which the cross-sections were equal, the bisector of these angles then defining the zero angle. This calibration was made using a carbon target as a standard, except in the case of the runs with the helium target when the helium target itself was used. An angle at which the cross-section varies rapidly was chosen; 20^{o} for Carbon (Ma66) and 25^{o} for Helium (Go67). Initially the zero angle determination was made for both the main detector telescope and the monitor counter telescope, and this provided an absolute calibration of their relative zero angles. In subsequent runs it was found to be more convenient to measure monitor telescope zero angle and infer the zero angle correction for the main detector telescope from the earlier calibrations. Experimentally, the monitor counter was set at the appropriate angle on one side of the incident beam direction and the number of counts for a unit of beam recorded. This was then repeated on the opposite side at the same angle, and at angles smaller and larger by one degree. The zero angle was then determined graphically by plotting the counting rate differences against angle, as shown in fig. 12b for a helium run.

3.3 Beam Monitor Calibrations:

a) Faraday Cup:

The Faraday Cup was used as the beam monitor in the angular region from 30° to the backward angles. A calibration of the cup was made at each angle following data collection. This was necessary since different fringing field conditions caused small shifts in the unscattered beam position at the cup entrance and subsequent changes in the cup collection efficiency. In addition, changes in beam intensity involved changes in the divergence of the beam at the target which also gave rise to differences in the cup efficiency. The calibration was accomplished by comparing the main cup with the calibration cup in the external beam system (described in a previous section). Normalization of the two cups was achieved by collecting the charge with the same integrator and using, as an intermediate monitor, the beam current intercepted by the horizontal defining slits of the beam transport system. The slit current was integrated with a Keithley micromicro ammeter modified to measure charge. To first order, at least over short time intervals, the intercepted beam should provide a fairly reliable intermediate monitor and this in fact was found to be the case from the consistency of a number of consecutive readings. Several measurements were made each time to minimize the effects of small variations. (The advantages of a direct transmission secondary monitor such as an ionization chamber are obvious). Calibration of the Faraday cup in this way gave corrections no larger than 3% and more typically of the order of 1%.

b) Monitor Telescope:

The monitor counter served as the sole beam monitor at scattering angles smaller than 30^o, and was used in conjunction with the Faraday cup at larger angles. Calibration of the monitor counter was accomplished simply by ensuring that during the course of each run, some data be accumulated at an angle greater than 30^o, permitting simultaneous monitoring of the beam with the Faraday cup. At small angles the monitor telescope was well shielded from the plexiglas beam stopper with lead blocks. To check for possible counting rate effects due to background (largely gamma ray) from the beam stopper, the monitor rates with the plexiglas stopper in and out were compared (with the magnet at an angle larger than 30^o). No noticeable effect was observed. The monitor counter was also checked by comparison with the Faraday cup, for counting rate dependence of the counting efficiency, no systematic effects being observed for counting rates up to $10^4 sec^{-1}$. In the early stages of the experiment checks were made for possible effects on the counting rate due to gain shifts in the photomultipliers (or small angle shifts) caused by the magnet's fringing field. No systematic differences in counting rate were observed with the magnet on or off, again using the beam slits as an intermediate monitor.

c) Current Integrator:

At the start of each run and usually once or twice during the course of a run, the current integrator was calibrated. This was done using a Keithley picoampere source (model 261) on each integrator scale used. Absolute calibration has been described in section 2.5 (c).

3.4 Magnet Settings:

The magnet setting was determined for each reaction and at each angle on the basis of the energy calibration described in section 2.3 and plotted in fig. 8. The central path energy was obtained from the reaction kinematics and the required range of excitation, allowance being made for particle energy losses in the target and windows. The settings were always chosen conservatively to allow a wide margin for possible variations, especially those due to hysteresis effects in the magnet. Only the central 80 per cent of the full transmission region was used, and the magnet was cycled before changing a setting. In some cases it was necessary to accumulate overlapping spectra at two magnet settings in order to study a range of excitation which was larger than the full transmission energy "bite".

3.5 ΔE Discriminator Setting:

Where necessary, the ΔE discriminator was used in conjunction with the magnet to improve particle separation. ΔE discrimination was accomplished with the fast discriminator in the ΔE side of the fast coincidence circuit. Ideally it would be desirable to use a single channel analyser for this purpose, setting a window on the ΔE spectrum and gating the E spectrum accordingly. It was found, however, that the use of a lower level discriminator alone (which was already an integral part of the electronics) did not limit the flexibility of the system. Particle species with higher specific ionization (i.e. larger ΔE pulses viz. deuterons or tritons) were usually well separated in energy from the particle species being studied. This was due both to the magnet properties and to the lower (intrinsic) output of the plastic E counter for the more highly ionizing particles.

Figures 13a, b, and c, show typical spectra from the ΔE counter of protons, deutrons, and tritons, from a carbon target at a scattering angle of 30°. These were accumulated with magnet settings corresponding to central path rigidities of 90 MeV protons, 75 MeV deuterons and 70 MeV tritons respectively. In each case the ΔE scintillator was 2mm thick and the lowest ΔE discriminator level was used. These spectra illustrate to some extent the effect of magnetic separation alone. The study of protons did not require ΔE discrimination. In the case of deuterons or tritons, the ΔE discriminator was set to cut the ΔE spectrum off below the minimum E pulse height for the appropriate particle group.

The cut off level was chosen conservatively to ensure no loss of the particle species being investigated. This meant that there was always some feedthrough of the heavier particles, which in fact was enhanced by the effect of the Landau tail. In all cases particle species with higher ionizing rates (higher ΔE pulse height) appeared in a part of the energy (E) spectrum outside the region of interest.

In cases where it was difficult to decide on the discriminator setting, it was found useful to determine the best setting while accumulating data in the two dimensional, ΔE vs E mode of the two parameter analyser. In this mode particles of different species appear as ridges in the display, following a locus determined by the relationship between dE/dx and E (i.e. essentially hyperbolae). The width of these ridges (or conversely, the separation between the ridges) is dependent on the ΔE resolution. The limiting factor in the choice of ΔE resolution was the energy loss suffered by the particles in passing through the ΔE counter and consequent deterioration in the E counter resolution. This technique also provided a very useful indication of the extent to which feedthrough was present in the region of interest in a particular spectrum. These points are illustrated by the two parameter spectra of fig. 14, which also show several interesting features of the particle separation.

The target used was ^{6}Li and the scattering angle 15^o. Fig 14a shows a spectrum obtained with the magnet and ΔE discriminator set for deuterons from the ^{6}Li (p,d)^{5}Li reaction. The two prominent deuteron peaks correspond to excitation of the ^{5}Li ground state and a level at

16.65 MeV. The deuteron cutoff due to the magnet characteristics is quite evident as is the lack of protons after ΔE discrimination. Tritons accepted by the magnetic selection appear as a ridge behind the deuterons (at a higher ΔE) and in a lower energy region. In fig. 14b the display of fig. 14a has been rotated by 180^{o} in the kicksorter memory to show the tritons more clearly. Fig. 14c shows a spectrum obtained with the magnet and ΔE discriminator now set for tritons from the ^{6}Li (p,t)^{4}Li reaction. The gain settings were the same as in figs. 14a and b. In this display the integrated energy (E) spectrum is also shown in the first row of channels. Figs. 15a and b illustrate two additional examples of the particle separation. Fig. 15a shows a spectrum of tritons at 5^{o}Lab from the reaction ^{7}Li (p,t)^{5}Li, the high energy triton peak corresponding to the ground state of ^{5}Li. Fig. 15b is representative of the separation possible with protons, and shows a spectrum of protons at 30^{o}Lab. from a CH target. The three main peaks correspond to protons scattered from the ground state and from the 4.43 and 9.65 MeV excited states of ^{12}C. The lowest energy proton peak is due to elastic proton proton scattering from the hydrogen content of the target and is only partially transmitted by the magnet, illustrating an energy "bite" of somewhat less than 23 MeV.

Feedthrough of protons in the deuteron spectra was not a serious problem, as can be seen in figs. 14a and b, and in fact was negligible at the high energy end of the spectrum. Feedthrough of deuterons in the triton spectra (Figs. 14c and 15a) was more difficult to avoid and a correction had to be estimated in most cases.

3.6 Background Measurements:

The background contribution was checked at each angle by comparing target in-target out counting rates. At angles larger than 30° the background counting rate (coincidence rate) was essentially zero. In the small angle region, the large flux of gammas and neutrons produced by the beam stopper contributed in some cases to an appreciable background counting rate in the detector, in spite of all efforts at shielding. However, the background appeared only at the low energy end of the spectrum, well out of the region of interest, and its most serious effect was that of increasing the singles counting rate in the E counter, enhancing chance coincidences and pile-up.

3.7 Chance Coincidence Measurements:

The chance coincidence rate was continuously monitored as described in a previous section. In some cases a chance spectrum was also obtained by insertion of an R.F. delay into one side of the true coincidence circuit. The chance rate was generally negligible at angles larger than 30° and at smaller angles, the detector counting rate was limited to keep the chance rate below about 2 per cent.

3.8 Liquid Helium Target:

The helium target was installed in the scattering chamber and remained in the chamber, under vacuum for the duration of this part of the experiment. Preparatory to each run, the liquid nitrogen reservoir was loaded two hours before filling the target with helium, to allow the inner target assembly to cool down. The scattering chamber vacuum system was isolated from the main external beam transport system and pressures of 10^{-6} mm Hg were typical with the help of the cryopumping. The liquid helium transfer was accomplished using standard techniques with a helium transfer tube. A good transfer took about twenty minutes and used 7 to 8 litres to fill the 1.6 litre reservoir. After all the data had been accumulated with the helium target, background runs with an empty target (maintaining the beam alignment) were made at each angle to allow correction for reactions in the target cylinder and heat shield windows. One transfer of helium was more than sufficient for a typical 20 hour run, but the liquid nitrogen reservoir was replenished every four to five hours.

FIGURE 12

a) BEAM ALIGNMENT ON HELIUM TARGET

AND

b) ZERO ANGLE CALIBRATION

FIGURE 12 a

This diagram shows the profile of the liquid helium target. The solid curve represents the variation in monitor counting rate for the 12.7 mm diameter target, calculated on the basis of the known beam spot size and target thickness. The curve and experimental points (obtained by sweeping the proton beam across the target) have both been arbitrarily normalized to 1 at the maximum.

FIGURE 12 b

This figure illustrates a typical zero angle calibration for a helium run. Monitor counter angles used were 25° left, and 24°, 25°, 26° right. The error bars reflect the maximum uncertainties due to statistical errors. The zero angle corresponds to the intersection of the curve with the line

$$(N_{left} - N_{right}) = 0$$

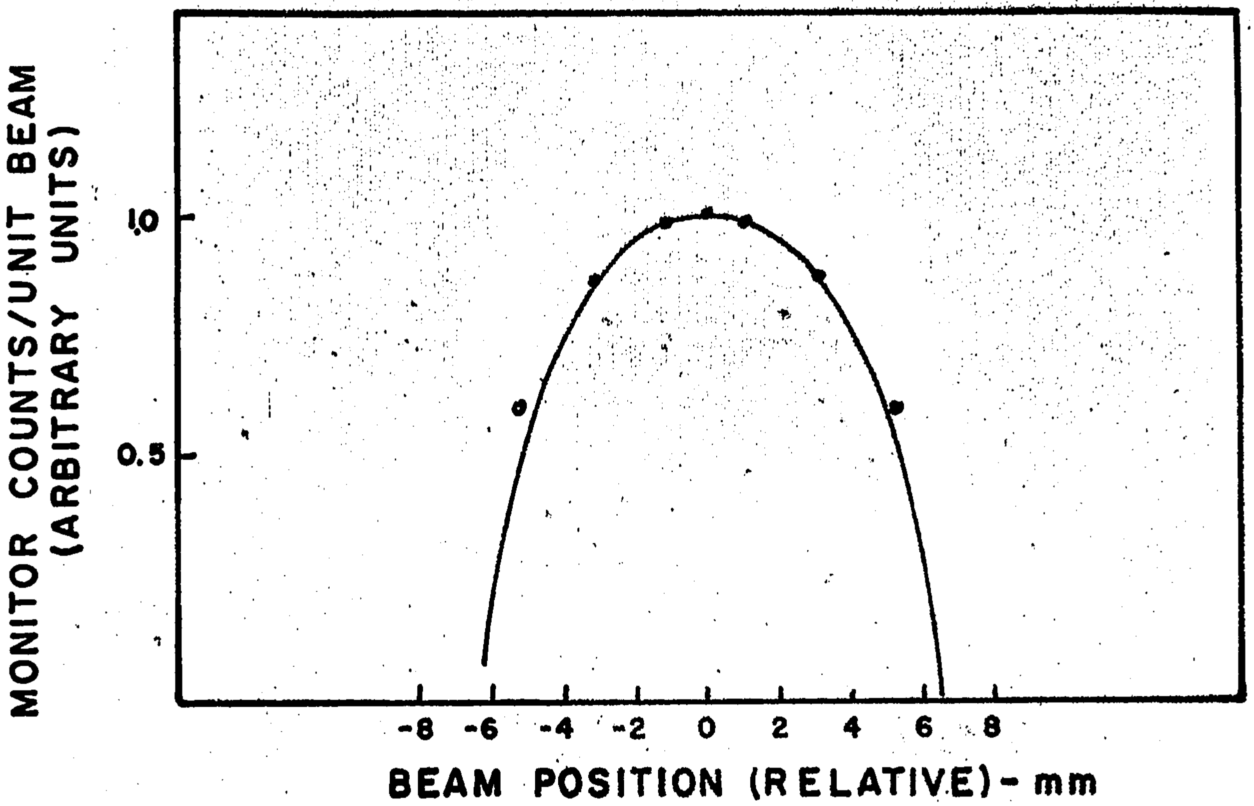
MONITOR COUNTS/UNIT BEAM (ARBITRARY UNITS)
1.0
0.5
-8
-6
-4
-2
0
2
4
6
8
BEAM POSITION (RELATIVE) - mm

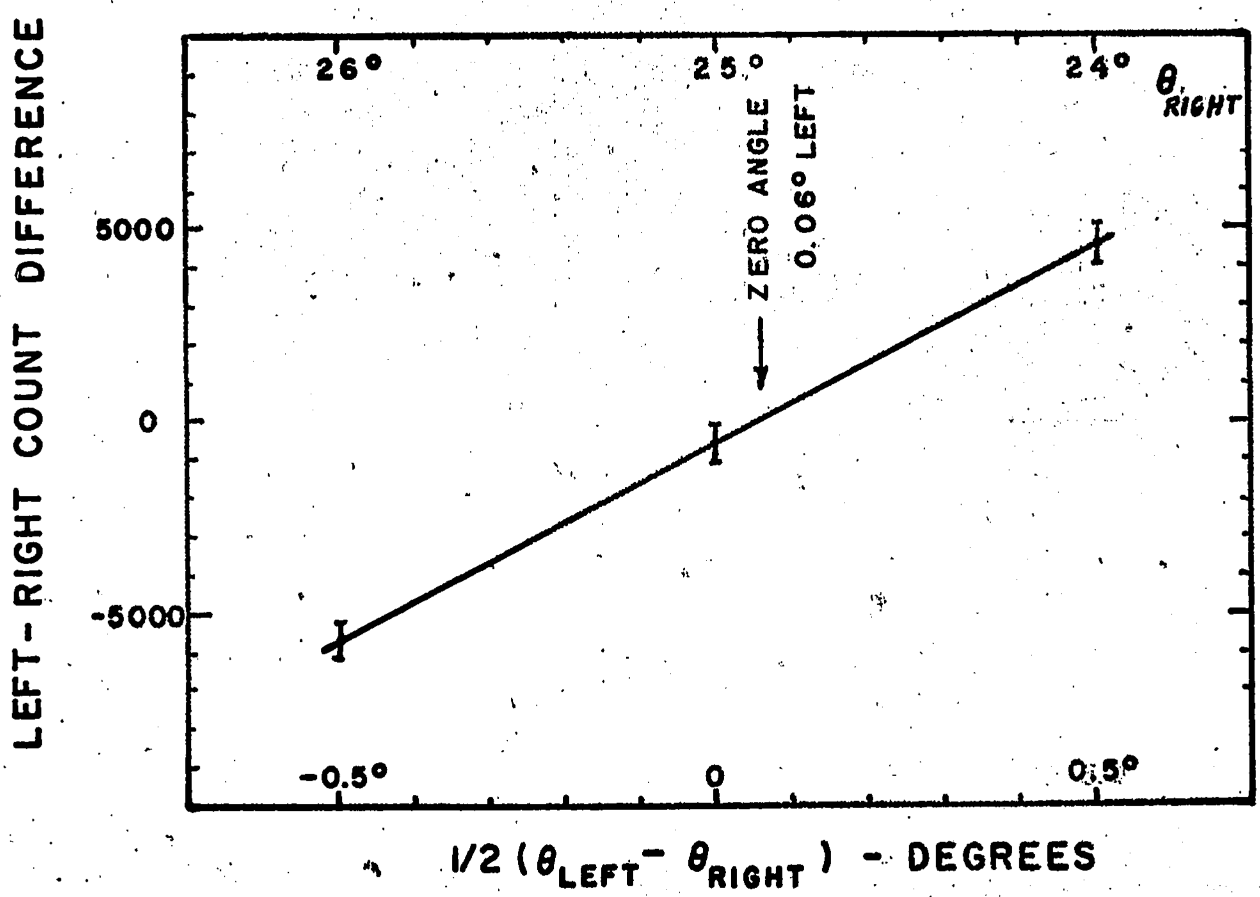
LEFT-RIGHT COUNT DIFFERENCE
5000
0
-5000
26°
25°
24°
θ_{RIGHT}
ZERO ANGLE
0.06° LEFT
-0.5°
0
0.5°
1/2 (θ_{LEFT} - θ_{RIGHT}) - DEGREES

FIGURE 13

ΔE SPECTRA FOR PROTONS, DEUTERONS AND TRITONS FROM A CARBON TARGET AT 30°

FIGURE 13

ΔE spectra are shown for protons, deuterons and tritons from a carbon target at 30°. The spectra were accumulated with magnet settings appropriate to central path rigidities for 90 MeV protons, 75 MeV deuterons and 70 MeV tritons respectively. The lowest ΔE discriminator level was used in each case. The scales (in arbitary units) give an indication of the relative cross-sections.

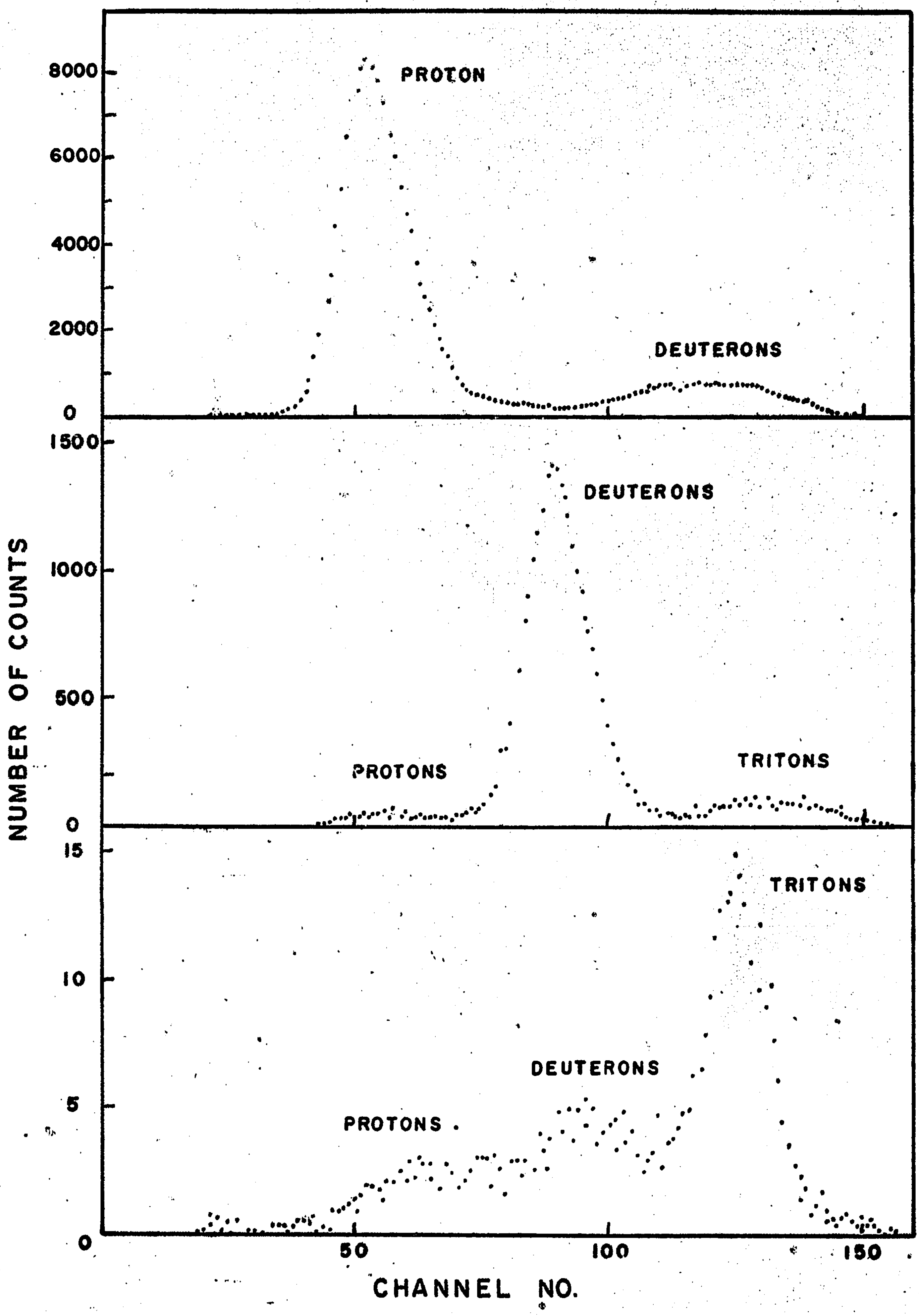

PROTON
DEUTERONS
DEUTERONS
PROTONS
TRITONS
TRITONS
DEUTERONS
PROTONS
NUMBER OF COUNTS
CHANNEL NO.
8000
6000
4000
2000
0
1500
1000
500
0
15
10
5
0
50
100
150

FIGURE 14

TWO PARAMETER (E - ΔE) DISPLAYS FOR THE (p,d) AND (p,t) REACTIONS ON ^{6}Li.

FIGURE 14

Two parameter displays are shown of spectra accumulated for the (p,d) and (p,t) reactions on ^{6}Li at an angle of 15^{o} Lab. (Energy E extends to the right and ΔE extends backwards).

a) This displays the spectrum obtained with the magnet and ΔE discriminator set for deuterons from the $^{6}Li(p,d)^{5}Li$ reaction. The deuteron ridge is prominent at low ΔE, a ridge of tritons accepted by the magnetic selection appearing in the back.

b) This is the spectrum of (a) above, rotated in the memory through 180^{o} in order to show the tritons more clearly.

c) In this display the magnet and ΔE discriminator settings were appropriate to tritons from the $^{6}Li(p,t)^{4}Li$ reaction. The gain settings were unchanged from the previous displays. The integrated energy spectrum is also shown in the first row of channels.

a)

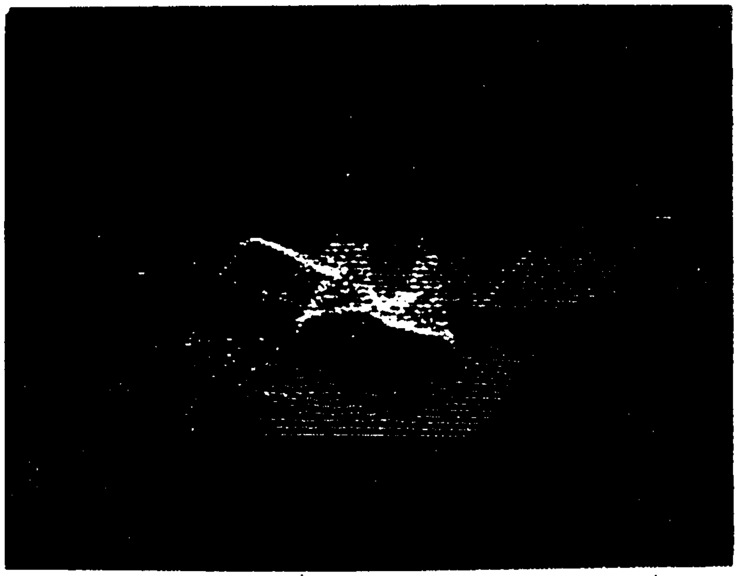

b)

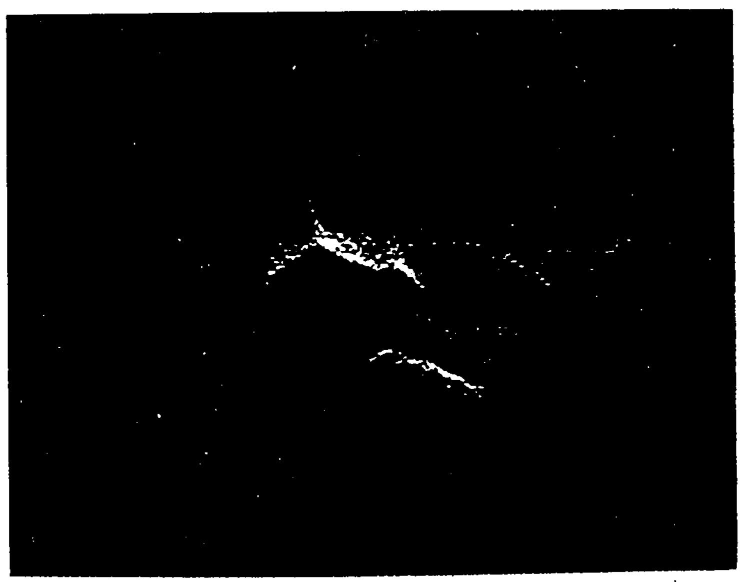

c)

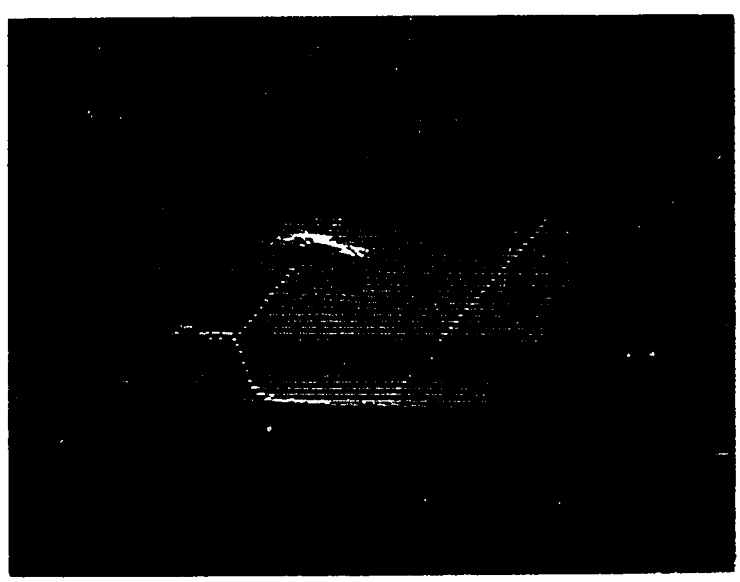

a)

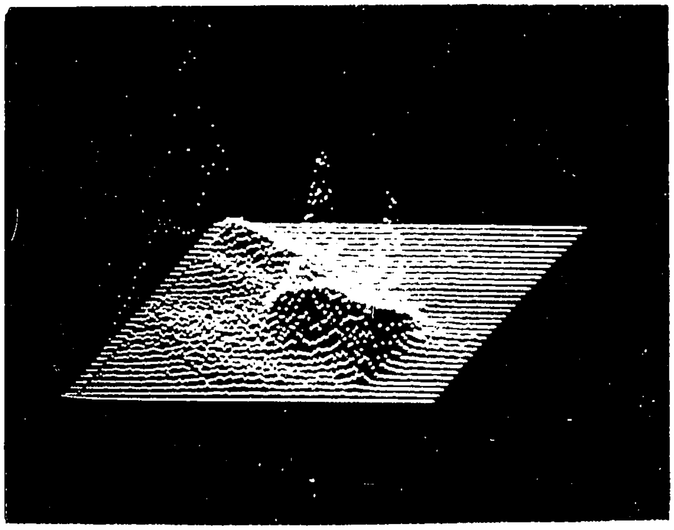

b)

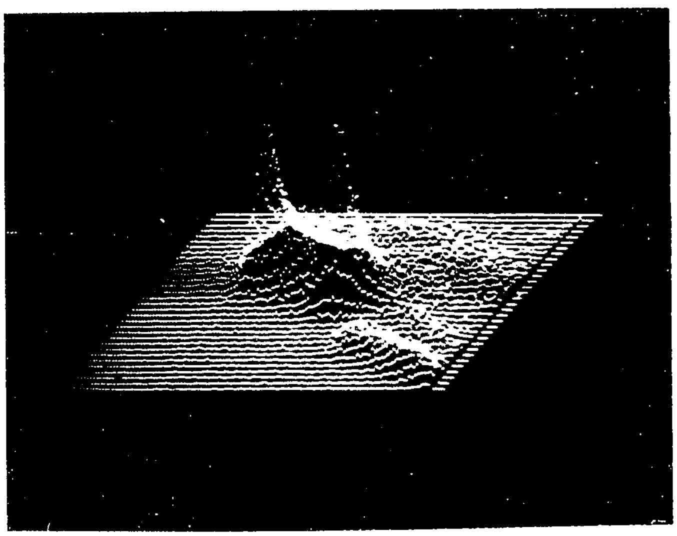

c)

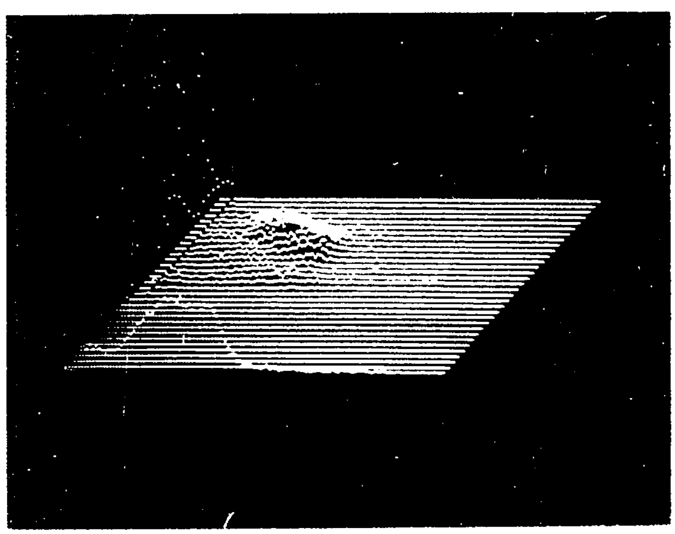

FIGURE 15

MORE TWO PARAMETER DISPLAYS

FIGURE 15

Additional two parameter spectra are shown for:

a) The triton spectrum from the reaction $^{7}Li(p,t)^{5}Li$ at 5^{o} Lab., illustrating the negligible deuteron feed-through in the region of interest.

b) A proton spectrum from carbon at 30^{o} Lab., illustrating the excellent separation of protons from the deuterons accepted by the magnetic selection.

a)

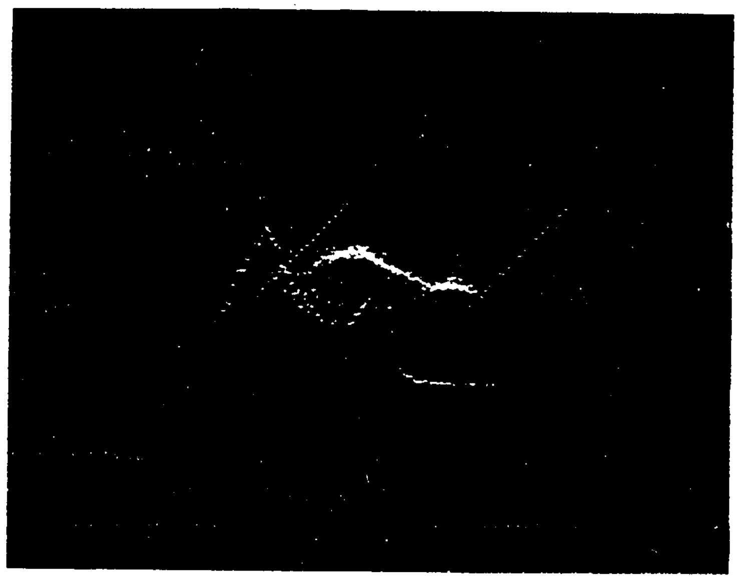

b)

a)

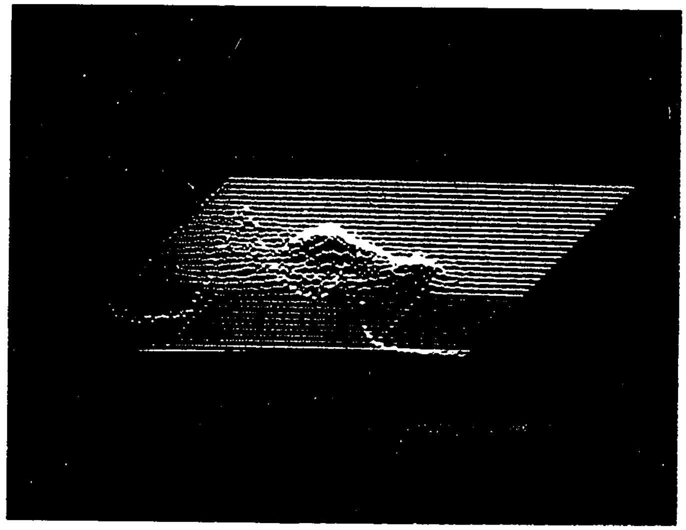

b)

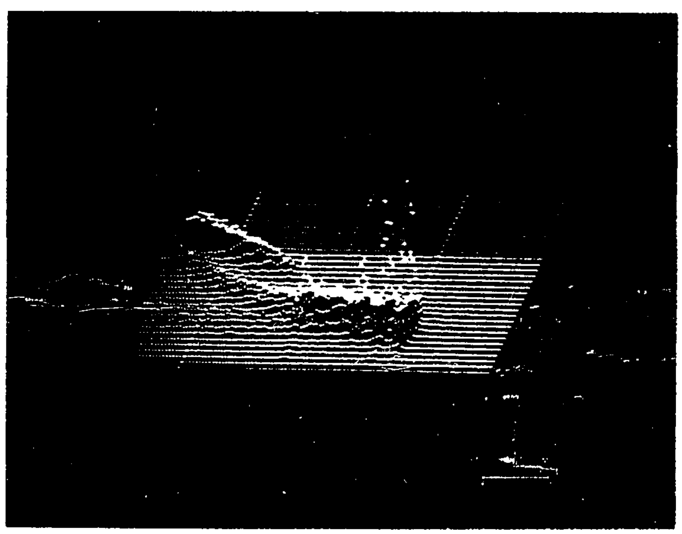

CHAPTER 4. DATA REDUCTION AND DISCUSSION OF ERRORS

4.1. Calculation of Cross-Sections:

The differential scattering cross-section is defined by:

$$\frac{d\sigma}{d\Omega} = \frac{N}{n\, N_I\, d\Omega}$$

where N/N_I is the fraction of the incident particles scattered into the solid angle $d\Omega$ by n scattering centres per unit area.

For the determination of the experimental differential cross-sections presented in the next chapter, this can be rewritten:

$$\frac{d\sigma}{d\Omega} = \frac{N\cos\theta}{Q}\left[\frac{1}{d\Omega\left(\frac{\rho t}{A}\right)\left(\frac{1}{e}\right)}\right]$$

where:

N is the number of scattered particles detected, leaving the residual nucleus in a particular state.

Q is the integrated charge in coulombs of the incident proton beam.

e is the proton charge (1.60×10^{-19} Coul.)

ρt is the target thickness (in gm/cm^2)

N_o is Avogadro's number (6.023×10^{23} atoms/gm. atomic weight)

A is the atomic weight of the target nucleus

θ is the angle between the target normal and the incident beam (not applicable to the helium target)

and $d\Omega$ is the solid angle subtended at the target centre by the defining counter of the detector telescope.

The quantity in brackets is a constant for each target, depending only on target thickness and detector geometry. The systematic errors associated with this constant, and the various corrections applied to the other experimental variables in the calculation of differential cross-sections are discussed, together with their associated uncertainties, in the following sections.

4.2 Corrections to Raw Data and Associated Uncertainties:

a) Determination of N;

The major corrections to the number N of observed particles were to compensate for counting rate losses and for absorption by the detectors. The only significant counting losses were due to the dead time of the multichannel analyser and the pulsed structure of the proton beam. The analyser dead time was considerably longer than the duration (10 μsec) of the cyclotron beam burst, allowing storage of only one information pulse per burst. Any subsequent pulses within the burst were lost. The correction for counting losses was determined experimentally by monitoring the coincidence output with a fast (100 MHz) scaler and comparing the number of coincidences (negligible dead time correction) with the summed counts in the analyser spectrum. This was checked by comparison with the calculated correction using the Cormack formula(Co62) for a long dead time circuit and a pulsed beam:

$$\lambda_2 t_o = 1 - e^{-\lambda_1 t_o}$$

where λ_2 and λ_1 were the observed and true counting rates and t_o the interval between beam bursts. The beam burst interval was obtained by continuous monitoring the cyclotron repetition rate. Agreement between experimental and calculated corrections was very good and the experimental corrections were used. These ranged from about 15% for counting rates of 150 sec^{-1} in the proton scattering experiments to 1% or 2% in the lower counting rate pick-up reactions.

Absorption in the detectors also introduced significant losses in the number of counts observed. Two processes contributed to this loss. A correction for the first, which was due to scattering of particles by the ΔE detector outside the acceptance of the E counter, was estimated using published carbon and hydrogen scattering cross-sections. For protons between 100 and 50 MeV (Ma66, Fa67, Br60) the calculated correction was less than 1% and for deuterons of 95MeV (Ba56, Po61) the correction was about 0.7%. Much more serious were losses due to nuclear interactions in the E counter itself. These inelastic processes produced substandard pulses, displacing counts to a lower energy in the spectrum. The correction for this effect is energy dependent and has been calculated over a wide range of energies by Measday (Me65, Me66) for protons, deuterons, and alphas incident on a plastic $(CH)_n$ counter. An experimental check of the correction for this effect was made with 100 MeV protons by placing the main counter telescope in the direct proton beam (with greatly reduced intensity). The spectrum thus obtained exhibited a low energy "tail" corresponding to losses from the peak due to nuclear interactions. In estimating the correction from the "tail" or continuum, a gaussian was fitted to the peak and a value of (14 $\pm$ .5)% was obtained. The uncertainty includes estimated errors in extrapolation of the tail at both ends of the spectrum and the statistical error. An earlier measurement using similar techniques, made in collaboration with Mark (Ma65) yielded a correction of (13.4 $\pm$ .3)% for a different plastic counter. This correction is considerably larger than the 9.8% correction tabulated by Measday (Me65). The discrepancy between the values can be attributed to the approximations used in Measday's calculations. Loss by elastic scattering out of the detector volume was ignored, and this has been shown (Go67) to contribute as much as 1.5% of the total for 100 MeV protons. Measday's calculations also assumed (somewhat arbitrarily) a cut off at 5 MeV, protons having to lose more than 5 MeV to be included as "lost". A similar demarcation in the experimental measurement described above would decrease the measured correction by 2.4%. Previous experimental measurements of the corrections for protons in a plastic scintillator were made at 40 and 68 MeV (Jo58) yielding corrections 7% lower and 14% higher respectively than the Measday values. The corrections finally used for the proton data were obtained by fitting a curve to the experimental points, while maintaining the same general shape as Measday's values. A systematic error of $\pm$ 1% was assigned for the uncertainty in this correction. No experimental data was available with which to compare Measday's deuteron corrections (Me66) for deuteron energies in the region of interest. One measurement at 26.8 MeV (Ei63) was about 20% higher than the corresponding calculated Measday value. Using somewhat less accurate cross-section data Postma and Wilson (Po61) also calculated the correction for nuclear interactions of deuterons in plastic scintillators and obtained corrections about 25% higher than those of Measday. The corrections finally used for the deuteron data were those tabulated by Measday (Me66) and a systematic uncertainty of $\pm$ 2% was assigned to this correction. Experimental data, either in the form of direct measurements of the absorption correction, or in the form of reaction cross-sections which would enable calculations (such as Measday's) of this correction, is not available for tritons of the energy range covered in this experiment. Consequently no corrections could be made to the triton counts for losses due to nuclear interactions in the counters or for outscattering from the ΔE scintillator. These corrections, which probably are of the order of 20 to 25% could easily be applied to the data at some future date, should they become available.

There were several additional, but smaller, corrections to the number of counts N. Chance rate and pile up corrections were always small and often negligible. Maximum chance rate, which never exceeded 4%, occurred in the (p,t) reactions at the forward angles, where it was enhanced by high singles rates in the counters (due to the beam stop background). In the few cases where the chance rate was high, a chance spectrum was obtained in addition to the normal energy spectrum. Pile-up corrections were also small, the most serious corrections ($<$ 4%) again occurring for the (p,t) reaction at small angles. Pile up corrections were made assuming Poisson statistics, and using information on the E pulse shape and singles rate which was checked at each angle. No systematic uncertainty was assumed for these corrections.

In the experiments with the lithium targets, background (checked by comparing spectra with the target in and the target out) was non-existent at angles larger than 30°. In the small angle region where the beam stop was used, background counting rates were sometimes quite appreciable, but in all cases contributed only to a part of the spectrum outside the region of interest. In the case of the helium target, the target cylinder and aluminum heat shield contributed a background to the entire spectrum, and it was necessary to repeat each helium run with an empty target. The corrections obtained for the scattering from the empty target ranged from about 5% for the inelastic region of the proton and deuteron spectra to less than 3% in the (p,t) spectra and 1% in the elastic proton scattering peak. Errors introduced by this correction were negligible.

There were also several sources of relative error in the determination of N. In general the method used to obtain N was to fit a gaussian at the peak position (On61). This was straight forward for the proton spectra, except in the case of weakly excited inelastic states, where error assignments as large as 20% to 30% were sometimes necessary. The estimation of N for the (often poorly defined) ground state peaks in the ^{6}Li (p,t) ^{4}Li and ^{7}Li (p,t)^{5}Li reactions and to a much lesser extent in the ^{6}Li (p,d)^{5}Li reaction was however subject to a large possible systematic error. The peaks were fitted systematically by requiring consistency in the peak widths, and relative errors typically $\pm$ 4%, were assigned on the basis of this fitting. It is very difficult to make more than a qualitative statement about the uncertainty in the absolute value of the cross-sections introduced by the method used to estimate N. The cross-sections may conceivably be as much as 50% too high.

A similar uncertainty exists in the absolute values of the cross-sections for inelastic scattering from the excited states of ^{6}Li and ^{7}Li. All the levels analysed in the next chapter were unbound and therefore above the threshold for three-body breakup. The calculated cross-sections contain an unknown contribution from this three body continuum , which was most pronounced at the backward angles.

The statistical errors varied considerably, from less than 1% for elastic proton scattering to a few percent for the other reactions studied. Data was unsually accumulated until a statistical accuracy of 2% or better was obtained.

b) Determination of Q:

Both the primary and the calibration Faraday cups were designed to minimize errors in beam current measurement. Error due to ionization of the residual gas was negligible at the pressures used (Ki65) and errors due to backscattered electrons were estimated to be less than 0.2%. An r.m.s. error of $\pm$ 0.5% was assumed for the calibration of the primary Faraday cup against the calibration cup. This error arose mainly from the inadequate intermediate monitor used (described in a previous section). The systematic error associated with the calibration cup itself was probably very small and was assumed to be $\pm$ 0.4%. The current integrator was calibrated several times during each run with the Keithley picoampere source, indicating corrections of the order of 1 or 2 percent. No r.m.s. error was associated with this correction. The picoampere source was itself calibrated absolutely at the beginning and at the end of the experiment, the corrections being (1.1 $\pm$ .3)% and (1.4 $\pm$ .3)% respectively. At small angles the charge Q was determined by the use of a secondary monitor, the monitor telescope and additional corrections were necessary. Corrections for monitor telescope background counts (due to the beam stop) were usually less than 0.4%. Monitor telescope variations, due to counting rate effects and the effect of the fringing magnet field were frequently checked and found to be small. Shifts of the zero scattering angle produced a change in monitor counting rate of about 1% per degree. A total r.m.s. error of $\pm$ 0.5% was assumed for all these effects. A systematic error of $\pm$ 0.5% was assigned to the calibration of the monitor telescope relative to the Faraday cup. At the smallest scattering angles, monitor counter statistics also contributed to the relative errors.

c) Determination of target thickness (ρt):

The thickness of the lithium targets was determined to an accuracy of about $\pm$ 0.4% from the average of a number of measurements using a micrometer gauge. The target uniformity was estimated to be within this uncertainty. The thickness in gm/cm^2 (ρt) was then obtained by using the density given in the Handbook of Chemistry and Physics (Mo62). A direct measurement of the density would probably have been less accurate, due to difficulties in correcting for non-uniformities in thickness over a larger area, especially at the target edges and also to the uncertainty introduced in the weight by a residual oil film. (The targets were stored in mineral oil to minimize oxidation). The high malleability of lithium and the method of rolling the targets ensured uniformity and freedom from voids, as verified by inspection. The effective target thickness also depended on the orientation of the target, which was chosen so as to minimize the energy spread in the detected particles due to energy degradation in the target. The uncertainty in the determination of the target angle with respect to the beam direction was about $\pm$ 0.2^{o} and this introduced a variable error, depending on the target angle, of less than 0.4% in the estimation of the target thickness. The isotopic impurity (.7% ^{7}Li) of the ^{6}Li target introduced a small and uncertain error in the determination of the target thickness. No correction was made for the ^{7}Li impurity and instead a systematic uncertainty of $\pm$ 0.4% was assumed. Deterioration of the lithium targets by oxidation was not serious and oxygen and nitrogen contamination were believed to be negligible.

Determination of the thickness of the helium target involved several corrections. The initial thickness (ρt) was calculated using the internal diameter of the target cylinder (measured with an accuracy of about $\pm$ .1%) and the density (0.125 gm/cm^{3}) of liquid helium at its normal boiling point (Ke42). Two corrections to the cylinder dimensions were necessary under running conditions: the first to correct for expansion due to the one atmosphere pressure differential and the second to compensate for thermal contraction due to the low helium temperature. These corrections were calculated using the manufacturer's quoted properties of H-film (Dupont Bulletin H-2), reasonable extrapolations being necessary for some properties. The effects of the aluminum end sections of the target finger were ignored. The elongation of the target cylinder circumference due to the pressure differential was estimated to be 1.8% and the thermal contraction 0.6%. A systematic uncertainty of $\pm$ 0.2% was assumed for these corrections.

An additional consideration in determining the target thickness involved the accuracy of alignment of the beam on the target centre and the subsequent stability of the beam position. Allowing for small beam shifts of $\pm$0.5 mm and the finite beam size a relative or r.m.s. error of $\pm$0.5% was assigned to the target thickness. The beam spot size was somewhat larger (probably 2 to 3 mm in diameter) in the helium experiments than in the experiments using the lithium targets, due to the inability to focus the beam directly at the target position. The effect of the finite beam size alone also introduced a systematic uncertainty of about $\pm$ 0.3% in the target thickness due to its small radius of curvature.

Finally, the effective target thickness could have been reduced by excessive evaporation of helium along the beam path. An accurate estimate of this effect was difficult because of the assumptions required in making the calculations. The energy loss sustained by the proton beam in traversing the target contributed an evaporation rate of about 2cc/hour per nanoamp. Assuming that all evaporation took place within the beam path, that the gas formed did not contribute to the reaction and that the clearing time for the bubbles produced was 0.1 sec., the reduction in the effective target thickness was about 0.1% per nanoamp. The first assumption is most unlikely, since conduction and convection in the liquid helium would tend to disperse the heating produced by the beam. The second assumption is essentially correct since the density of gaseous helium at liquid temperature is about 10% of the liquid density (Ho61). The third assumption is difficult to substantiate, but seems reasonable. More realistic estimates for the first (and to a much lesser extent the second) assumption would therefore reduce the effect of evaporation to a negligible consideration. Nevertheless an additional systematic uncertainty of $\pm$ .3% was assumed for this effect.

d) Determination of the Solid Angle $d\Omega$:

The solid angle was determined by projecting the area of the ΔE (defining counter) scintillator back through the magnet to the target, using the matrix techniques described in Appendix II. This procedure was necessary to correct for focussing in the horizontal plane introduced by the wedge magnet. The solid angle obtained was $(5.3 \pm 0.4)\%$ larger than that determined directly by dividing the detector area by the square of the target to detector central path distance. The uncertainty in this correction arises from a possible $\pm 0.5^{\circ}$ misalignment of the pole tip entry angle. Additional systematic uncertainties include contributions of $\pm$ 0.2% for the determination of the ΔE scintillator area, $\pm$ 0.4% for the measurement of the central path distance and $\pm$ 0.3% for focussing effects in the vertical plane also due to the possible misalignment of the pole tip. An additional relative error of $\pm$ 0.5% was assumed to allow for the different detected particle path lengths.

The solid angle was also determined experimentally as a check on the calculated value above. The differential cross-section for scattering from carbon was measured very carefully at 30° Lab with both the main detector telescope and the monitor detector telescope. Determination of the scattering angles was critical and consequently the zero angle was measured to an accuracy of $\pm$ $.1^{\circ}$ for each detector. The cross-section for elastic scattering (and excitation of the 4.43 MeV level) at 30° was then obtained for the main counter telescope and the procedure repeated for the monitor telescope at angles of 29°, 30°, and 31° to permit interpolation to compensate for different zero angles. The solid angle of the monitor telescope was determined from the geometry to an accuracy of $\pm$ 0.4%. The corresponding solid angle for the main detector was then estimated and found to differ from the geometrical solid angle by + (6.6 $\pm$ 2)%, the error being mainly due to angle uncertainties of the order of $\pm$ 0.1°. This is in good agreement with the calculated correction to the solid angle.

e) Summary of Errors in Data Reduction:

A summary of the worst case systematic errors for each reaction studied is presented in Table I. These uncertainties are the linear sum of all the individual systematic errors. The relative errors which were treated as r.m.s. errors and added in quadrature have been tabulated with the differential cross-sections for each reaction in the next chapter.

Table I

Summary of Systematic Uncertainties in Differential Cross-Sections

	Uncertainty in %				
Reaction	N	Q	t	d	Total
$^{6}Li(p,p)^{6}Li$	1.0	1.4	0.8	1.3	4.5
$^{7}Li(p,p)^{7}Li$	1.0	1.4	0.4	1.3	4.1
$^{6}Li(p,d)^{5}Li$ (b)	2.0	1.4	0.8	1.3	5.5
$^{6}Li(p,t)^{4}Li$ (b)	a	1.4	0.8	1.3	3.5
$^{7}Li(p,t)^{5}Li$ (b)	a	1.4	0.4	1.3	3.1
$^{4}He(p,p')^{4}He$*	1.0	1.4	0.9	1.3	4.6
$^{4}He(p,d)^{3}$ He*	2.0	1.4	0.9	1.3	5.6
$^{4}He(p,t)2p$	a	1.4	0.9	1.3	3.6

Note: a) no corrections were available for triton losses in the counters due to nuclear interactions, and so no correction was made.

b) a possible large judgement error in fitting the triton (and deuteron) ground state peaks has been discussed in a).

4.3 Angular Uncertainty:

There were three sources of possible error in the determination of the scattering angle; the error in reading the angular scale, uncertainty in the zero angle and the uncertainty in the position of the actual trajectory of the detected particle relative to the central path. The accuracy with which the angular setting was made (which included possible errors in the original marking of the angular scale) was estimated to be $\pm 0.1^{\circ}$. The uncertainty in the zero angle contained contributions from the angular uncertainties involved in the zero angle measurement and from statistics and was estimated to be about $\pm 0.2^{\circ}$. The total angular acceptance of the magnet slits was 0.8° (for full transmission) and the uncertainty in determining the actual entry position of the detected particle was estimated to be $\pm 0.1^{\circ}$. The total r.m.s. error in the angular position was therefore $\pm 0.25^{\circ}$. This uncertainty could be considered as an equivalent error in the differential cross-section by translating the angular uncertainty to a cross-section error. This was done only in the case of the proton elastic scattering on ^{6}Li and ^{7}Li for the optical model analysis discussed in a subsequent chapter. The r.m.s. errors tabulated with the cross-section in the next chapter do not contain contributions from the angular uncertainty. Finally, the angular uncertainty was somewhat larger for the measurements made in the backward angle region, where the scattering chamber had to be rotated about its axis by 180°. The chamber was rotated to an accuracy of better than $\pm 0.05^{\circ}$ by using a theodolite to check alignment. In this angular region (approximately 110° to 150°) experimental difficulties precluded the determination of the zero angle by the standard method. Making use of the consistency in zero angle measurements at small angles, the zero angle in this angular range was estimated from the alignment procedure to an accuracy of $\pm 0.4^{\circ}$. The total r.m.s. uncertainty in the angle was then $\pm 0.42^{\circ}$ in the backward angle region.

4.4 Angular Resolution:

The angle subtended at the target by the defining counter (ΔE scintillator) was 0.6° and was the main contribution to the angular resolution. Additional smaller contributions came from the beam divergence ($< 0.3^{\circ}$), from the size of the beam spot at the target (this was somewhat more serious for the helium target) and from multiple scattering ($< .2^{\circ}$). Beam drift of a short term nature was found to be negligible and so did not contribute to the angular resolution. The total r.m.s. angular resolution was therefore less than 0.7° for the experiments using lithium targets and as high as about 1.1° with the helium target. The most serious effect of the finite angular resolution was kinematic broadening, resulting in inferior energy resolution. Another consequence of finite angular resolution is the difficulty introduced in interpreting the differential cross-section in a region of rapid change. This was not a problem in the present experiment.

CHAPTER 5. EXPERIMENTAL RESULTS AND DISCUSSION

5.1 Elastic and Inelastic Scattering from ^{6}Li:

a) Experimental Results:

Data for the elastic and inelastic scattering from ^{6}Li was collected over an angular range from 4.5^{o} lab, to 150.1^{o} lab. The measurements up to 120^{o} were made with the analyser magnet and main counter telescope. At the larger angles, because of physical limitations in the angular range of the magnet, it was necessary to use the monitor counter telescope for cross-section measurements. The only modification was simply the interchange of the functions of the two counter telescopes, which was accomplished by interchanging the electronics. Measurements were also made with the monitor counter at smaller angles to check for possible systematic errors. Differences between the cross-sections measured with the two counter systems, were within the estimated uncertainties.

Some typical energy spectra are shown in fig. 16. The elastic peak was quite well resolved throughout the angular range covered, the energy resolution being typically 1.3 to 1.4 MeV. Wherever necessary, gaussian paper (On61) was used to facilitate separation from the first excited state. The only peaks in the spectrum other than the elastic peak, which could be resolved, were those corresponding to the first excited 2.184 MeV state and second excited 3.562 MeV state. The 3.56 MeV state (0^{+}, T=1) was quite strongly excited at small angles, but the cross-section decreased rapidly with angle and by 15^{o} (lab.) it was impossible to resolve the peak from neighbouring levels. The first excited state at 2.18 MeV (3^+, T=0) was prominent over almost the entire angular range and was quite easily resolved from both the elastic peak and the higher energy levels, although, again, gaussian analysis was necessary in many cases. A broad peak at an excitation of approximately 5 MeV was also observed for angles larger than about 20^o lab. This peak most probably corresponds to excitation of the known levels (La66) at 4.57 MeV (2^+, T=0) and 5.36 MeV (T=1) although excitation of a broad level (Aj59) at 5.5 MeV (1^+, T=0) is also possible. These levels could not be resolved in the present experiment. No other distinct peaks were observed in the spectrum above the three body break-up continuum. In evaluating the peak areas for the first two excited states, no correction was made for the background introduced by the three body break-up $^6Li(p,pd)^4He$ (threshold at 1.47 MeV target excitation) since an estimation of this correction would have been difficult and quite uncertain. It is possible that this may have introduced an additional systematic error of up to +10% at large angles. A correction was applied, however, for the contribution of the continuum due to reactions induced in the detector by the elastically scattered protons. This correction was estimated from the spectrum obtained with the detector in the direct beam in the earlier determination of absorption losses in the counter.

The differential cross-sections calculated for the elastic scattering are tabulated together with the total r m s errors for both the lab. and centre of mass systems in Table 2. A similar compilation of results for the excitation of the 2.18 MeV and 3.56 MeV levels is presented in Tables 3 and 4 respectively.

The angular distributions in the centre of mass systems for the elastically and inelastically scattered proton groups are shown in fig.17.

b) Discussion:

Elastic scattering of protons on ^{6}Li has been studied previously at 31 MeV (De63), at 40 MeV (Ch60) and at 155 MeV (Ta64). The angular distribution obtained for the present results (at 100 MeV) has the same general features as the distribution obtained at Orsay with 155 MeV protons; the lower energy angular distributions having stronger diffraction oscillations. The main features of the angular distribution are the Coulomb interference at about 6^{o} (cm); a small diffraction dip at about 45^{o}(cm) and a general decrease in cross-section with increasing angle, leveling off at about 100^{o} (cm). An optical model analysis of the elastic scattering is presented in a later section.

Inelastic scattering has been investigated in the energy region from 30 MeV to 185 MeV by a number of groups (De63, Ch58, Cl61, Ja63, Ja64, Ha64, Ha65). The results obtained in this experiment can best be compared with the data of the Orsay group (Ja64) obtained at 155 MeV, and of the Uppsala group (Ha65) obtained at 185 MeV. Both groups observed the excitation of four levels in ^{6}Li. In addition to the 2.18 MeV and 3.56 MeV states observed in the present experiment, levels at

4.5 MeV and 5.5 MeV were resolved. The angular distributions presented for this data were very similar to those obtained here at 100 MeV. The shape of the angular distributions for the 4.5 and 5.5 MeV levels was the same as that of the 2.2 MeV state being broadly peaked at about 18° lab. All three levels correspond to an E2 excitation. The cross-section for the 2.18 MeV level decreases uniformly with increasing proton energy, the peak value being (in the lab. system) $\sim$ 8 mb/ster. at 100 MeV, $\sim$ 5.4 mb/ster. at 155 MeV, and $\sim$ 3.6 mb/ster. at 185 MeV. This is consistent with the theoretical energy dependence of differential cross-sections (Le58). Jacmart et al (Ja64) compare their angular distribution for the 2.18 MeV level with the distribution obtained from electron scattering (Be63) and a theoretical calculation by Jackson (Ja62) based on the impulse approximation and the shell model. The absolute values predicted by the theory were found to be low and this was interpreted by Jacmart as an indication of the cluster structure (α + d) of ^{6}Li. The cluster model which would lead to a similar shaped angular distribution but with higher cross-sections, would also account for the zero isospin levels at 4.5 MeV ($J^{\pi} = 2^{+}$) and 5.5 MeV (1^{+}) which together with the 2.18 MeV (3^{+}, T = 0) state of ^{6}Li constitute a triplet corresponding to an (α + d) cluster with relative angular momentum $\ell = 2$. The (α + d) cluster model for ^{6}Li has been employed successfully to interpret the ^{6}Li(p,pd)^{4}He reaction (Ru62).

The angular distribution for the 3.56 MeV level which corresponds to an M1 excitation was strongly peaked at small angles for all three energies. It was fitted theoretically by Jackson and Mahalanabis

(Ja65) at 155 MeV. The present results have a somewhat higher cross-section, but the same shape as those at the higher energies. Thomson and Tang (Th67) using the method of resonating-group structure have recently predicted several levels in ^{6}Li between 6 and 10 MeV with a (^{3}He + ^{3}H) cluster structure. No peaks were observed in this energy range in the present experiment although Hasselgren (Ha65) reported the possible observation of levels at 6.5 and 7.5 MeV with a maximum cross-section of 0.4 mb/ster.

TABLE 2

DIFFERENTIAL CROSS-SECTIONS FOR THE ELASTIC SCATTERING OF PROTONS ON ^6Li

Lab Angle degrees	$\frac{d\sigma}{d\Omega}$ lab mb /ster.	c.m. Angle degrees	$\frac{d\sigma}{d\Omega}$ cm mb / ster.
4.5	195 ± 2	4.8	139 ± 2
5.5	160 ± 2	6.0	115 ± 1
6.5	171 ± 2	7.7	123 ± 1
7.9	182 ± 2	9.3	131 ± 1
10.4	183 ± 2	12.3	132 ± 1
13.0	153 ± 2	15.4	110 ± 1
15.6	111 ± 1	18.4	80.2 ± .7
20.6	52.2 ± .4	24.3	38.3 ± .3
25.6	18.8 ± .1	30.1	14.0 ± .1
30.6	5.70 ± .04	35.9	4.31 ± .03
35.6	1.89 ± .02	41.7	1.45 ± .01
40.6	.877 ± .008	47.4	.690 ± .006
45.4	.548 ± .006	52.8	.440 ± .005
50.6	.316 ± .004	58.7	.261 ± .004
60.4	.0840 ± .0014	69.5	.0732 ± .0012
75.4	.00411 ± .00028	85.5	.00392 ± .00022
90.6	.00120 ± .00015	101.0	.00126 ± .00016
105.6	.00141 ± .00017	115.6	.00162 ± .00020
120.6	.000819 ± .000108	129.4	.00103 ± .00013
135.1	.000922 ± .000097	142.3	.00124 ± .00013
150.1	.000980 ± .000103	155.2	.00139 ± .00015

Note: The above errors are r m s errors. There is an additional systematic error of ± 4.5%.

TABLE 3

DIFFERENTIAL CROSS-SECTIONS FOR THE EXCITATION OF THE 2.184 MeV STATE IN ^{6}Li.

Lab Angle degrees	$\frac{d\sigma}{d\Omega}$ lab mb / ster.	c.m. Angle degrees	$\frac{d\sigma}{d\Omega}$ cm mb / ster.
6.4	3.9 ± 1.2	7.6	2.8 ± .8
7.8	4.7 ± 1.4	9.2	3.3 ± 1.0
10.3	6.0 ± 1.5	12.2	4.3 ± 1.1
12.9	7.90 ± .79	15.3	5.69 ± .57
15.5	7.65 ± .38	18.3	5.53 ± .28
20.5	7.16 ± .36	24.2	5.23 ± .26
25.5	5.19 ± .15	30.1	3.85 ± .12
30.5	3.27 ± .06	35.9	2.46 ± .05
35.5	2.03 ± .02	41.6	1.56 ± .02
40.5	1.29 ± .05	47.4	1.01 ± .04
45.3	.831 ± .025	52.8	.666 ± .020
50.5	.560 ± .011	58.7	.461 ± .009
60.3	.265 ± .005	69.5	.231 ± .005
75.2	.0444 ± .0009	85.4	.0423 ± .0009
90.4	.00826 ± .00050	100.9	.00869 ± .00052
105.4	.00645 ± .00032	115.5	.00746 ± .00037
120.4	.00449 ± .00024	129.6	.00565 ± .00031
134.9	.00363 ± .00029	142.2	.00490 ± .00039
149.9	.00325 ± .00026	155.1	.00463 ± .00038

Note: a) The errors tabulated above are r m s errors.

b) The total systematic error for these measurements is ± 4.5%. An additional systematic error introduced by not correcting for the continuum is discussed in the text.

TABLE 4

DIFFERENTIAL CROSS-SECTIONS FOR THE EXCITATION OF THE 3.56 MeV STATE IN ^{6}Li.

Lab Angle degrees	$\frac{d\sigma}{d\Omega}$ lab. mb/ster.	c.m. Angle degrees	$\frac{d\sigma}{d\Omega}$ c.m. mb/ster.
4.3	13.6 $\pm$ 1.4	5.1	9.68 $\pm$ .97
5.3	11.1 $\pm$ 1.1	6.3	7.90 $\pm$ .79
6.3	9.70 $\pm$ .97	7.5	6.91 $\pm$ .69
7.7	8.09 $\pm$ .81	9.1	5.77 $\pm$ .58
10.2	6.75 $\pm$ .78	12.1	4.83 $\pm$ .54
12.8	6.5 $\pm$ 1.3	15.2	4.64 $\pm$ .92
15.4	5.3 $\pm$ 1.1	18.4	3.85 $\pm$ .77

Note: a) the errors tabulated above are the r m s errors.

b) the total systematic error for these measurements is $\pm$ 4.5%. An additional systematic error introduced by not correcting for the continuum is discussed in the text.

FIGURE 16

ENERGY SPECTRA OF PROTONS SCATTERED FROM ^{6}Li

FIGURE 16

Typical proton spectra from the $^6Li(p,p')^6Li$ reaction are shown for several lab angles. The energy level scheme for ^6Li is shown with each spectrum. The error bars shown are for relative uncertainties.

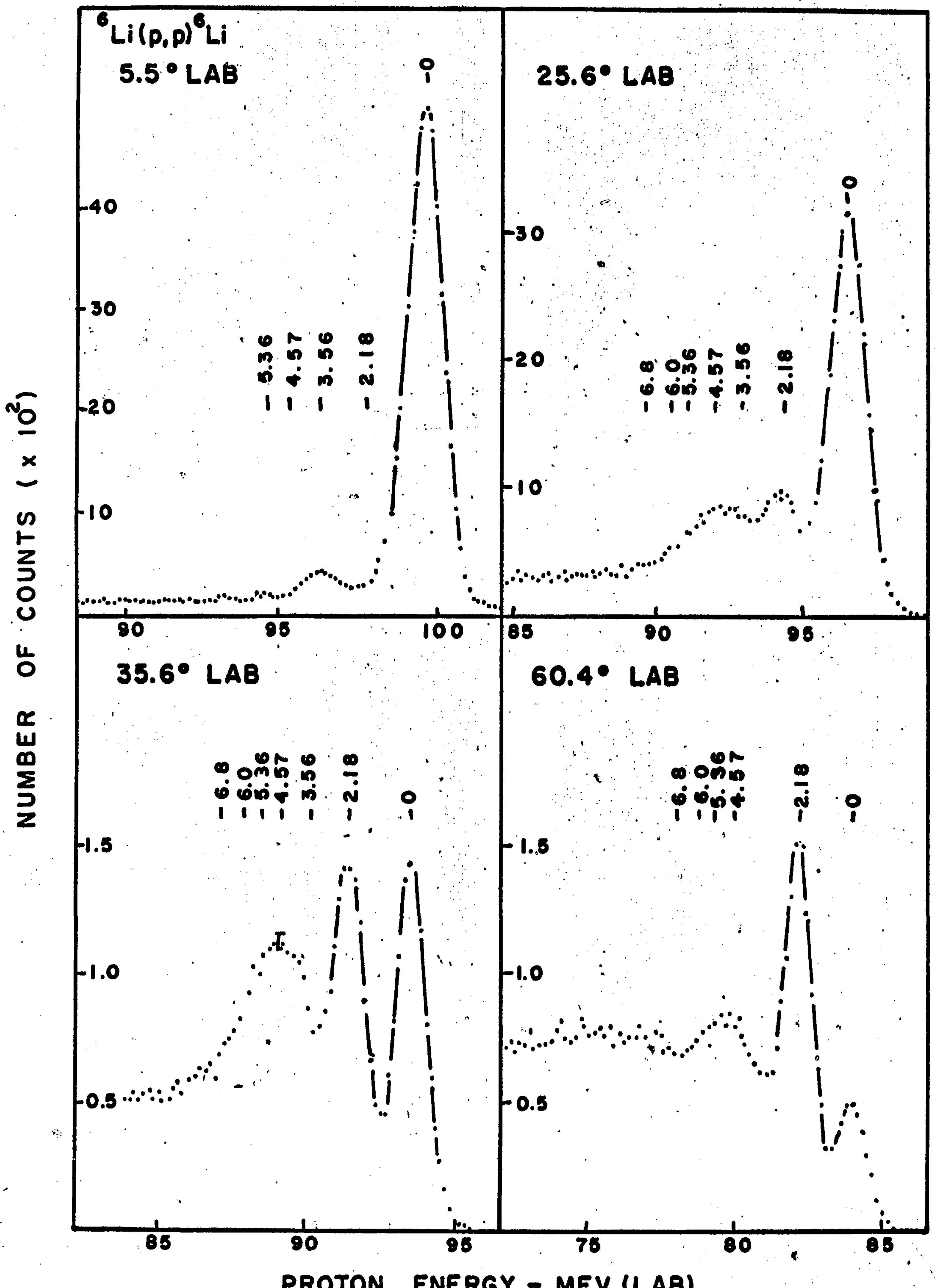

$^6Li(p,p)^6Li$
5.5° LAB
25.6° LAB
35.6° LAB
60.4° LAB
0
2.18
3.56
4.57
5.36
6.0
6.8
NUMBER OF COUNTS (x 10^2)
10
20
30
40
0.5
1.0
1.5
75
80
85
90
95
100
PROTON ENERGY - MEV (LAB)

FIGURE 17

ANGULAR DISTRIBUTIONS FOR ELASTIC AND INELASTIC PROTON GROUPS SCATTERED FROM ^{6}Li

FIGURE 17

Angular distributions for the elastic scattering from ^6Li and for the excitation of the 2.18 MeV and 3.56 MeV states. The coordinates are in the centre-of-mass system. The error bars shown are for relative uncertainties.

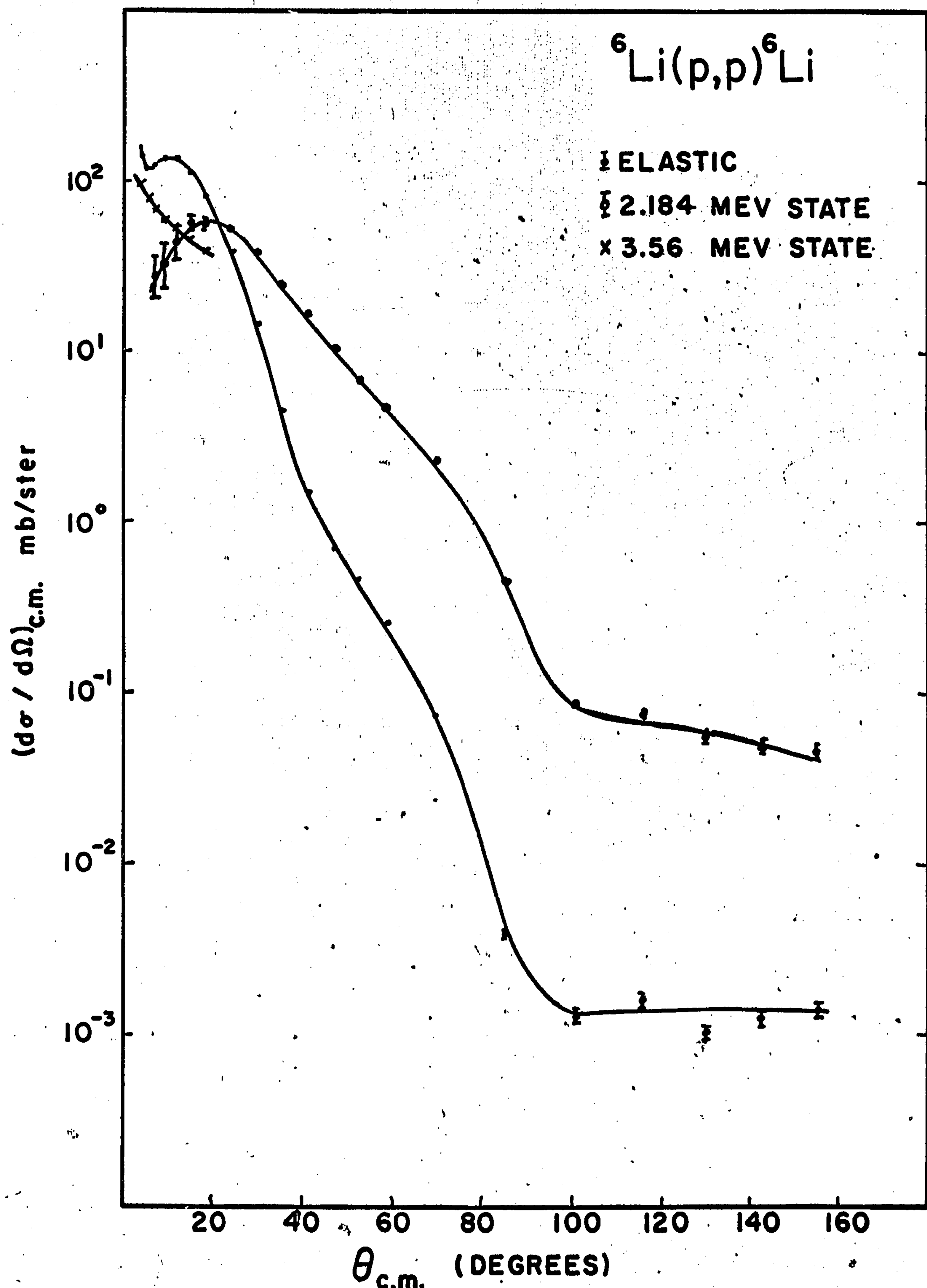

$^6Li(p,p)^6Li$
ELASTIC
2.184 MEV STATE
3.56 MEV STATE
10^2
10^1
10^0
10^{-1}
10^{-2}
10^{-3}
$(d\sigma / d\Omega)_{c.m.}$ mb/ster
20
40
60
80
100
120
140
160
$\theta_{c.m.}$ (DEGREES)

5.2. Elastic and Inelastic Scattering from ^{7}Li:

a) Experimental Results:

Data for the elastic and inelastic scattering from ^{7}Li was obtained concurrently with the ^{6}Li data described in the previous section, the ^{7}Li and ^{6}Li targets being alternated at each angle. Consequently the experimental procedure and angular range covered were the same. Typical energy spectra are shown in fig. 18. The elastic peak was unresolved from the 0.48 MeV ($\frac{1}{2}^-$, $T = \frac{1}{2}$) first excited state, but was well separated from the 4.63 MeV ($\frac{7}{2}^-$, $T = \frac{1}{2}$) second excited state over the entire angular range studied. The 4.63 MeV level was the most prominently excited inelastic state. Excitation of the broad 6.56 MeV ($\frac{5}{2}^-$, $T = \frac{1}{2}$) level was also observed, and there was some structure in the spectrum at an excitation corresponding to the 7.42 MeV level, which appeared as a small shoulder on the low energy side of the 6.56 MeV peak at large angles. Separation of the 4.63 MeV peak from the 6.56 MeV peak was achieved by the use of gaussian paper. The estimation of the 6.56 MeV peak area was considerably more uncertain and was unusually accomplished by fitting a gaussian curve at the peak position with the energy resolution determined from the more prominent elastic and 4.63 MeV peaks. As in the case of the ^{6}Li analysis, no correction was made for the three-body break-up continuum. The threshold for the break-up (^{4}He + t) is a target nucleus excitation of 2.47 MeV and although the contribution from the continuum was quite small at small angles it could have introduced an error as large as $\pm$ 10 percent in the estimation of the 4.63 MeV peak area and a considerably larger error in the determination of the 6.56 MeV peak area. Corrections were made, however, for the continuum introduced by reactions induced in the detector by the elastically scattered protons (and in the case of the 6.5 MeV level also by protons from the 4.6 MeV state). In the determination of the elastic peak area, no attempt was made to correct for the contribution from the unresolved 0.48 MeV state, which appeared as a very slight broadening on the low energy side of the elastic peak.

The differential cross-sections for elastic scattering from ^{7}Li (containing some unknown contribution from the excitation of the 0.48 MeV state) are tabulated with the associated r m s errors in both lab. and c.m. systems in Table 5. The differential cross-sections and r m s errors for the inelastic scattering from the 4.63 MeV state and 6.56 MeV state are given in Tables 6 and 7 respectively.

The angular distributions in the centre of mass system for the elastic (including the 0.48 MeV level) and inelastic scattering of protons by ^{7}Li are shown in fig. 19.

b) Discussion:

The scattering of 100 MeV protons from ^{7}Li has already been studied in an earlier collaboration with Mark (Ma65, Ma66), using a natural lithium target. The investigation of scattering from ^{7}Li was repeated here with an isotopically enriched target, and over a larger angular range, primarily to remove the uncertainty introduced in the earlier results by the unknown contribution to the elastic and inelastic cross-sections from the ^{6}Li content. The data for elastic scattering from the earlier experiment has been included in the angular distribution of fig. 19 for comparison. Elastic scattering from ^{7}Li has also been investigated at 40 MeV (Ch60), at 155 MeV (Ta64), at 160 MeV (Jo60) and at 180 MeV (Jo61). The angular distributions obtained by the various groups for protons with energies of 100 MeV or greater are in general very similar. The Uppsala group (Jo60, Jo61) used natural lithium targets and only covered a limited angular range. The Orsay group (Ta64) also covered a limited angular range ($<55^{\circ}$) but used an enriched ^{7}Li target. Their resolution was sufficient to allow a determination of differential cross-sections for the 0.48 MeV state. It was observed that the angular distribution for this level, which peaked at about 20° lab, dropped more slowly than that for elastic scattering, and that for angles larger than about 40° lab the cross-sections for elastic scattering and the excitation of the 0.48 MeV level were of the same order of magnitude. The angular distribution for the .48 MeV level was in fair agreement with that obtained by Newton et al (Ne62) in a (p,p'γ) experiment. This result leaves the interpretation of the angular distribution obtained for the elastic scattering in this experiment in some doubt. A careful study of the resolution of the elastic peak did not reveal any significant broadening as might be expected when contributions to the peak from the two levels were equal. However, at angles larger than 50° the energy calibration tends to favour identification of the "elastic" peak with excitation of the 0.48 MeV level. In view of this conflicting evidence, the angular distribution was left unchanged and can only be considered as the combined cross-section for elastic scattering and excitation of the first excited state. At angles smaller than 40°, evidence from previous investigations (Ne62, Ta64) indicates that the contribution of the 0.48 MeV level to the elastic cross-section is less than about 3%. An optical model analysis of the elastic scattering is presented in a later section.

Inelastic scattering from ^{7}Li has been investigated quite extensively with 150 to 180 MeV protons (Ty58, Ne62, Ja63, Ja64, Ha65). The most prominently excited state reported by all groups was the 4.63 MeV ($\frac{7}{2}^{-}$) level. The angular distribution obtained in this experiment was similar in shape to those obtained at the higher energies, and at angles larger than about 20° lab, the angular distribution was, within experimental error, in agreement with the 100 MeV results previously reported (Ma65, Ma66). At smaller angles the cross-sections obtained here were somewhat lower than those of the earlier experiment. This difference can be almost exactly accounted for by the inclusion in the earlier data, of a contribution from the 3.56 MeV ^{6}Li level arising from the ^{6}Li content of the natural lithium target. The main effect of removing the ^{6}Li contribution was to reduce forward peaking in the angular distribution.

In addition to the 6.56 and 7.48 MeV peaks observed in the present work, Hasselgren reported excitation of levels at 5.5 MeV (which would not have been resolved in the present experiment) and 9.6 MeV.

Newton et al (Ne62) compared the relative strength of excitation of the 0.48 MeV ($\frac{1}{2}^-$) level from their work with that of the 4.63 MeV ($\frac{7}{2}^-$) level using the data of Tyrén and Maris (Ty58) and concluded that these levels together with the ground ($\frac{3}{2}^-$) and 7.47 MeV ($\frac{5}{2}^-$) states were members of a K = $\frac{1}{2}$ rotational band in a deformed ^{7}Li nucleus, based on the 0.48 MeV ($\frac{1}{2}^-$) state. Jacmart et al (Ja64) in analysing their data for inelastic scattering from ^{7}Li, claimed that their results were also consistent with a rotational model for ^{7}Li. However, in keeping with later theoretical predictions (Cl62, Ch63) they replaced the original $\frac{5}{2}^-$ member of the band (i.e. 7.47 MeV level) with the 6.56 MeV ($\frac{5}{2}^-$) level. They report maximum cross-sections of 1.8, 0.8, and 4.7 mb/ster. for the excitation of the $\frac{1}{2}^-$, $\frac{5}{2}^-$, and $\frac{7}{2}^-$, states respectively. (The three angular distributions had the same shape and were broadly peaked at about 20°). This ratio corresponds very well with the ratio predicted by the squares of the Clebsch-Gordon coefficients ($\frac{1}{5}$, $\frac{3}{35}$, $\frac{18}{35}$,). In the present experiment the maximum cross-sections (lab) for excitation of the 6.56 MeV and 4.63 MeV levels were about 3.7 and 13.3 mb/ster. respectively. This gives a relative strength of excitation which differs from that predicted by the rotational model. However, this can probably be explained by the fact that the cross-section for the 6.56 MeV level was overestimated due to a contribution of unknown strength from the continuum. The cross-section for excitation of the 7.5 MeV level was found to be considerably lower than that of the 6.56 MeV level. The results obtained by Hasselgren et al (Ha65) at 185 MeV were similar to those reported here.

Chesterfield and Spicer (Ch63) analysing the properties of ^{7}Li on the basis of a strong coupling rotational model, suggest a prolate distortion of the ^{7}Li nucleus corresponding to $\epsilon = 0.5$ and $\eta = 6.6$. They also compare the predictions of this model with those of the intermediate coupling shell model (Ku56, Me56) and observe the failure of the latter to predict a $\frac{3}{2}^{-}$ state at about 5.5 MeV. The existence of this state is necessary in the level scheme for the rotational model, being the base state for the first excited rotational band. Hasselgren et al observed the weak excitation of a level at 5.5 MeV, but were unable to extract any detailed information on its behaviour.

Later calculations on the 0.48 MeV level using shell model wave functions (Mh66) predicted a strong spin-flip component in the scattering for angles below 20° and this discrepancy with the rotational model results was checked by Johansson (Jo67) by including in his calculations configuration mixing resulting from a quadrupole nuclear deformation. Finding fairly good agreement with the data, Johansson concluded that spin-flip scattering was important in inelastic scattering at small angles contradicting the predictions of the rotational model without spin-flip.

Finally, it is interesting to note that ^{7}Li can also be well-described by a cluster model (α + t), the low-lying negative parity states resulting from the relative motion of the triton and alpha clusters (Sh60).

TABLE 5

DIFFERENTIAL CROSS-SECTIONS FOR THE ELASTIC SCATTERING OF PROTONS ON ^{7}Li.

Lab Angle degrees	$\frac{d\sigma}{d\Omega}$ lab mb / ster.	c.m. Angle degrees	$\frac{d\sigma}{d\Omega}$ cm. mb / ster.
4.5	283 ± 3	5.2	212 ± 2
5.5	261 ± 3	6.4	196 ± 2
6.5	288 ± 3	7.5	216 ± 2
7.9	326 ± 4	9.1	244 ± 3
10.4	286 ± 3	12.0	215 ± 2
13.0	247 ± 3	15.0	186 ± 2
15.6	171 ± 1	18.0	130 ± 1
20.6	79.0 ± .6	23.8	60.3 ± .4
25.6	28.3 ± .2	29.5	21.9 ± .2
30.6	9.63 ± .06	35.2	7.54 ± .05
35.6	3.86 ± .03	40.8	3.07 ± .02
40.6	2.19 ± .02	46.4	1.78 ± .01
45.4	1.34 ± .01	51.8	1.10 ± .01
50.6	.838 ± .008	57.5	.707 ± .006
60.4	.290 ± .003	68.2	.256 ± .003
75.0	.0454 ± .0013	83.7	.0434 ± .0007
90.6	.00413 ± .00022	99.5	.00429 ± .00023
105.6	.000970 ± .000092	114.2	.00109 ± .00010
120.6	.000489 ± .000062	128.2	.000592 ± .000075
135.1	.000830 ± .000068	141.3	.00107 ± .00009
150.1	.000922 ± .000059	154.5	.00124 ± .00008

Note: The above errors are r m s errors. There is an additional systematic uncertainty of ± 4.1%.

TABLE 6

DIFFERENTIAL CROSS-SECTIONS FOR THE EXCITATION OF THE 4.63 MeV STATE IN ^{7}Li.

Lab Angle degrees	$\frac{d\sigma}{d\Omega}$ lab mb / ster.	c.m. Angle degrees	$\frac{d\sigma}{d\Omega}$ cm. mb / ster.
5.3	4.1 ± 1.0	6.2	3.0 ± .7
6.3	4.2 ± 1.0	7.3	3.1 ± .8
7.7	4.3 ± 1.3	8.9	3.2 ± .9
10.2	7.2 ± 1.4	11.8	5.4 ± 1.1
12.8	8.0 ± 1.6	14.8	6.0 ± 1.2
15.4	13.3 ± 1.3	17.8	10.0 ± 1.0
20.4	12.0 ± .4	23.6	9.07 ± .27
25.4	9.04 ± .18	29.3	6.94 ± .14
30.4	4.84 ± .04	35.1	3.77 ± .03
35.4	2.70 ± .02	40.7	2.14 ± .02
40.4	1.52 ± .01	46.4	1.22 ± .01
45.2	.878 ± .007	51.7	.721 ± .006
50.4	.612 ± .006	57.5	.514 ± .005
60.2	.259 ± .003	68.2	.228 ± .002
75.1	.0602 ± .0008	83.9	.0575 ± .0008
90.3	.0109 ± .0004	99.4	.0113 ± .0005
105.3	.00456 ± .00028	114.1	.00514 ± .00031
120.3	.00296 ± .00018	128.2	.00361 ± .00021
134.8	.00319 ± .00013	141.2	.00412 ± .00016
149.7	.00348 ± .00014	154.3	.00471 ± .00019

Note:
a) The errors tabulated above are r m s errors.
b) The total systematic error for these measurements is ± 4.1%. An additional systematic error introduced by not correcting for the continuum is discussed in the text.

TABLE 7

DIFFERENTIAL CROSS-SECTIONS FOR THE EXCITATION OF THE 6.56 MeV STATE IN ^{7}Li.

Lab Angle degrees	$\frac{d\sigma}{d\Omega}$ lab mb / ster.	c.m. Angle degrees	$\frac{d\sigma}{d\Omega}$ cm. mb / ster.
10.1	1.7 ± .7	11.7	1.3 ± .5
12.7	2.9 ± .9	14.7	2.2 ± .6
15.3	4.2 ± .6	17.8	2.8 ± .4
20.3	3.69 ± .37	23.5	2.79 ± .28
25.3	3.02 ± .24	29.3	2.31 ± .18
30.3	1.71 ± .05	35.0	1.33 ± .04
35.3	.942 ± .019	40.7	.743 ± .015
40.3	.592 ± .012	45.3	.476 ± .010
45.1	.430 ± .013	51.7	.353 ± .010
50.3	.234 ± .007	57.4	.196 ± .006
60.1	.120 ± .004	68.1	.106 ± .003
75.0	.0354 ± .0018	83.9	.0338 ± .0017
90.2	.00959 ± .00096	99.4	.00996 ± .00100
105.2	.00365 ± .00055	114.1	.00471 ± .00070
120.1	.00132 ± .00020	128.0	.00161 ± .00024
134.6	.00186 ± .00037	141.1	.00241 ± .00048
149.5	.00274 ± .00027	154.1	.00372 ± .00037

Note: a) The errors tabulated above are r m s errors.

b) The total systematic error for these measurements is ± 4.1%. An additional systematic error introduced by not correcting for the continuum is discussed in the text.

FIGURE 18

ENERGY SPECTRA OF PROTONS SCATTERED FROM ^{7}Li.

FIGURE 18

Typical proton spectra from the $^{7}Li(p,p')^{7}Li$ reactions are shown for several lab. angles. The energy level scheme for ^{7}Li is shown with each spectrum. The error bars shown are for relative uncertainties.

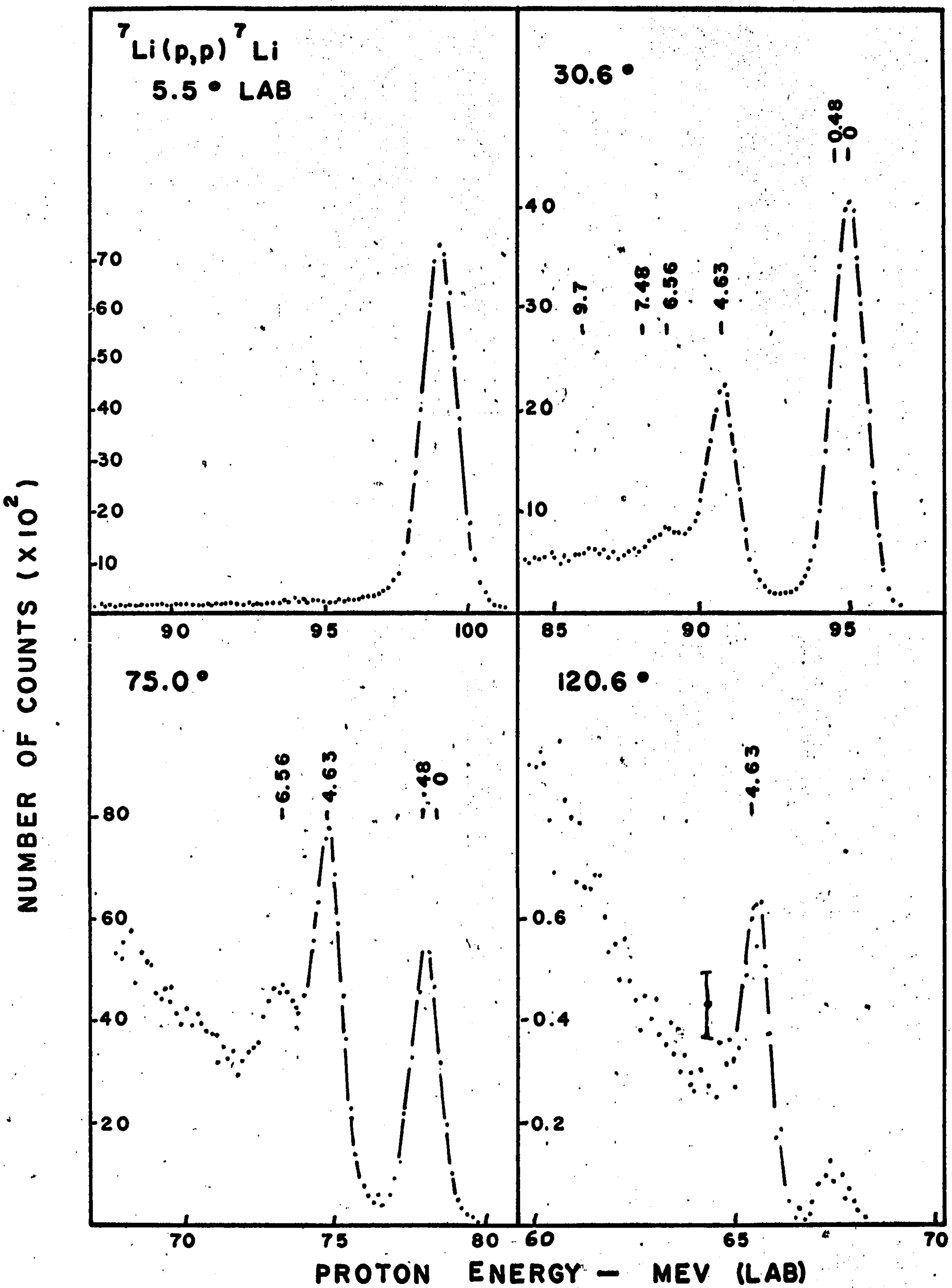

$^7Li(p,p)^7Li$
5.5° LAB
30.6°
75.0°
120.6°
0.48
0
9.7
7.48
6.56
4.63
NUMBER OF COUNTS ($\times 10^2$)
PROTON ENERGY — MEV (LAB)

FIGURE 19

ANGULAR DISTRIBUTIONS FOR ELASTIC AND IN-
ELASTIC PROTON GROUPS SCATTERED FROM ^{7}Li.

FIGURE 19

Angular distributions for the elastic scattering from ^{7}Li and for the excitation of the 4.63 MeV and 6.54 MeV states. The coordinates are in the centre-of-mass system. The error bars shown are for relative uncertainties.

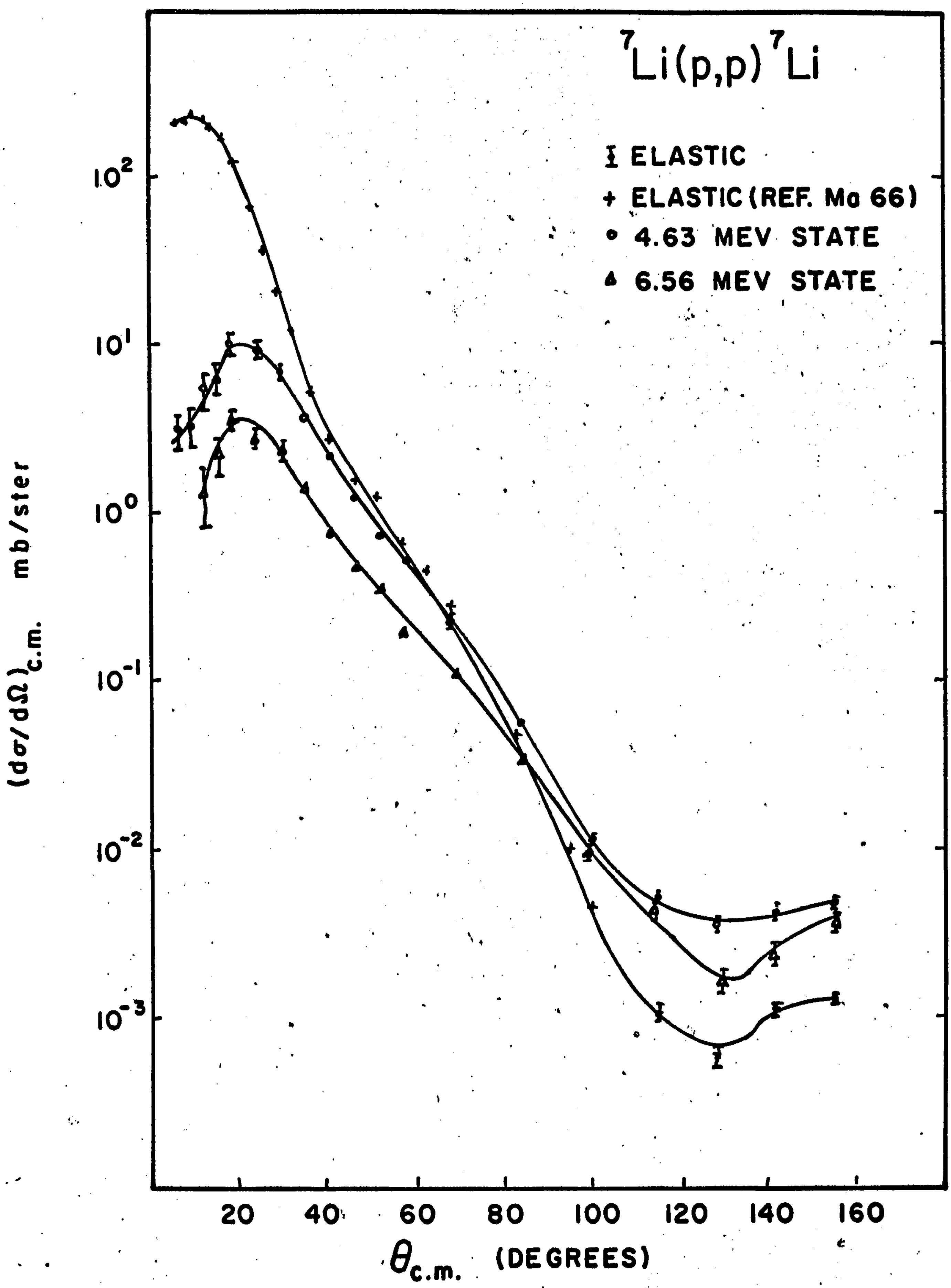

$^7Li(p,p)^7Li$
ELASTIC
ELASTIC (REF. Mo 66)
4.63 MEV STATE
6.56 MEV STATE
10^2
10^1
10^0
10^{-1}
10^{-2}
10^{-3}
$(d\sigma/d\Omega)_{c.m.}$ mb/ster
20
40
60
80
100
120
140
160
$\theta_{c.m.}$ (DEGREES)

5.3. The $^{7}Li(p,t)^{5}Li$ Reaction:

a) Experimental Results:

Data for the $^{7}Li(p,t)^{5}Li$ reaction was collected over the angular range 5^{o} to 75^{o} Lab.. Typical energy spectra for tritons from this reaction are shown in figs. 20 and 21 for angles of 5.3^{o} lab. and 15.3^{o} lab. respectively. The spectrum shown in fig. 21 for 15.3^{o} lab. is a composite spectrum derived from two spectra obtained with different magnet settings, so as to extend the observed triton energy range. However, the smaller energy "bite" of a single magnet setting was generally found to be sufficient. The ^{5}Li ground state was broad and asymmetric, being unbound (by 1.965 MeV) to (^{4}He + p) decay. A very broad $\frac{1}{2}^{-}$ level (Γ = 3 to 5 MeV) has been reported at an excitation energy between 5 and 10 MeV (La66) and this state probably contributes to the asymmetric tail observed in the ^{5}Li ground state peak. Other features of the triton spectra were the large continuum due to three body break-up (there being no particle-stable states in ^{5}Li) and the absence of any evidence of the $J^{\pi} = \frac{3}{2}^{+}$ level at 16.65 MeV or the 20 MeV ($\frac{3}{2}^{+}$, $\frac{5}{2}^{+}$) level.

The area of the ^{5}Li ground state peak was determined by fitting a gaussian curve to the high energy side of the triton peak, after making appropriate corrections for deuteron feed-through. This method for estimating the areas, although fairly accurate in the forward angles where the ground state peak was prominent, may have introduced substantial systematic errors at large angles. The typical width of the ground state peak was 2.7 MeV. The intrinsic detector resolution for tritons was estimated to be approximately 2%, by folding together the contributions from the beam energy spread, target thickness, kinematic broadening, straggling due to the material between the target and the detector, and the inherent width of the ^{5}Li ground state.

The calculated differential cross-sections for the $^{7}Li(p,t)^{5}Li$ reaction leading to the ^{5}Li ground state are tabulated together with the total experimental r.m.s. errors in Table 8. The angular distribution in the centre-of-mass system for the ground state transition is shown in fig. 22.

b) Discussion:

The $^{7}Li(p,t)^{5}Li$ reaction has been investigated at proton energies of 44 MeV (Ce66) and 155 MeV (Ba66) and also reported at energies lower than 20 MeV (Ma57, Ko59). A preliminary report of this work has been given elsewhere (Po67).

In the simple L-S coupling shell model, the selection rules for the $^{7}Li(p,t)^{5}Li$ ground state transition ($^{2}P_{3/2} \longrightarrow {}^{2}P_{3/2}$) allow values of L = 0 or 2 for the angular momentum transfer. This assumes two neutron pick-up from the 1p shell for which S=0 for the transferred neutron pair. However transitions to the 16.65 MeV state in ^{5}Li via the (p,t) reaction on ^{7}Li would require L=1, S=1, for the transferred neutron pair and this transition is therefore S- forbidden. There was no evidence for the excitation of this level in agreement with previous observations by Cerny et al (Ce66) and Bachelier et al (Ba66) and this would seem to confirm the prediction of the L-S coupling shell model.

On the other hand both ^{7}Li and ^{5}Li are known (Sh60) to have properties which can be described by a simple cluster model, the ^{7}Li ground state having a ($t + \alpha$) cluster structure with the triton and alpha particle coupled with orbital angular momentum $\ell = 1$ giving rise to a spin parity of $\frac{3}{2}^-$. Similarly the ^{5}Li ground state can be described by an alpha coupled to a proton with $\ell = 1$ giving $J^\pi = \frac{3}{2}^-$. The other possible spin parity for this configuration is $\frac{1}{2}^-$ corresponding to the broad first excited state of ^{5}Li observed in this experiment as the asymmetry in the ^{5}Li ground state low energy tail. The 16.65 MeV ($\frac{3}{2}^+$) level is slightly unbound to (d + ^{3}He) decay and can be described by a cluster model consisting of a deuteron coupled to a ^{3}He particle with $\ell = 0$. This configuration gives rise to $J^\pi = \frac{3}{2}^+$. If the ^{7}Li(p,t)^{5}Li reaction is now considered in the light of the cluster model described above, the transitions to the ground state and first excited state of ^{5}Li are the result of the pick-up of a neutron pair from the triton cluster. In this case the transferred pair will have S=0, and L=0 or 2 as in the L-S shell model description. In the case of the transition to the 16.65 MeV level, however, the transferred neutron pair must have $\ell = 1$, S = 1 and this restricts the isospin of the level to $T = \frac{1}{2}$ or $T = \frac{3}{2}$. The absence of this transition in the experimentally observed spectrum does not necessarily invalidate the cluster model description. The excitation of this level requires the pick-up of one neutron from each of the alpha and triton clusters.

Correlations of such neutron pairs are expected to be small and would consequently substantially decrease the cross-section for this transition This discussion will be considered further in a comparison with the ^{6}Li(p,d)^{5}Li reaction presented in the next section.

It should be noted that in the LS coupling shell model the transfer of a neutron pair consisting of one neutron from the p shell and one neutron from the s shell of ^{7}Li should be allowed by the selection rules, but may well be inhibited by the additional energy required and the weaker correlation between neutrons in the s and p shells.

A level at 20 MeV in ^{5}Li has been reported (To65) as a D wave d - ^{3}He interaction with spin parity tentatively assigned as $(\frac{3}{2}, \frac{5}{2})^{+}$. No evidence for this state was observed in this and previous experiments (Ce66, Ba66) and this can be explained by similar arguments as those used for the 16.65 MeV$(\frac{3}{2}^{+})$ state.

The angular distribution obtained for the ^{5}Li ground state transition is typical of the L=0 distributions observed in this energy region. A preliminary D. W. B. A. analysis of the angular distribution is presented in the next chapter.

TABLE 8

DIFFERENTIAL CROSS-SECTIONS FOR THE REACTION $^{7}Li(p,t)^{5}Li$.

Lab Angle degrees	$\frac{d\sigma}{d\Omega}$ lab μb / ster.	c.m. Angle degrees	$\frac{d\sigma}{d\Omega}$ cm μb /ster.
5.3	358 ± 13	7.0	208 ± 7
7.8	331 ± 12	9.6	193 ± 7
10.3	219 ± 8	13.5	128 ± 4
12.8	152 ± 6	16.1	89.7 ± 3.3
15.3	107 ± 4	20.0	63.6 ± 2.4
20.3	62.9 ± 2.5	26.5	38.1 ± 1.5
25.3	47.0 ± 1.8	32.9	29.2 ± 1.1
30.3	26.9 ± 1.0	39.4	17.2 ± 0.7
35.3	14.8 ± 0.6	45.7	9.80 ± 0.38
40.3	9.88 ± 0.42	52.0	6.80 ± 0.29
50.3	6.79 ± 0.31	64.2	5.10 ± 0.23
60.3	4.68 ± 0.28	76.0	3.89 ± 0.23
75.3	1.35 ± 0.09	92.8	1.33 ± 0.09

Note:

a) The errors tabulated above are the r m s errors.

b) The cross-sections are not corrected for nuclear absorption in the counter material.

c) The total systematic error for these measurements is ± 3.1%. This does not include the uncertainty due to (b) above, or the possible large systematic error in fitting the peaks.

FIGURE 20

TRITON ENERGY SPECTRUM FROM ^{7}Li AT 5.3^{o} LAB.

FIGURE 20

$^{7}Li(p,t)^{5}Li$ triton spectrum at 5.3° lab. The ^{5}Li energy level scheme and the $(p + {}^{4}He)$ threshold are shown. The error bars shown are for relative uncertainties.

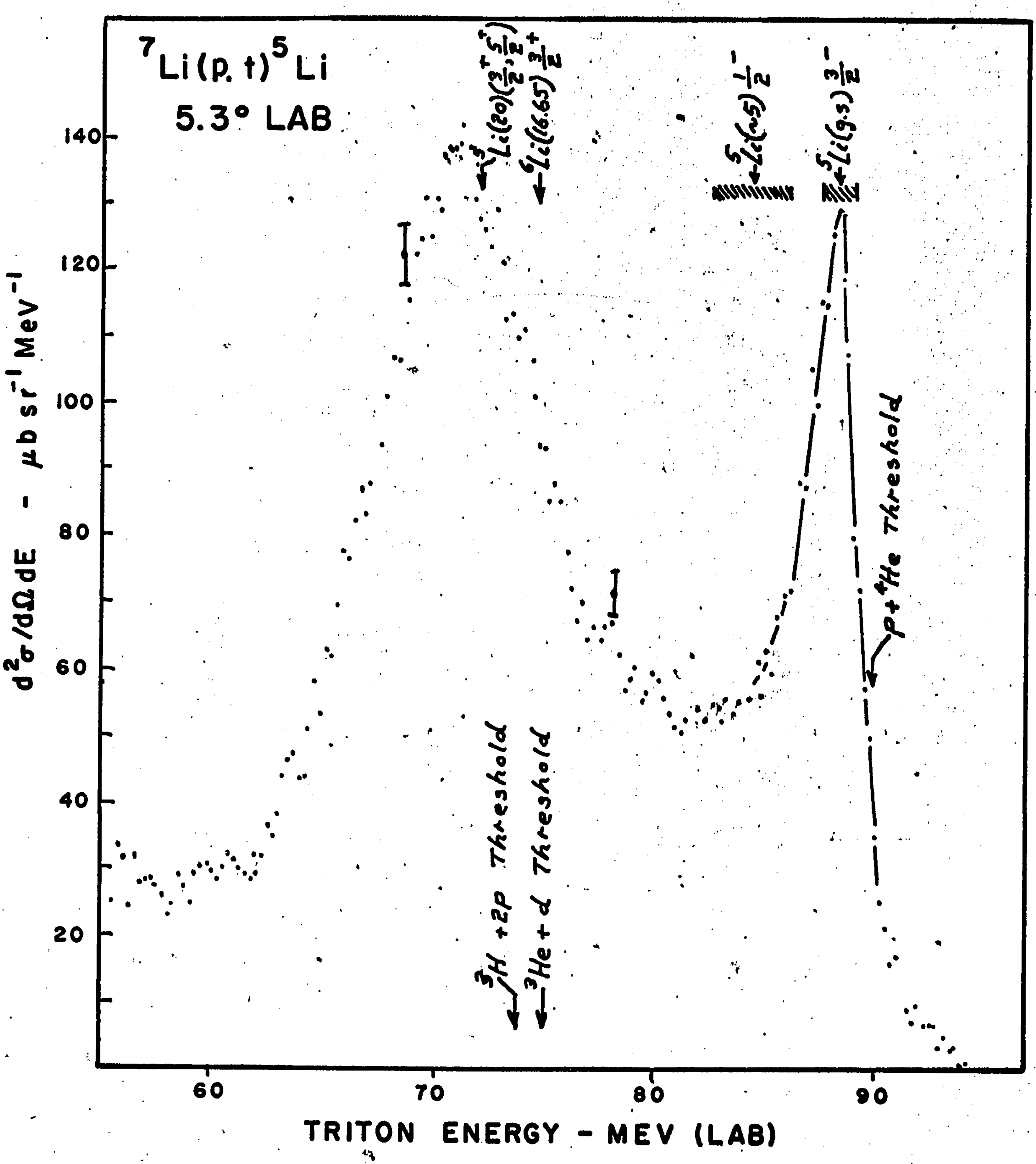

$^7Li(p,t)^5Li$
5.3° LAB
$^5Li(20)(\frac{3}{2}^+,\frac{5}{2}^+)$
$^6Li(16.65)\,\frac{3}{2}^+$
$^5Li(\sim 5)\,\frac{1}{2}^-$
$^5Li(g.s)\,\frac{3}{2}^-$
$p + {}^4He$ Threshold
$^3H + 2p$ Threshold
$^3He + d$ Threshold
$d^2\sigma/d\Omega dE$ - $\mu b\, sr^{-1}\, MeV^{-1}$
TRITON ENERGY - MEV (LAB)

FIGURE 21

TRITON ENERGY SPECTRUM FROM ^{7}Li AT 15.3° LAB.

FIGURE 21

$^{7}Li(p,t)^{5}Li$ triton spectrum at 15.3° lab. The spectrum is a composite of two spectra taken with different magnet settings and therefore extends to a higher excitation energy than the previous spectrum shown at 5.3° lab. The error bars shown are for relative uncertainties.

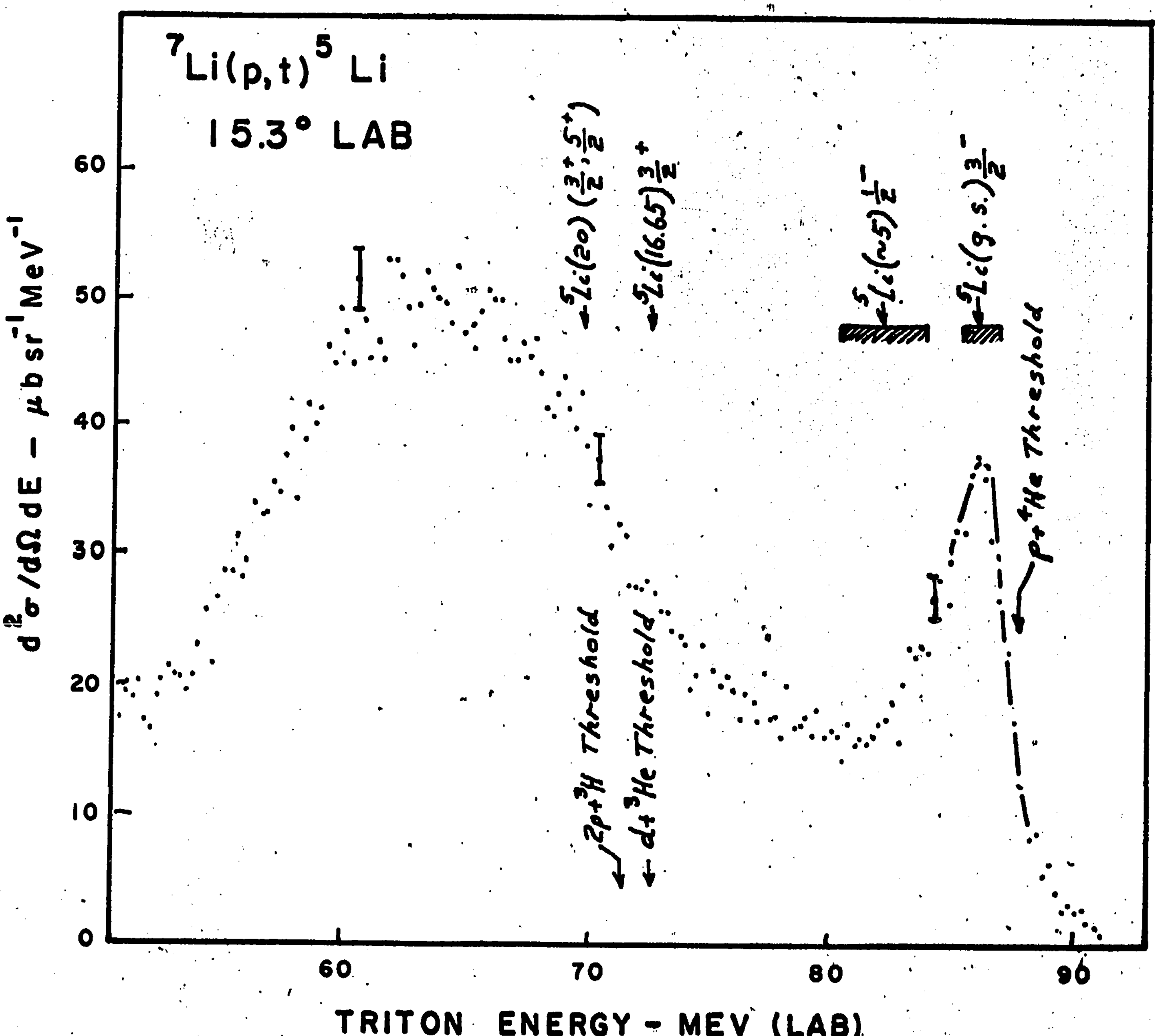

$^7Li(p,t)^5Li$
15.3° LAB
$d^2\sigma/d\Omega\, dE$ – $\mu b\, sr^{-1}\, MeV^{-1}$
TRITON ENERGY – MEV (LAB)
$^5Li(20)\ (\frac{3}{2}^+, \frac{5}{2}^+)$
$^5Li(16.65)\ \frac{3}{2}^+$
$^5Li(\sim 5)\ \frac{1}{2}^-$
$^5Li(g.s.)\ \frac{3}{2}^-$
$2p + {}^3H$ Threshold
$d + {}^3He$ Threshold
$p + {}^4He$ Threshold

FIGURE 22

ANGULAR DISTRIBUTION FOR THE $^{7}Li(p,t)^{5}Li$ REACTION

FIGURE 22

$^{7}Li(p,t)^{5}Li$ ground state angular distribution.

The coordinates are in the centre-of-mass system.

The error bars shown are for relative uncertainties.

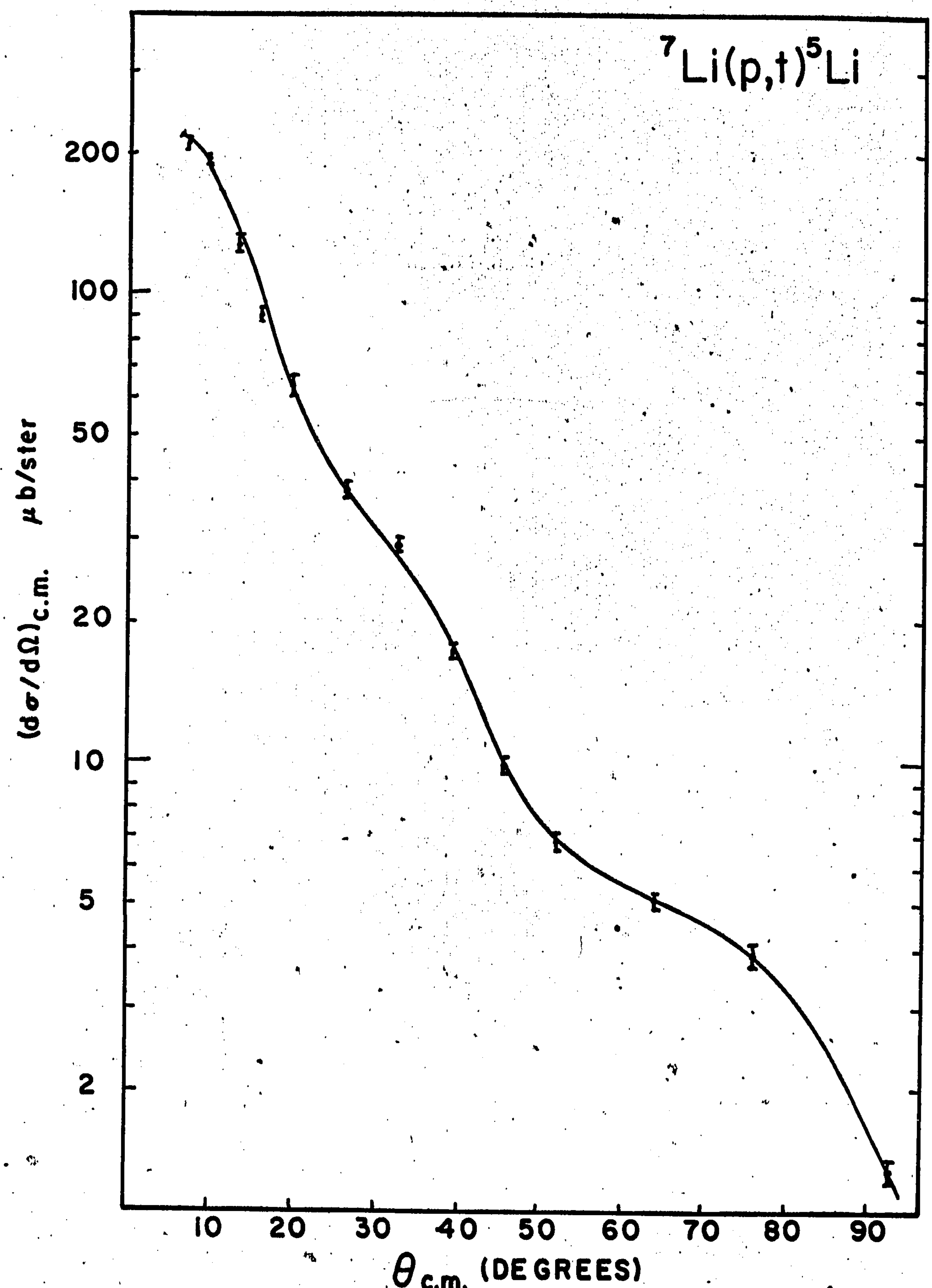

$^7Li(p,t)^5Li$
200
100
50
20
10
5
2
$(d\sigma/d\Omega)_{c.m.}$ μb/ster
10 20 30 40 50 60 70 80 90
$\theta_{c.m.}$ (DEGREES)

5.4. The $^{6}Li(p,d)^{5}Li$ Reaction

a) Experimental Results:

Data for the (p,d) reaction on ^{6}Li were collected over an angular range of 5^{o} to 90^{o} lab. Typical deuteron energy spectra from this reaction are shown in figs. 23 and 24. In order to investigate a region of excitation sufficient to include the 16.65 MeV ($\frac{3}{2}^{+}$) and 20 MeV ($\frac{3}{2}^{+}$, $\frac{5}{2}^{+}$) levels of ^{5}Li, each spectrum was determined as a composite of two spectra obtained at different magnet settings. The magnet settings were typically adjusted to give spectra overlapping by about 5 to 10 MeV and the correlation in this region was always very good. The observed deuteron spectra were similar to the triton spectra in the $^{7}Li(p,t)^{5}Li$ reaction except for the prominent deuteron peak in the forward angle region corresponding to excitation of the 16.65 MeV ($\frac{3}{2}^{+}$) level in ^{5}Li. There was no evidence for the excitation of the previously reported 20 MeV ($\frac{3}{2}$, $\frac{5}{2}$)$^{+}$ state, although it could have been obscured by the large background due to three body break-up.

The area of the ^{5}Li ground state peak and the 16.65 MeV ($\frac{3}{2}^{+}$) peak were determined in the same way as previously described for the triton spectra from ^{7}Li. The systematic error in the estimation of the area of the deuteron peaks was probably lower than that for the corresponding triton peaks due to the better deuteron energy resolution.

The differential cross-sections for the $^{6}Li(p,d)^{5}Li$ reaction leading to the ^{5}Li ground state are tabulated together with the associated relative (r m s) errors in Table 9 for both laboratory and centre-of-mass coordinate systems. The differential cross-sections for the 16.65 MeV state could only be determined for angles smaller than 15^{o}, the deuteron peak being indistinguishable from the three body break-up continuum at larger angles. The angular distributions for the ^{5}Li ground state and 16.65 MeV state deuterons are given in fig. 25 in the centre-of-mass coordinate system.

b) Discussion:

The ^{6}Li(p,d)^{5}Li reaction has been investigated at proton energies of 19 MeV (Li55), 37 MeV (Ku67) and 156 MeV (Ba66). From the conservation of isotopic spin, the (p,d) reaction on ^{6}Li should excite $T = \frac{1}{2}$ levels in ^{5}Li. The observation that the 16.65 MeV level is strongly excited in this reaction confirms that it is a $T = \frac{1}{2}$ level. In the LS coupling shell model the excitation of the ^{5}Li ($\frac{3}{2}^{-}$) ground state and the $\frac{1}{2}^{-}$ state result from the pick-up of a p shell neutron, and the 16.65 MeV ($\frac{3}{2}^{+}$) state results from the pick-up of an s shell neutron. The ground state and the 16.65 MeV state angular distributions should therefore be characteristic of $\ell_n = 1$ and $\ell_n = 0$ pick-up. Inspection of the angular distributions of fig. 25 seems to verify this. The ^{6}Li(p,d)^{5}Li reaction can also be described within the framework of the cluster model, ^{6}Li being represented by an alpha-deuteron cluster structure with the two clusters coupled with orbital angular momentum L=0. In this model, excitation of the ^{5}Li ground and first excited states results from the pick-up of a neutron from the loosely bound deuteron cluster. The excitation of the 16.65

MeV level corresponds to the pick-up of a neutron from the tightly bound alpha particle. In fact the difference in excitation energy of these levels reflects the known difference in binding energies of a 1 p proton and 1 s proton in ^{6}Li (about 17 MeV) obtained from the ^{6}Li(p,2p)^{5}He reaction (Ti62).

Inspection of the small angle data (see 5^{o} spectrum) indicates that the excitation strength of the 16.65 MeV level at very small angles is of the order of twice that of the ground state transition. This is what might be expected on the basis of a simple impulse approximation, since there are twice as many s shell as p shell neutrons. This observation implies that the energy effect does not inhibit the pick up of neutrons from the s shell. Returning now to the L-S coupling shell model description of the (p,t) reaction on ^{7}Li in which the transferred neutron pair consists of an s and p shell neutron; the fact that pick-up of s shell neutrons is probably as strong as pick-up in the p shell should tend to enhance the cross-section for this process (statistically by a factor of four) in spite of the poorer correlation between s and p neutrons. This may in fact imply that the transition should be observable, in contrast to the previously established s-forbidden nature of the two neutron pick-up from the p shell. In the cluster model description of the (p,t) reaction on ^{7}Li (as previously described) the reaction would be inhibited by the poor correlation of two neutrons in the widely separated ^{7}Li alpha and triton clusters and the experimental observations therefore may tend to favor the cluster model structure over the L-S shell model description.

TABLE 9

DIFFERENTIAL CROSS-SECTIONS FOR THE REACTION $^{6}Li(p,d)^{5}Li$.

Lab Angle degrees	$\frac{d\sigma}{d\Omega}$ lab μb / ster.	c.m. Angle degrees	$\frac{d\sigma}{d\Omega}$ cm μb / ster.
5.3	5530 ± 100	6.8	3390 ± 60
10.3	3060 ± 60	13.2	1890 ± 30
15.3	1420 ± 30	19.5	889 ± 17
20.4	771 ± 19	26.0	491 ± 12
25.3	480 ± 14	32.1	312 ± 9
30.3	282 ± 9	38.4	188 ± 6
35.4	130 ± 4	44.7	89.4 ± 2.8
40.3	81.3 ± 2.8	50.7	57.8 ± 2.0
50.3	35.5 ± 1.2	62.6	27.2 ± 0.9
60.3	17.7 ± 0.9	74.2	14.8 ± 0.7
75.3	8.58 ± 0.39	90.8	8.40 ± 0.38
90.3	3.59 ± 0.23	106.3	4.04 ± 0.25

Note: a) The errors tabulated above are the r m s errors.

b) The total systematic error for these measurements is ± 5.5%. This does not include a possible systematic error in the method used for fitting the peaks.

FIGURE 23

DEUTERON ENERGY SPECTRUM FROM ^{6}Li AT 5.3^{o} LAB.

FIGURE 23

$^{6}Li(p,d)^{5}Li$ deuteron spectrum at 5.3^{o} lab. The ^{5}Li energy level scheme and the $(p + {}^{4}He)$ threshold are shown. The error bars shown are for relative uncertainties.

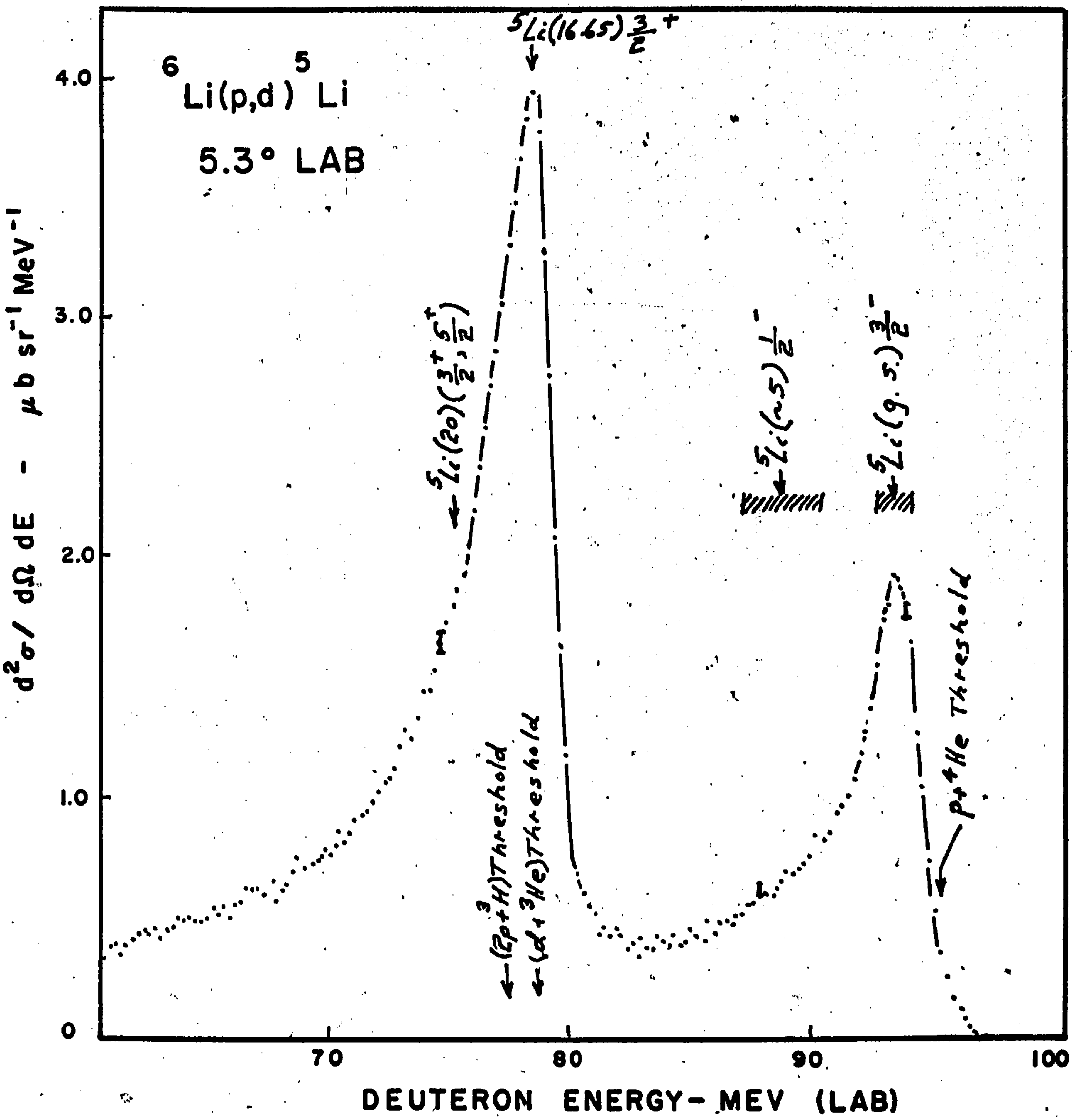

6Li(p,d)5Li
5.3° LAB
5Li(16.65) 3/2+
5Li(20)(3/2+,5/2+)
5Li(~5) 1/2-
5Li(g.s.) 3/2-
(2p+3H)Threshold
(d+3He)Threshold
p+4He Threshold
4.0
3.0
2.0
1.0
0
70
80
90
100
d2σ/ dΩ dE - μb sr-1 MeV-1
DEUTERON ENERGY- MEV (LAB)

FIGURE 24

DEUTERON ENERGY SPECTRA FROM ^{6}Li

FIGURE 24

$^{6}Li(p,d)^{5}Li$ deuteron spectra for several indicated lab angles. The error bars shown are for relative uncertainties.

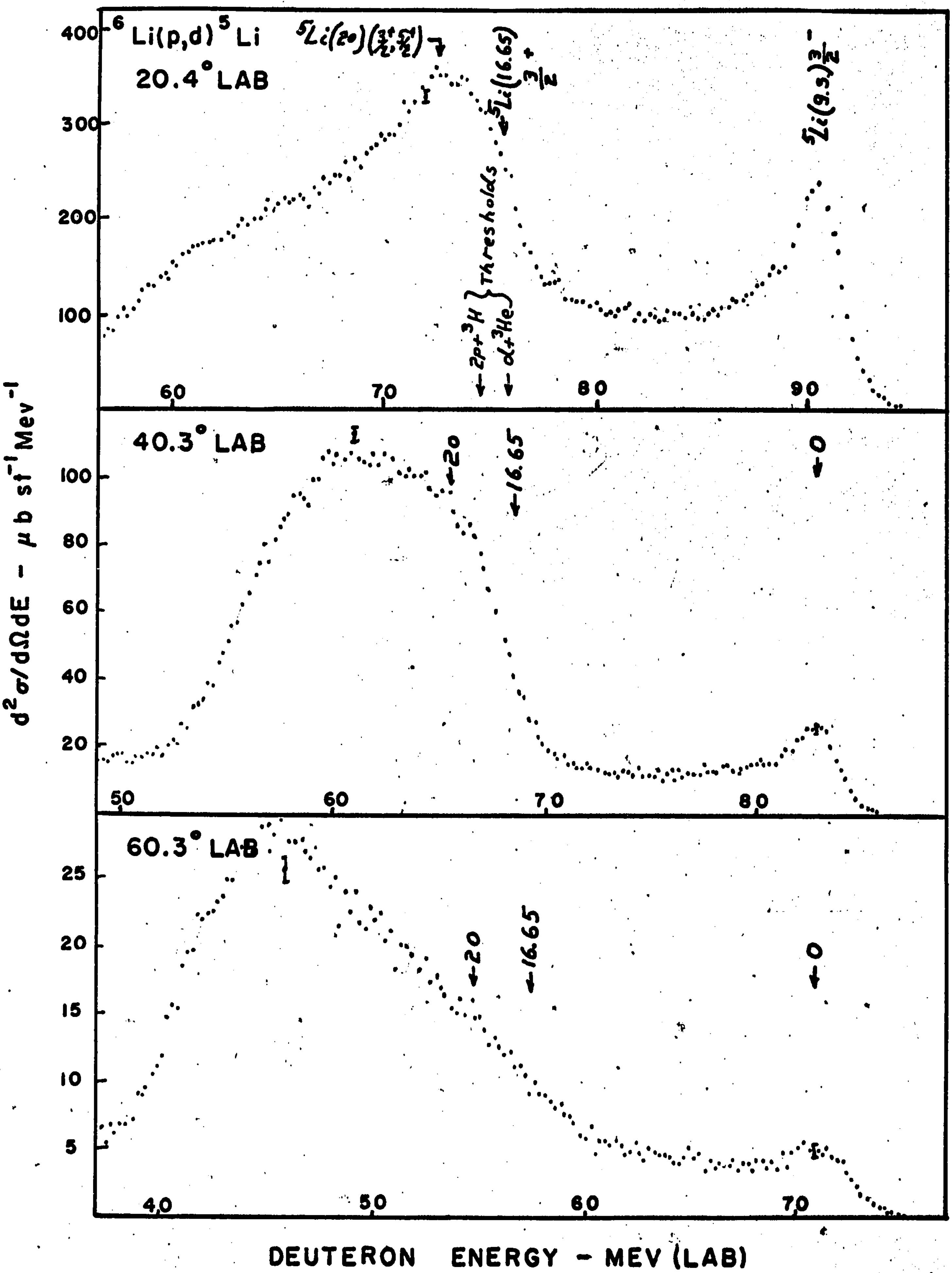

^{6}Li(p,d)^{5}Li
20.4° LAB
^{5}Li(20)($\frac{3}{2}^+$,$\frac{5}{2}^+$)
^{5}Li(16.65) $\frac{3}{2}^+$
^{5}Li(9.5)$\frac{3}{2}^-$
2p+^{3}H
α+^{3}He
Thresholds
40.3° LAB
20
16.65
0
60.3° LAB
20
16.65
0
d$^2\sigma$/dΩdE - μb st^{-1} Mev^{-1}
DEUTERON ENERGY - MEV (LAB)

FIGURE 25

ANGULAR DISTRIBUTION FOR THE $^{6}Li(p,d)^{5}Li$ REACTION

FIGURE 25

$^{6}Li(p,d)^{5}Li$ ground state angular distribution.

The coordinates are in the centre-of-mass system.

The error bars shown are for relative

uncertainties.

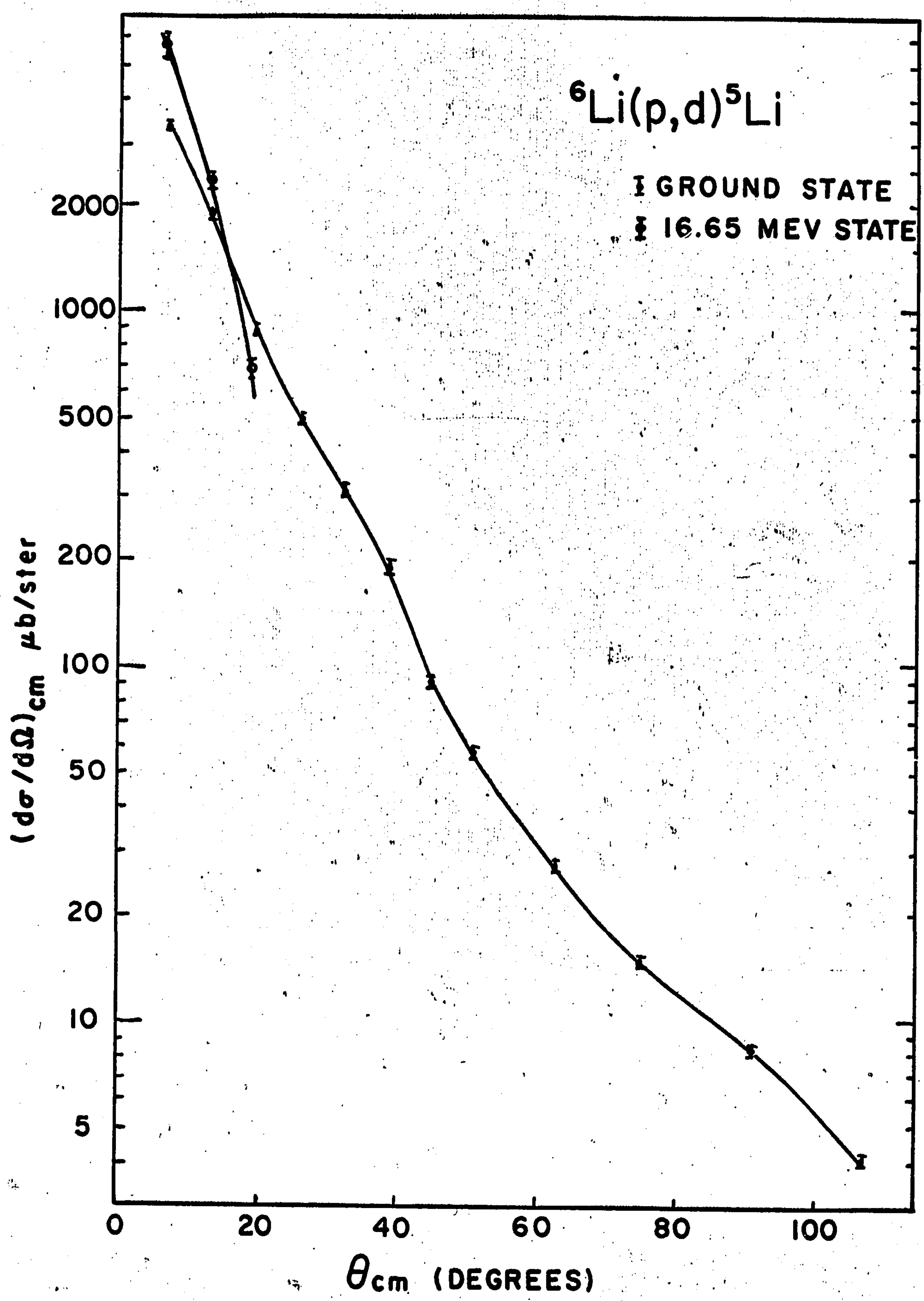

$^6Li(p,d)^5Li$
GROUND STATE
16.65 MEV STATE
2000
1000
500
200
100
50
20
10
5
$(d\sigma/d\Omega)_{cm}$ μb/ster
0
20
40
60
80
100
θ_{cm} (DEGREES)

5.5 The $^6Li(p,t)^4Li$ Reaction:

a) Experimental Results:

Data for the (p,t) reaction on ^6Li was collected over an angular range from 5 to 50 degrees in the lab. system. A typical triton energy spectrum obtained at 5.3^o lab. is shown in fig. 26. The main features are the broad peak at the high energy end of the spectrum and the large continuum due to three body break-up. The thresholds for various three body break-up processes are indicated in the figure. The high energy peak is denoted here as the "ground state" of ^4Li, by analogy with the observations in the $^7Li(p,t)^5Li$ reaction although, as will be discussed later; it may well be due to contributions from several states. Estimation of the area of the ground state peak was complicated by the large continuum and separation of the peak was, especially at large angles, subject to quite considerable systematic errors. The method used to determine the peak area was to fit a gaussian curve to the high energy side of the peak, after making the necessary corrections to the spectrum for deuteron feed-through. No attempt was made to estimate a background level due to the continuum, and the resulting uncertainties in the peak area could conceivably be as great as + 50%. The differential cross-sections for the (p,t) reaction on ^6Li leading to the ^4Li "ground state" are tabulated together with the associated relative uncertainties in Table 10 for both the laboratory and centre-of-mass coordinate systems. The angular distribution for the "ground state" transition is given in fig. 27.

b) Discussion:

The (p,t) reaction on ^{6}Li has been previously investigated by Cerny et al (Ce66a) at 44 MeV and by Bachelier et al (Ba66, Ba67) at 156 MeV. Preliminary results of this work have also appeared elsewhere (Po67). The triton spectra obtained by Cerny et al and Bachelier et al have the same general features as those observed in the present experiment.

The triton energies corresponding to the ^{4}Li "ground state" peak positions were obtained from a triton energy calibration which was determined from the analysis of the ^{7}Li(p,t)^{5}Li kinematics. This calibration was checked by conventional range (absorber) measurements. The linearity and reproducibility over the energy range from about 40 MeV to 90 MeV was very good and the errors in calibration were estimated to be less than $\pm$ 1%. Kinematic calculations of the triton energies for the ^{6}Li(p,t)^{4}Li reaction were then made, varying the ^{4}Li mass so as to fit the observed angular variation of the ^{4}Li "ground state" energy. This analysis made over the entire angular range covered by the data, indicated that the ^{4}Li "ground state" is unbound to (p+^{3}He) decay by 2.7 $\pm$ 0.7 MeV. This value is in good agreement with the result obtained by Cerny et al (2.9 $\pm$ .3 MeV). Preliminary analysis of the Orsay results (Ba66) gave a somewhat larger value, but with a corresponding larger uncertainty.

The intrinsic width of the unbound ^{4}Li ground state was determined from the peak width and a knowledge of the experimental resolution which was obtained from a previous study of the $^{7}Li(p,t)^{5}Li$ reaction. The width obtained from the data was 4.8 $\pm$ 0.5 MeV which again is in good agreement with the 5.0 $\pm$ 0.5 MeV value quoted by Cerny et al.

On the basis of their results for the ^{4}Li "ground state" and using Coulomb calculations, Cerny et al predicted that the lowest T = 1 state in the ^{4}He would be at 22.5 $\pm$ .3 MeV, and that the analog ^{4}H nucleus would also be unbound by about 2 MeV. They then found an indication of this analog state in ^{4}He in a study of the $^{6}Li(p,{}^{3}He)^{4}He^{*}$ reaction and compared its angular distribution with that of the ^{4}Li ground state from the $^{6}Li(p,t)^{4}Li$ reaction. Agreement was found both in shape and in relative cross-sections (after making the necessary corrections for isospin coupling and phase space) and it was concluded that (within their large uncertainties of peak separation and background correction) this confirmed the assignment of the ^{4}Li and ^{4}He analog states. They also stated that the angular distributions were consistent with the L = 1 angular momentum transfer which would be expected for transitions to 1^{-} or 2^{-} states.

Tombrello (To65b) made a comprehensive phase-shift analysis of all the available data on p + ^{3}He scattering and polarization measurements and concluded that there was strong evidence for at least 3 p wave levels in ^{4}Li (unbound to p+^{3}He). He found possible triplet states with $J^{\pi} = 2^{-}, 1^{-}, 0^{-}$, at centre-of-mass energies of 4.74, 6.15, and 9.74 MeV above the (p+^{3}He) threshold and also, but with less confidence a broad singlet 1^- level at 9.8 MeV. He also stated that these resonances have the ordering that would be expected on the basis of a simple L-S coupling shell model and that the spacing and widths (which with the exception of the singlet level were comparable with the Wigner limit) are consistent with those of ^{5}Li.

Most experimental searches for ^{4}Li have been inconclusive or unsuccessful. The existence of a particle stable state is most unlikely (Im64) and searches for unbound states in ^{4}Li have been mainly inconclusive or negative. A summary of some of the experimental work done on ^{4}Li is given in an article by Kerr (Ke66), who also finds no evidence for states in ^{4}Li. However Kerr states that a level with the width and low cross-section reported by Cerny et al (and discussed above), would probably not have been detected in his experiment.

To summarize, although the evidence in this experiment (and Cerny's) is not conclusive, it seems probable that the unbound "ground state" of ^{4}Li has been observed, but because of its width, the peak denoted by the ^{4}Li ground state may conceivably be due to more than one state.

A preliminary D.W.B.A. analysis of the angular distribution is presented in the following chapter.

TABLE 10

DIFFERENTIAL CROSS-SECTIONS FOR THE REACTION $^{6}Li(p,t)^{4}Li$

Lab Angle degrees	$\frac{d\sigma}{d\Omega}$ lab μb / ster.	c.m. Angle degrees	$\frac{d\sigma}{d\Omega}$ cm μb / ster.
5.3	518 ± 19	7.6	260 ± 9
7.8	364 ± 13	11.0	184 ± 7
10.3	267 ± 10	14.6	136 ± 5
12.8	174 ± 7	18.1	89.2 ± 3.5
15.3	96.6 ± 3.8	21.6	50.0 ± 2.0
20.3	71.7 ± 3.3	28.6	38.2 ± 1.7
25.3	46.6 ± 2.0	35.6	25.6 ± 1.1
30.3	36.0 ± 1.7	42.4	20.6 ± 1.0
35.3	18.7 ± 0.8	49.2	11.2 ± 0.5
40.3	14.3 ± 0.6	55.9	9.06 ± 0.38
50.3	10.8 ± 0.4	69.0	7.74 ± 0.29

Note:

a) The errors tabulated above are the r m s errors.

b) The cross-sections are not corrected for nuclear absorption in the counter material.

c) The total systematic error for these measurements is ± 3.5%. This does not include the uncertainty due to (b) above, or the possible large systematic error in fitting the peaks.

FIGURE 26

TRITON ENERGY SPECTRUM FROM ^{6}Li

FIGURE 26

$^{6}Li(p,t)^{4}Li$ triton spectrum at 5.3^{o}Lab. The $p+^{3}He$ threshold and the excitation energy in the ^{4}Li c.m. system are shown. The error bars are for relative uncertainties.

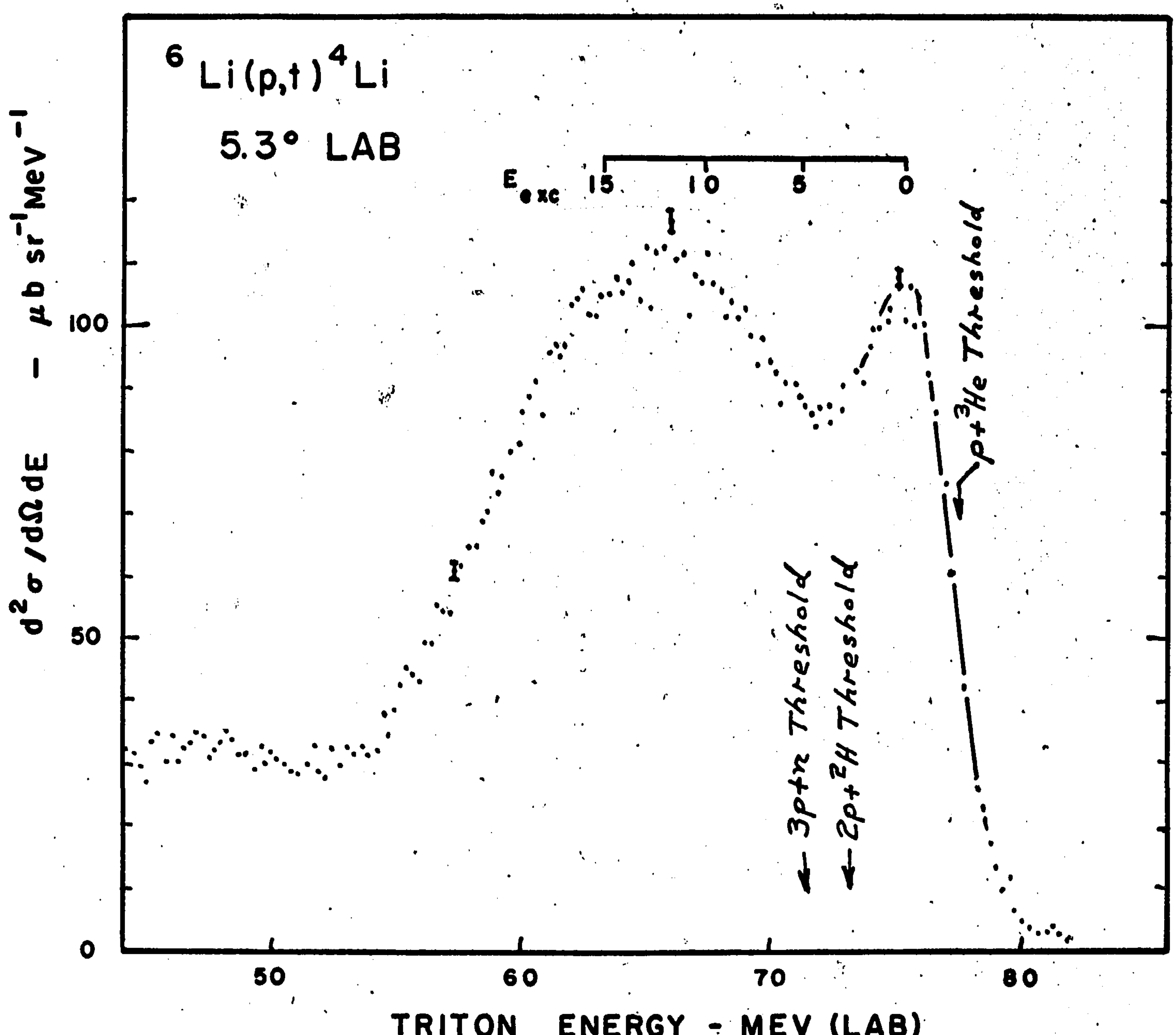

$^6Li(p,t)^4Li$
5.3° LAB
E_{exc} 15 10 5 0
$d^2\sigma/d\Omega dE$ - $\mu b\ sr^{-1} MeV^{-1}$
100
50
0
50
60
70
80
TRITON ENERGY - MEV (LAB)
$p+{}^3He$ Threshold
$3p+n$ Threshold
$2p+{}^2H$ Threshold

FIGURE 27

ANGULAR DISTRIBUTION FOR THE $^{6}Li(p,t)^{4}Li$ REACTION

FIGURE 27

$^6Li(p,t)^4Li$ "ground state" angular distribution.

The coordinates are in the centre-of-mass system.

The error bars shown are for relative uncertainties.

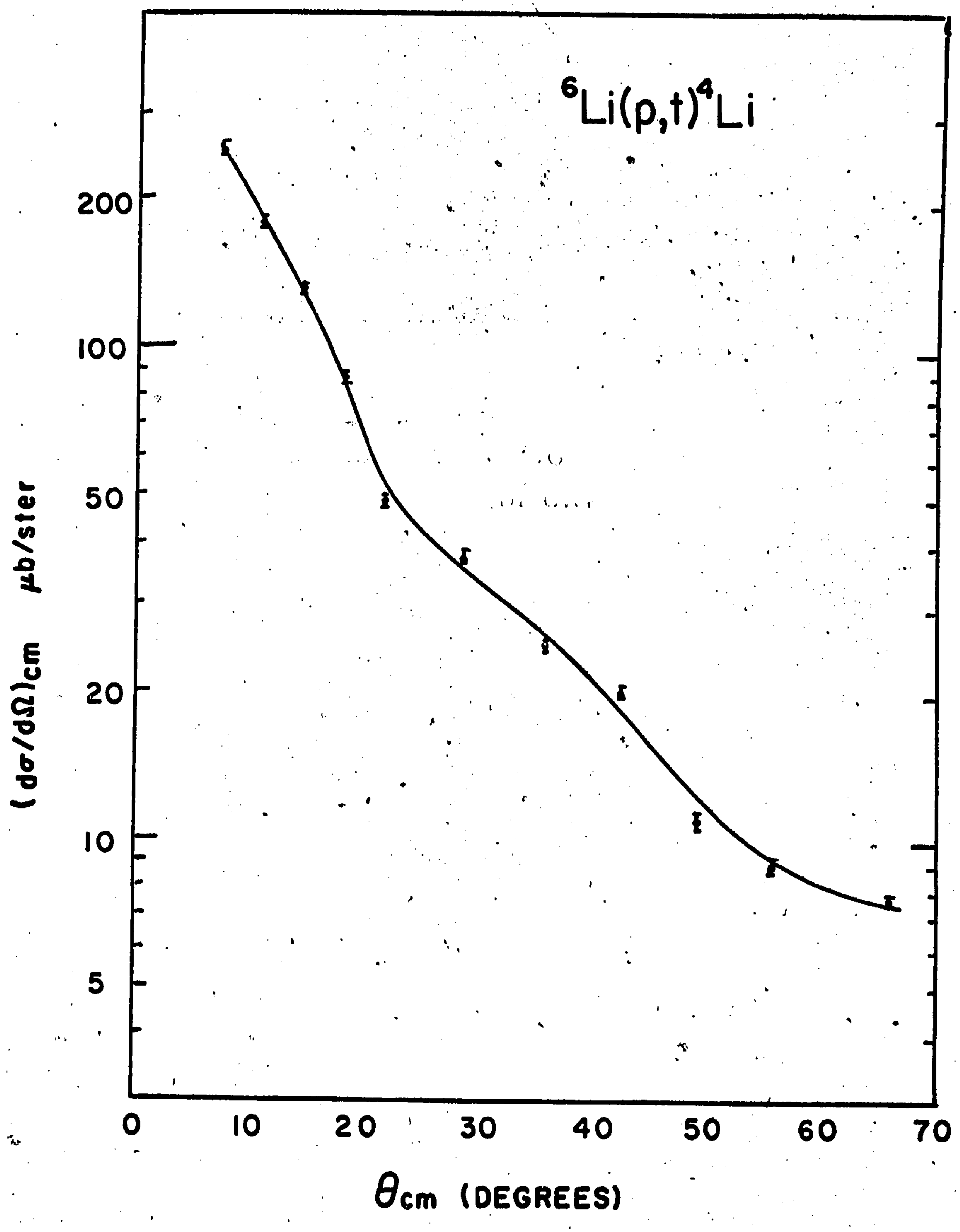

$^6Li(p,t)^4Li$
200
100
50
20
10
5
$(d\sigma/d\Omega)_{cm}$ μb/ster
0
10
20
30
40
50
60
70
θ_{cm} (DEGREES)

5.6. The $^4He(p,p')^4He^*$ and $^4He(p,d)^3He^*$ Reactions:

In an experiment recently completed, Goldstein (Go67) studied elastic and inelastic scattering and the deuteron pick-up reaction on ^4He. This section describes a continued study of these reactions with the improved resolution and particle separation afforded by the present experimental set-up. In particular a search was made for excited states in ^4He and ^3He through the investigation of the $^4He(p,p')^4He^*$ and $^4He(p,d)^3He^*$ reactions.

Inelastic scattering from ^4He was studied at several angles with good statistics and a typical spectrum obtained is shown in fig.28 for an angle of 45° lab. This spectrum is a composite of two spectra obtained with different magnet settings, the elastic and inelastic data being collected separately because of the high excitation energy of the inelastic levels and the finite energy "bite" of the magnet analyser system. The spectrum has been corrected for background originating from the helium target container. This was accomplished by subtracting from the spectrum, a background spectrum obtained with the target empty. The main features of this spectrum are similar to those observed by Goldstein and other previous proton scattering experiments on ^4He. The energy resolution obtained for the elastic peak was typically 1.4 MeV. The calculated differential cross-section for elastic scattering at 45.5° was 2.87 ± 0.03 mb/ster. which is in good agreement with the value of 2.95 ± 0.09 mb/ster. obtained at this angle by Goldstein. The spectrum illustrates the lack of bound excited states in ^4He below the proton and neutron separation energies. The continuum due to the three body break-up modes (p + ^{3}H) and (n + ^{3}He) is readily evident from the figure and the peak at the high energy end of the continuum corresponds to the excitation of the well known 22 MeV level (Pa 65). The excitation energy of this state was determined (from a rough energy calibration) to be about 21.4 MeV. This level was observed at all scattering angles studied, however, no evidence was found for the excitation of other unbound levels.

There is considerable experimental evidence for a 0^+ resonant state in ^{4}He at an excitation energy of about 20.1 MeV (Mf65). A search for this level, which has been observed in a (high resolution) scattering experiment at 40 MeV (Wi66), was unsuccessful.

A more detailed discussion of the experimental and theoretical evidence for known unbound levels in ^{4}He has been presented by Goldstein (Go67).

b) The ^{4}He(p,d)^{3}He* Reaction:

The deuteron pick-up reaction on ^{4}He was investigated over an angular range from 5° to 70° lab and deuteron energy spectra with good statistics obtained at several angles. A typical deuteron spectrum, corrected for background and taken at 45.5° lab. is shown in fig. 29. The spectrum consists of a peak corresponding to the ground state of ^{3}He and a continuum resulting from three body break-up of the residual nucleus. There is no evidence of structure indicating the excitation of unbound states in ^3He.

Baldin (Bd66), on the basis of scattering theory, predicted a $T = \frac{1}{2}$ level in ^3He at an excitation energy of 2.5 MeV in the (p - D) centre-of-mass system. Subsequently, Kim et al (Ki66) in a study of inelastic, scattering of protons on ^3He at 30 MeV reported the excitation of levels in ^3He at 8.2, 10.2, and 12.6 MeV, the 10.2 level being the most strongly excited with an estimated cross section of 2 mb/ster. at an angle of 15^o lab. Kim et al suggest that the level observed at 8.2 MeV might be the analog state of ^3n supporting the existence of a trineutron bound by about 1 MeV.

The positions of the three levels observed by Kim et al are shown in fig. 29 and it is evident that no confirmation of their results can be made. The differential cross-section for excitation of any of these levels at this angle was less than 4 μb/ster.

A number of other experiments which also contradict the results of Kim et al have been reported and much of this work has been discussed by Goldstein (Go67) who also found no evidence for these levels in (p,p') scattering on ^3He.

FIGURE 28

ENERGY SPECTRUM OF PROTONS SCATTERED FROM ^{4}He

FIGURE 28

$^{4}He(p,p)^{4}He$ proton spectrum at 45°lab. showing, in particular, positions of expected unbound levels in ^{4}He. Background due to the target cylinder has been subtracted. The error bars shown are for relative uncertainties.

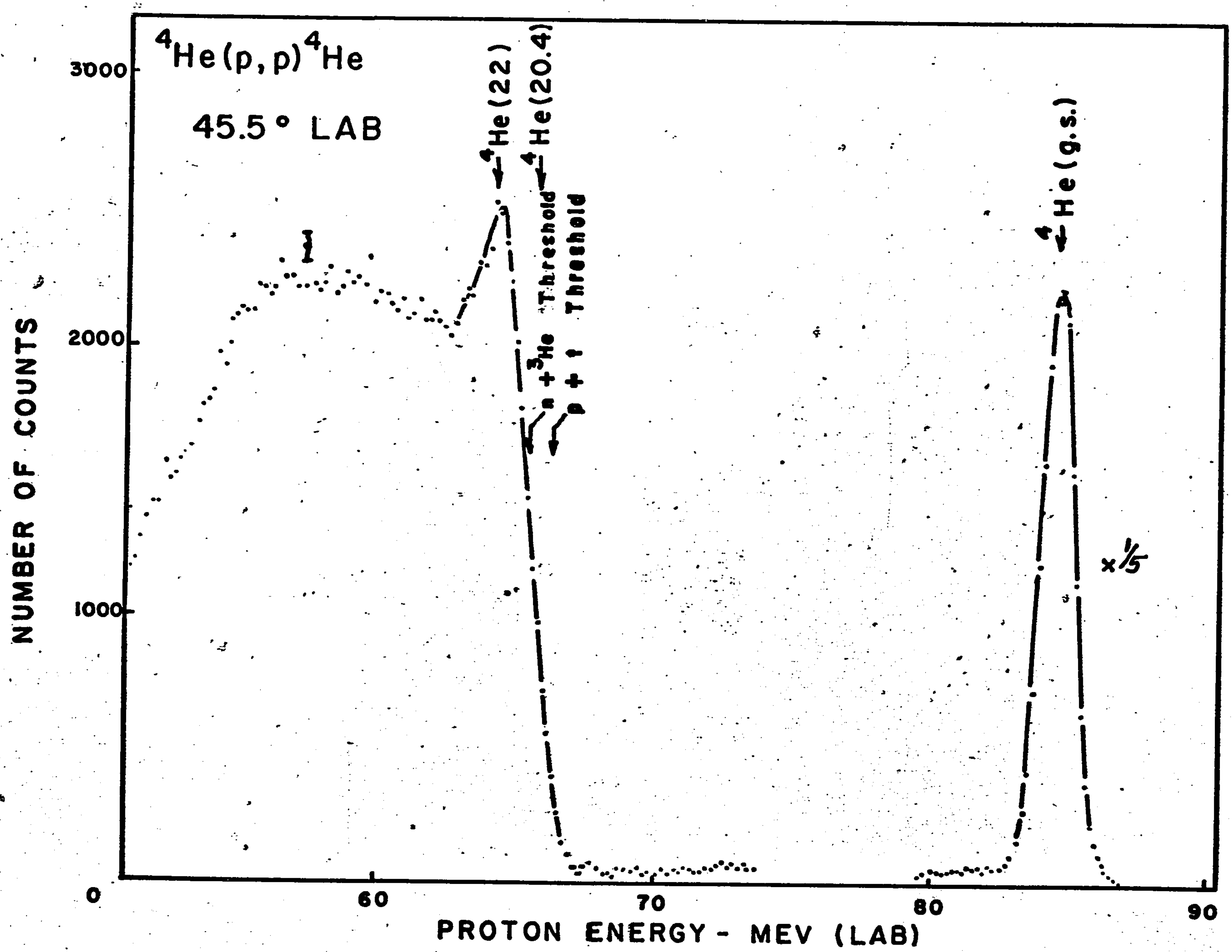
$^4He(p,p)^4He$
45.5° LAB
$^4He(22)$
$^4He(20.4)$
$n + {}^3He$ Threshold
$p + t$ Threshold
$^4He(g.s.)$
×1/5
3000
2000
1000
0
60
70
80
90
NUMBER OF COUNTS
PROTON ENERGY - MEV (LAB)

FIGURE 29

ENERGY SPECTRUM OF DEUTERONS FROM ^{4}He

FIGURE 29

$^{4}He(p,d)^{3}He$ deuteron spectrum at 45^{o} Lab. Positions of proposed ^{3}He excited states (see text) are shown. Background due to the target cylinder has been subtracted. The error bars shown are for statistical uncertainties.

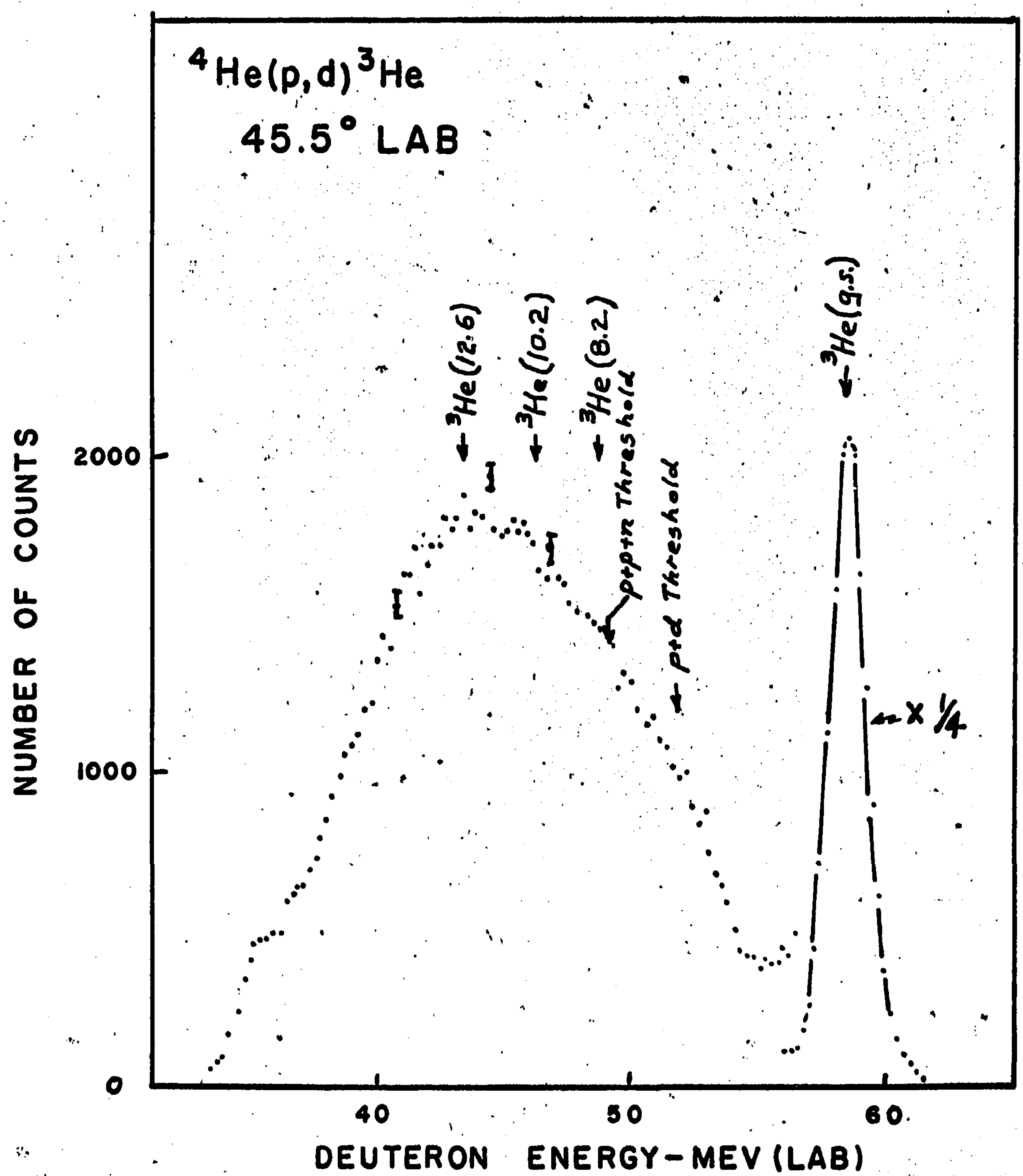

$^4He(p,d)^3He$
45.5° LAB
^3He(12.6)
^3He(10.2)
^3He(8.2)
p+p+n Threshold
p+d Threshold
^3He(g.s.)
x 1/4
2000
1000
0
40
50
60
NUMBER OF COUNTS
DEUTERON ENERGY-MEV (LAB)

5.7 The (p,t) Reaction on ^{4}He:

a) Experimental Results:

Data for the (p,t) reaction on ^{4}He was collected over an angular range from 5^{o} to 35^{o} lab. At larger angles the low energy of the tritons emitted resulted in excessive energy losses in the material between the target and the detector. Triton energy spectra from this reaction are presented in figs. 30 and 31. The spectrum in fig. 30 is a composite of two spectra obtained with different magnet settings, and was obtained to indicate the shape of the continuous triton distribution over a larger range of excitation energy. Shown together with this triton spectrum, which was collected at 5.6^{o} lab. is a spectrum obtained with the helium target empty, indicating the background contribution to the helium spectrum from the target cylinder. Fig. 31 shows additional triton spectra which have been corrected for background. All the spectra in figs, 30 and 31 have been corrected for deuteron feed-through. The main feature of the continuous triton spectrum is the asymmetric high energy peak which is most prominent at small angles. The change in the character of the spectrum between 10^{o} and 20^{o} is quite spectacular as can be seen in fig. 31.

The triton energy scale was obtained from the energy calibration previously determined from the kinematics of the $^{7}Li(p,t)^{5}Li$ reaction. The energies determined for the peak positions were found to correspond to a constant Q value of about - 20 MeV which is consistent with the peaking being due to a final state interaction between the two protons left in the residual nucleus:

The differential cross-section $d^2\sigma/d\Omega dE$ was calculated for the peak height of the continuous distribution and is tabulated together with the associated r.m.s. uncertainties in Table 11 for the lab. coordinate system. The angular distribution for the peak height is given in fig. 32 in the lab. system. It should be noted that these values of the differential cross-section have no absolute meaning since they are dependant on the experimental energy resolution.

b) Discussion:

The only other reported investigation of the $^4He(p,t)2p$ reaction was performed at Orsay by Bernas et al (Be67) at an incident proton energy of 156 MeV. Their experimental observations were essentially the same as those reported here, although their study covered a more limited angular region, measurements being presented for 2^o, 5^o, 10^o and 15^o. The shape of the triton spectrum was similar to that observed here, except that Bernas et al had better resolution, achieved primarily by the use of a low temperature gaseous helium target. By 15^o lab the prominent high energy peak observed by Bernas et al was almost completely indistinguishable.

Two reaction mechanisms can be considered for the production of tritons from the $^4He(p,t)2p$ reaction. In the first, the reaction can be thought of as direct two neutron pick-up resulting in immediate three body break-up, in which the continuous triton spectrum observed is associated with a variable energy in the 2p system. The high triton yield at the maximum energy of the spectrum (at small angles) can be attributed to an enhancement due to the final state interaction (FSI) between the recoiling protons and will be discussed in more detail later. In a $^{3}He(d,t)^{2}He$ experiment, Bilaniuk and Slobodrian (Bi63) interpreted a similar peaking in their spectrum as the decay of a very short lived diproton. Another possible mechanism for the $^{4}He(p,t)2p$ reaction is the sequential process:

$$p + {}^{4}He \longrightarrow {}^{4}He^{*} + p$$
$$\qquad\qquad\qquad\quad \hookrightarrow t + p$$

where the continuous distribution of tritons could be due to excitation of the alpha particle. At large angles (not considered in the present experiment) a charge exchange mechanism would also be possible.

The experimentally observed spectra strongly suggest the direct interaction pick-up mechanism with FSI enhancement at small angles. The rapid change with increasing angle in the character of the observed spectrum most probably implies a change in the dominant reaction mechanism. A similar phenomenon has been observed by Tombrello and Bacher (To65a) for a number of reactions with three bodies in the final state.

Final state interactions have been studied quite extensively in the low energy region ($<$ 50 MeV) in recent years. Most investigations have involved single nucleon transfer reactions on mass 2 and 3 nuclei (see for e.g. Slobodrian et al (Sl67) and contained references) and the analysis of these reactions has usually employed the Watson-Migdal formalism (Wa52, Mi55). In these three-body final-state experiments, the detected particle typically has a high energy and the two remaining particles recoil with low relative momentum q and can therefore interact strongly. The Watson-Migdal theory allows the differential cross-section to be factored (within several limiting assumptions) into independent contributions due to: phase space, the primary reaction mechanism (usually pick-up of one or two nucleons) and an FSI which corresponds to the low energy s-wave scattering between the remaining particles. The contribution from the primary reaction mechanism is generally assumed to be constant over the limited region of the spectrum being analysed and the Watson-Migdal formalism neglects the additional final-state interaction between the detected particle and one of the remaining particles. Bernas et al (Be67) have pointed out that these last two approximations have more validity at higher energies, making their results at 156 MeV more appropriate to the FSI analysis than the lower energy experiments. This would also apply to the present results at 100 MeV. Bernas et al obtained a good fit to their data using the Watson-Migdal treatment and folding in their experimental resolution. The singlet p-p scattering length a_p and effective range r_o used in their analysis were consistent with values determined from low energy scattering experiments. A similar analysis of the present experimental data should yield the same results.

The observed angular distribution follows a pronounced diffraction pattern. A similar distribution was obtained in the $^{3}He(^{3}He,\alpha)2p$ reaction studied at 53 MeV by Slobodrian et al (S167). They fitted their angular distribution using a diffraction calculation due to Dar (Da64) and found evidence for a peripheral picture of the reaction mechanism consisting of an $\ell = 0$ nucleon transfer.

TABLE 11

DIFFERENTIAL CROSS-SECTIONS FOR THE ^{4}He(p,t)2p REACTION:

Lab. Angle degrees	$\frac{d^2\sigma}{d\Omega\, dE}$ lab. μb/ster. MeV
5.6	37.7 ± .5
8.0	29.1 ± .3
10.6	15.7 ± .2
13.0	8.91 ± .13
15.6	3.97 ± .07
18.0	2.01 ± .05
20.6	1.43 ± .04
25.6	2.16 ± .05
30.6	2.52 ± .05
35.5	1.88 ± .04

Note:

a) The errors tabulated above are the r m s errors.

b) The cross-sections are not corrected for nuclear absorption losses in the detector.

c) The overall systematic error for these measurements (not including b) above) is ± 3.6%.

FIGURE 30

TRITON ENERGY SPECTRUM FROM ^{4}He

FIGURE 30

$^4He(p,t)2p$ triton spectrum at 5.6° lab. This continuous spectrum is a composite of two spectra taken with different magnet settings to extend the observed region of excitation. The background spectrum, obtained with an empty target, is also shown. The error bars are for relative uncertainties.

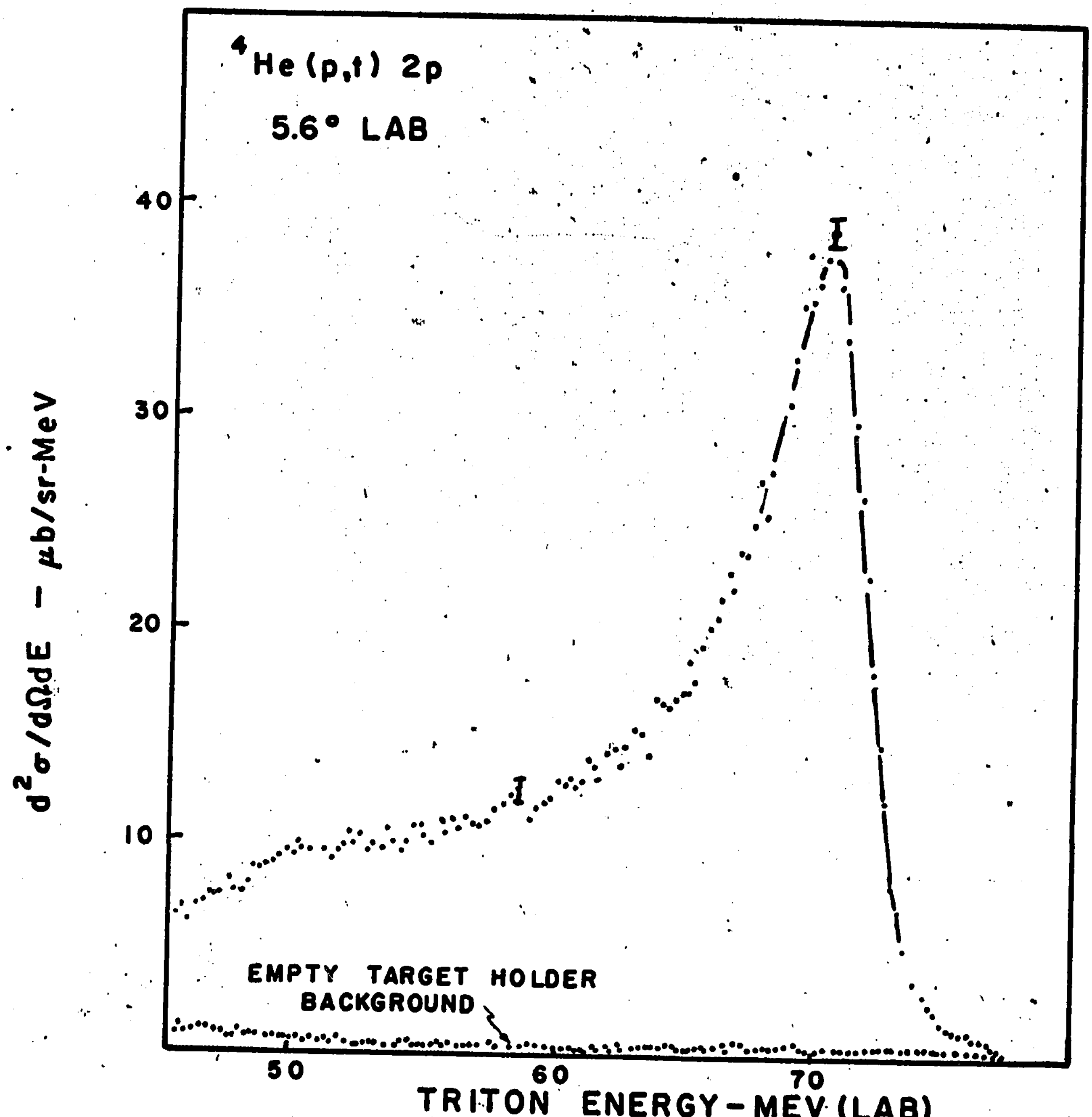

$^4He(p,t)\,2p$
5.6° LAB
40
30
20
10
$d^2\sigma/d\Omega dE$ — $\mu b/sr$-MeV
EMPTY TARGET HOLDER BACKGROUND
50
60
70
TRITON ENERGY-MEV (LAB)

FIGURE 31

MORE TRITON SPECTRA FROM ^{4}He

FIGURE 31

$^{4}He(p,t)2p$ triton spectra at angles from 7.5° to 20° lab. The error bars are for statistical errors.

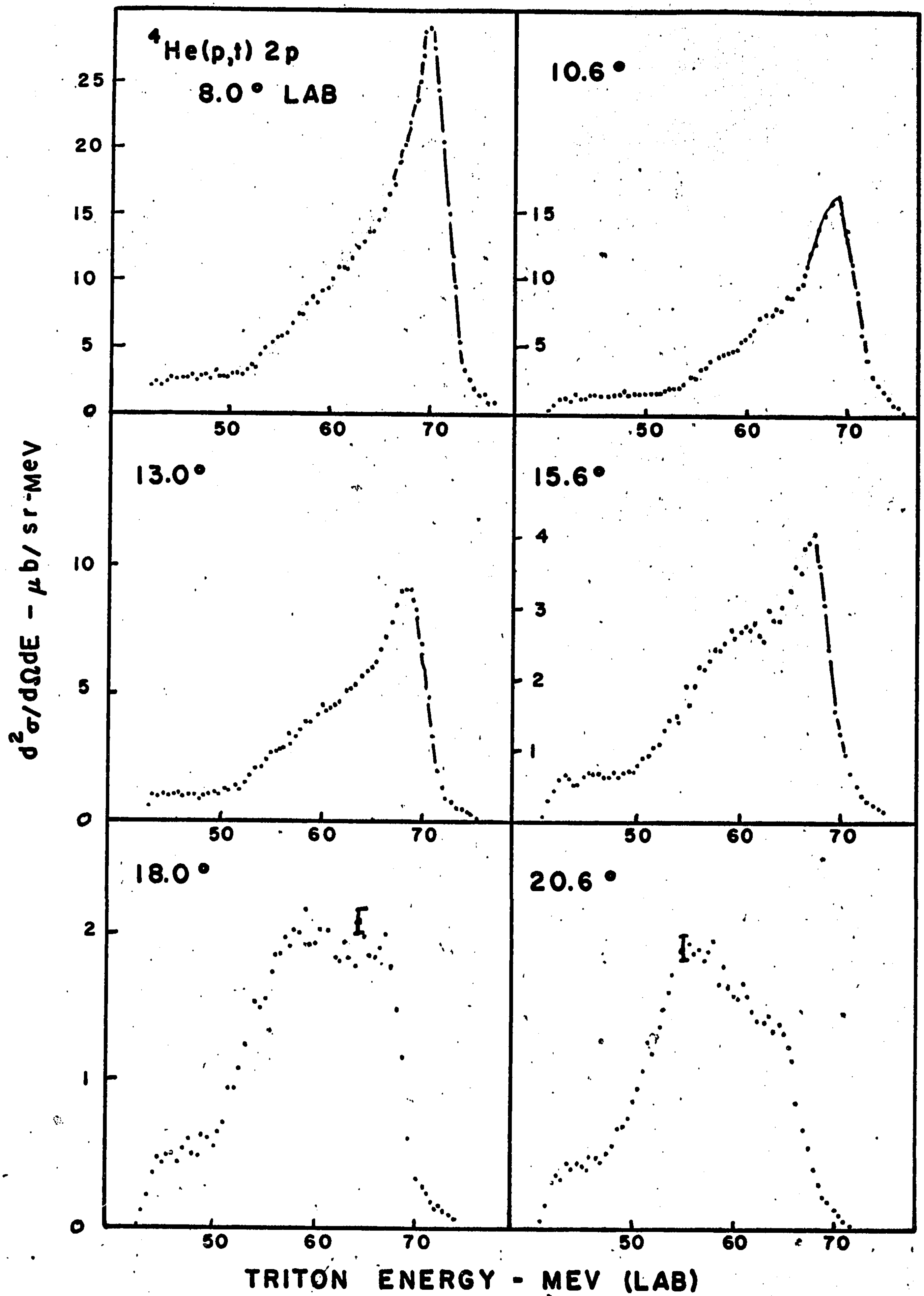

$^4He(p,t)\,2p$
8.0° LAB
10.6°
13.0°
15.6°
18.0°
20.6°
$d^2\sigma/d\Omega dE$ - $\mu b/sr\text{-}MeV$
TRITON ENERGY - MEV (LAB)

FIGURE 32

ANGULAR DISTRIBUTION FOR THE FSI PEAK IN

THE ^{4}He(p,t)2p REACTION.

FIGURE 32

The differential cross-section $(d^2\sigma/d\Omega dE)$ of the FSI peak in the $^4He(p,t)2p$ reaction is plotted as a function of triton angle. The angular distribution is in the lab. system. The error bars shown are for relative uncertainties.

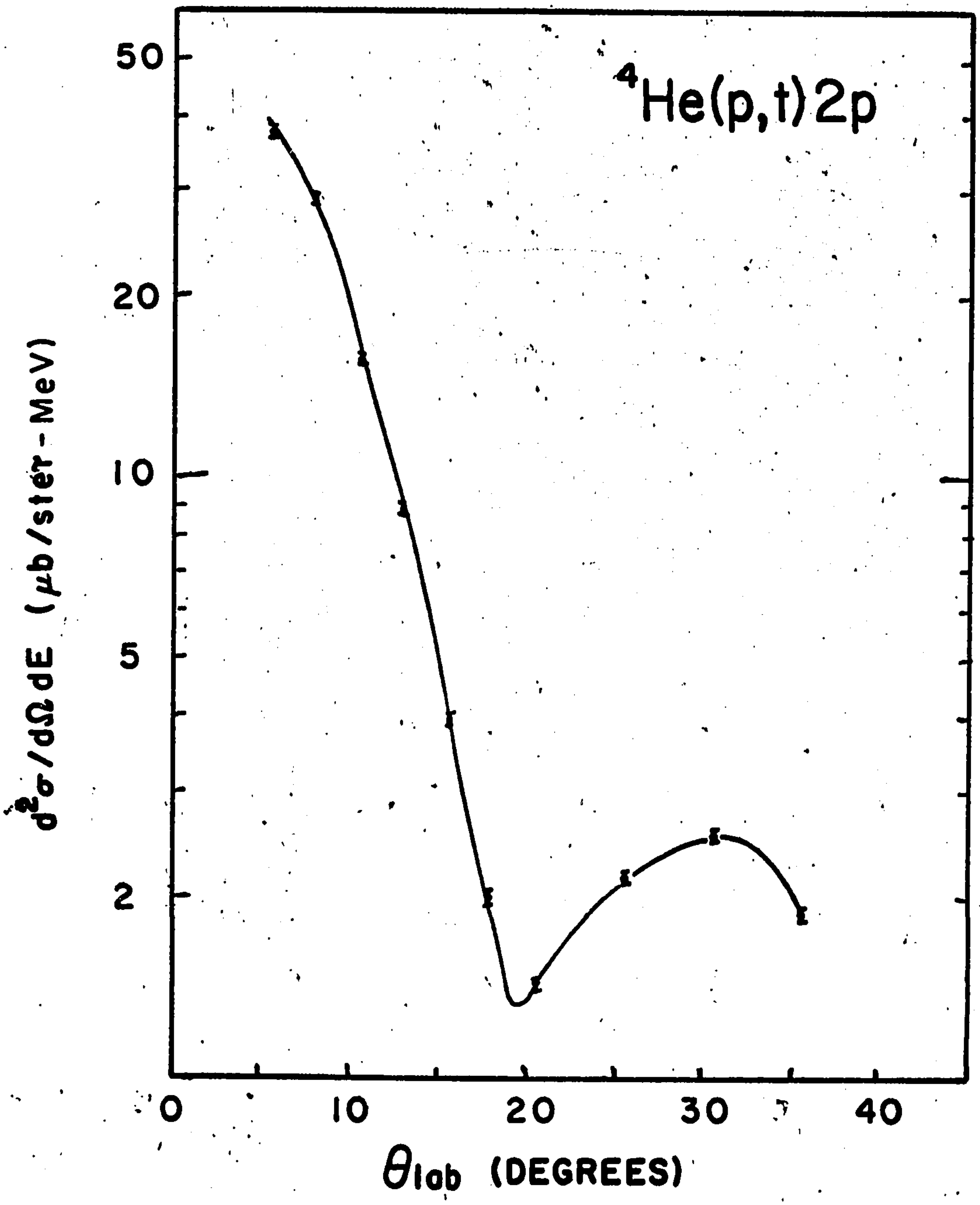

⁴He(p,t)2p
50
20
10
5
2
d²σ/dΩdE (μb/ster-MeV)
0
10
20
30
40
θlab (DEGREES)

CHAPTER 6. THEORETICAL ANALYSES:

6.1. Optical Model Analysis of Elastic Scattering on ^{6}Li and ^{7}Li.

This section presents an optical model analysis of the elastic scattering data for ^{6}Li and ^{7}Li. An optical model search routine due to Held (He66) was used with small modifications to the program to allow greater flexibility in the choice and variation of the optical model parameters.

The form of the optical potential between the incident proton and the target nucleus was:

$$V(r) = V_c(r) - V(1+e^{x})^{-1} - i(W_V - 4W_D\, d/dx')(1+e^{x'})^{-1} + (\hbar/m_\pi c)^2 V_s r^{-1}\, d/dr\,(1+e^{x_s})^{-1}\,\vec{\sigma}\cdot\vec{L}$$

where: $V_c(r)$ is the Coulomb potential for a uniformly charged sphere of radius $r_cA^{1/3}$; V is the real central potential, W_V and W_D the volume and surface parts respectively of the imaginary potential, V_s is the real part of the spin-orbit potential and m_π is the pion mass. The spin-orbit coupling term was taken to be real because no evidence for the necessity of an imaginary part has been found (Sa67). The form factors were Saxon-Woods for the real and imaginary potentials and of the Thomas type for the spin-orbit potential:

$$x = (r - r_oA^{1/3})/a$$

$$x' = (r - r'A^{1/3})/a'$$
$$x_s = (r - r_sA^{1/3})/a_s$$

where r_o, r', and r_s and a, a' and a_s are the radius and diffuseness parameters respectively for the real, imaginary and spin orbit potentials and constitute the geometrical optical model parameters. These parameters and the potential strengths, V, W_v, W_D and V_s which are sometimes refered to as the dynamic optical model parameters, together define the optical potential.

The search program varied the optical model parameters so as to minimize the quantity:

$$\chi^2 = \sum_i \left(\sigma_{exp}(\theta_i) - \sigma_{theo}(\theta_i)\right)^2 / \left(\Delta\sigma_{exp}(\theta_i)\right)^2$$

where $\sigma_{exp.}$ and $\sigma_{theo.}$ are the measured and theoretical cross-sections at θ_i and $\Delta\sigma_{exp.}$ is the error associated with $\sigma_{exp.}$ To ensure that the minimum found by the search was the true minimum and not just a local minimum, several different initial parameters were tried. For the purpose of the optical model analysis, the elastic scattering data reported in the previous chapter were modified so as to combine the angular uncertainties (transformed to equivalent cross-section uncertainties) with the other relative errors.

Fits were obtained for both lithium isotopes using either pure "volume" or pure "surface" absorption (i.e. $W_D = 0$ or $W_v = 0$).

In the first analysis "constrained" spin orbit parameters were used (Sa67) with $r_s = r$ and $a_s = a$ and the seven parameters were varied to give a minimum χ^2. Using the parameters obtained from this fit the analysis was repeated with free spin-orbit parameters. The results of these fits for ^{6}Li and ^{7}Li are given in Tables 12 and 13. The values used for r_c were obtained from the charge distributions determined from electron scattering experiments. The radius used for ^{6}Li was taken from Meyer-Berkhout et al (Me59) and the radius for ^{7}Li was determined from the ^{6}Li radius and a measurement by Streib (St55) of the ratio of the ^{7}Li to ^{6}Li radius.

The best optical model fits are also plotted together with the experimental points in figs. 33 to 36. The fits appear to be quite good in all cases although the surface absorption fit for ^{6}Li is better than the volume fit. The large angle region is not fitted well for either ^{6}Li or ^{7}Li. The fits for ^{7}Li are not as good as those for ^{6}Li, both subjectively and in terms of χ^2, but it should be remembered that the angular distribution for ^{7}Li contains, at least at large angles, a substantial contribution from the first excited state.

Several general observations can be made regarding the optimum parameters obtained from the analyses. First it can be seen that the "constrained" optical model fit is somewhat worse in each case than the fit with free spin orbit parameters. The changes produced in the other parameters by introducing the additional freedom for r_s and a_s is however quite small. Satchler (Sa67) in a comprehensive optical model analysis of 30 MeV proton scattering, found that while the cross-sections could be fitted very well with the constrained form ($r_s=r_o$, $a_s=a$) of the optical potential, the polarization data demanded that at least one of these parameters take on a different value.

The spin orbit radius r_s was found in all cases to be smaller than the real central radius r_o. This has been observed before in other similar analyses, (Gr65, Bl66) and has been interpreted by Greenlees et al (Gr67) in terms of the interaction of the incident proton with the nuclear matter distribution via the two-body nucleon-nucleon force.

It is also interesting to note that the diffuseness parameter for ^{6}Li is very large both in comparison with ^{7}Li and with results obtained in similar analyses for other nuclei. This is most probably explained as a clustering effect since there is much evidence (Ta62) that the ground state of ^{6}Li has a predominant (α + d) cluster structure. The clusters are only bound by 1.5 MeV and so on the average are quite far apart, behaving much like free particles. The deuteron is known to have a long tail to its distribution and this is manifested in ^{6}Li by the deuteron cluster giving rise to the large diffuseness.

Very few optical model analyses have been reported for proton scattering from the lithium isotopes. ^{7}Li has been analysed at 180 MeV both by Johannson et al (Jo61) and by Satchler and Haybron (Sa64) who found a better fit with surface absorption, the volume absorption fit oscillating too severely (as it did in the present analysis) at the larger angles. ^{6}Li has been analysed using a fairly restricted set of parameters by Kull (Ku67) at 40 MeV, but it is difficult to make any comparison with the present results.

Finally it is observed that for both ^{6}Li and ^{7}Li, the volume absorption gave considerably lower reaction cross-sections σ_{tot} than the corresponding surface absorption case. This is related directly to the fit at small angles which appears to be slightly better for the volume absorption, the surface absorption model overestimating the cross-sections in the coulomb interference region. The only reported measurement on the lithium isotopes of the total reaction cross-section, is for ^{7}Li at 180 MeV (Jo61a). The measured cross-section is 149 ± 3 mb. which is lower than those determined from the optical model fits described above. Taking into account the energy dependence of the total reaction cross-section, this would tend to favour the volume absorption fits. Subsequent to the work presented above, there has been a publication (Su67) of new and more accurate values of the charge distributions of ^{6}Li and ^{7}Li from electron scattering data. The new values of the radius parameter r_c are 1.81 ± 0.04 f and 1.71 ± 0.04 f respectively. However the fitting is not very sensitive to the value of r_c and consequently the results presented above should not change significantly.

TABLE 12

OPTIMUM OPTICAL POTENTIAL PARAMETERS FOR ^{6}LI

	Surface Absorption (W_V=0)		Volume Absorption (W_D=0)	
	7 Param.	9 Param.	7 Param.	9 Param.
V(Mev)	-18.87	-18.76	-18.04	-18.25
r_o (fm)	1.099	1.095	1.136	1.164
a(fm)	0.632	0.719	0.930	0.877
W(Mev)	-7.82	-7.82	-20.16	-20.78
r'(fm)	1.114	1.070	1.016	0.987
a'(fm)	0.611	0.628	0.564	0.573
V_s(Mev)	4.16	4.22	4.02	3.73
r_s(fm)	1.099	1.044	1.016	1.157
a_s(fm)	0.632	0.547	0.930	0.849
r_c(fm)	1.92	1.92	1.92	1.92
χ^2	64	25	123	92
σ_{tot}(mb)		189		156

Note:

a) The 7 parameter analyses refer to constrained spin orbit coupling r_s=r_o, a_s=a.

b) r_c was obtained from electron scattering data (Me59).

c) The reaction cross section σ_{tot} was not calculated for the 7 parameter analyses.

TABLE 13

OPTIMUM OPTICAL POTENTIAL PARAMETERS FOR ^{7}LI

	Surface Absorption (W_V=0)		Volume Absorption (W_D=0)	
	7 param.	9 param.	7 param.	9 param.
V (Mev)	-16.35	-16.12	-16.04	-16.04
r_o(fm)	1.257	1.292	1.467	1.472
a (fm)	0.458	0.574	0.661	0.651
W (Mev)	- 7.80	- 7.03	-26.09	-26.43
r'(fm)	1.226	1.271	1.084	1.079
a'(fm)	0.632	0.622	0.437	0.441
V_s(Mev)	4.82	4.80	2.24	2.16
r_s(fm)	1.257	1.262	1.467	1.459
a_s(fm)	0.458	0.444	0.661	0.639
r_c(fm)	1.78	1.78	1.78	1.78
χ^2	106	61	79	76
σ_{tot}(mb)		225		189

Note:

a) The 7 parameter analyses refer to constrained spin orbit coupling r_s=r_o, a_s=a.

b) r_c was obtained from electron scattering data (Me59, St55).

c) The reaction cross section σ_{tot} was not calculated for the 7 parameter analyses.

FIGURE 33

OPTICAL MODEL FIT TO ELASTIC SCATTERING FROM

^{6}Li - SURFACE ABSORPTION

FIGURE 33

Optical model fit to $^{6}Li(p,p)^{6}Li$ using an optical potential containing a surface imaginary term. See text for details.

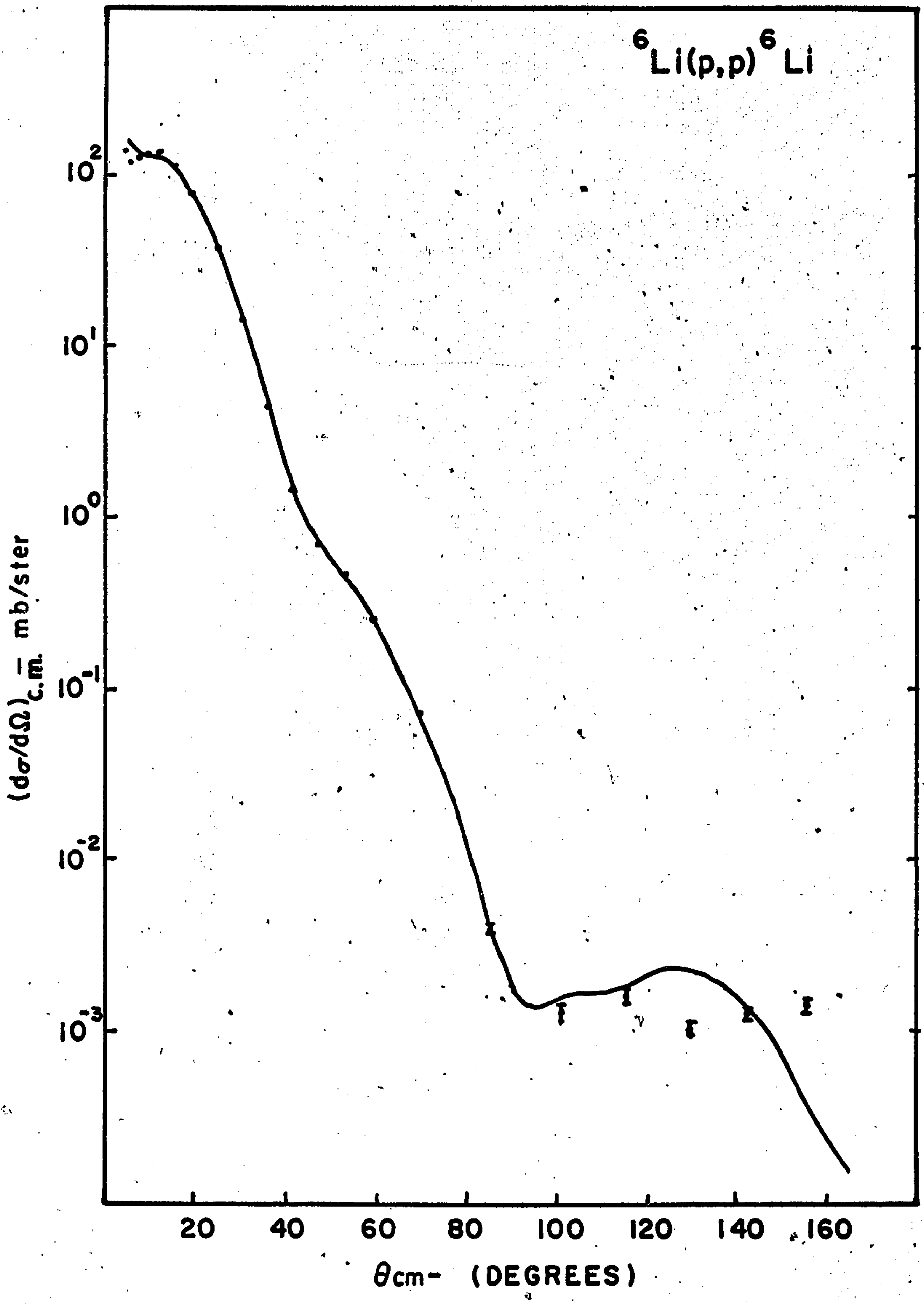

$^6Li(p,p)^6Li$
10^2
10^1
10^0
10^{-1}
10^{-2}
10^{-3}
$(d\sigma/d\Omega)_{c.m.}$ – mb/ster
20 40 60 80 100 120 140 160
θcm– (DEGREES)

FIGURE 34

OPTICAL MODEL FIT TO ELASTIC SCATTERING FROM ^{6}Li - VOLUME ABSORPTION.

FIGURE 34

Optical model fit to $^{6}Li(p,p)^{6}Li$ using an optical potential containing a volume imaginary term. See text for details.

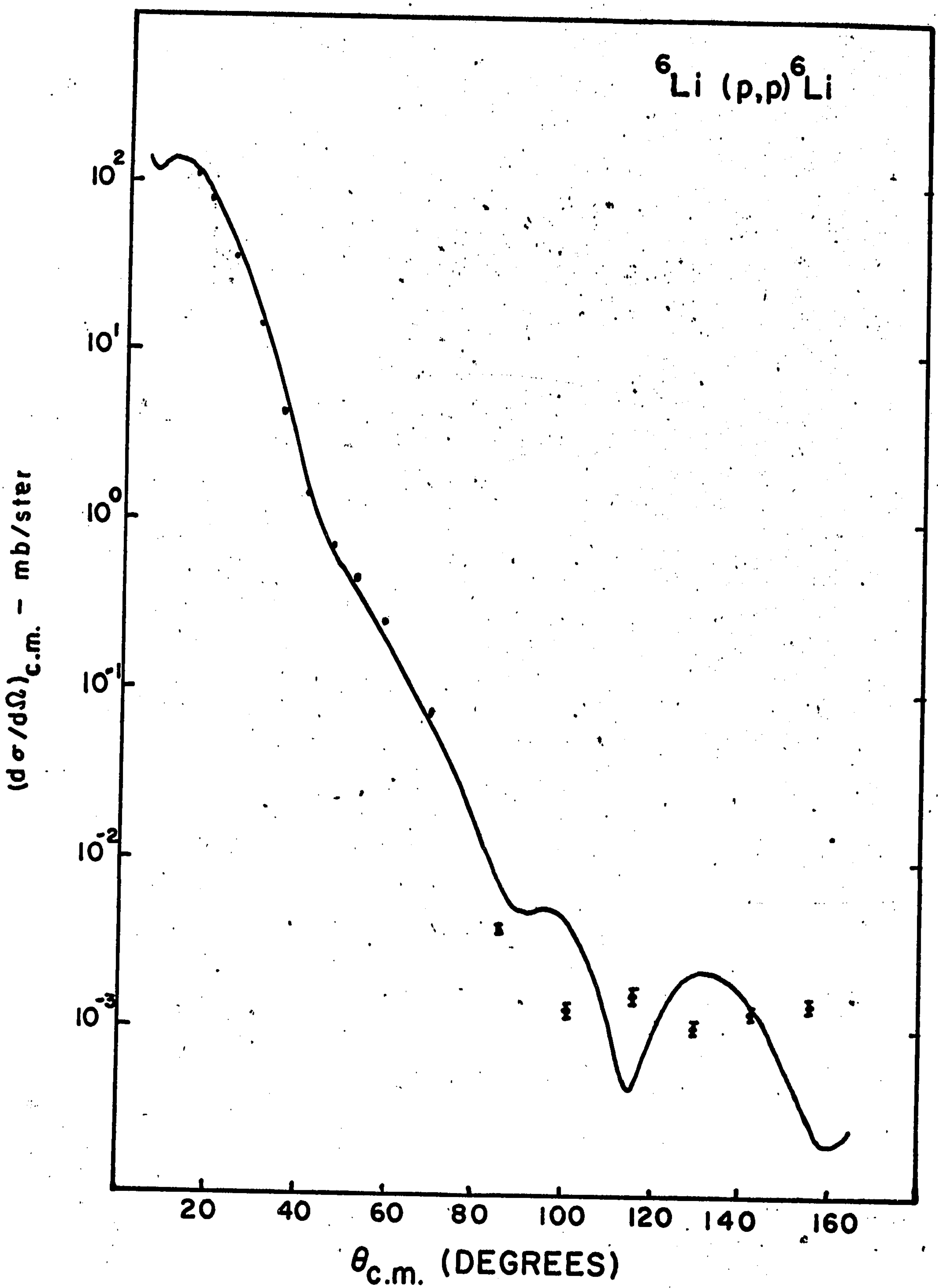

$^6Li\ (p,p)^6Li$
10^2
10^1
10^0
10^{-1}
10^{-2}
10^{-3}
$(d\sigma/d\Omega)_{c.m.}$ - mb/ster
20
40
60
80
100
120
140
160
$\theta_{c.m.}$ (DEGREES)

FIGURE 35

OPTICAL MODEL FIT TO ELASTIC SCATTERING FROM

^{7}Li - SURFACE ABSORPTION

FIGURE 35

Optical model fit to $^{7}Li(p,p)^{7}Li$ using an optical potential containing a surface imaginary term. See text for details.

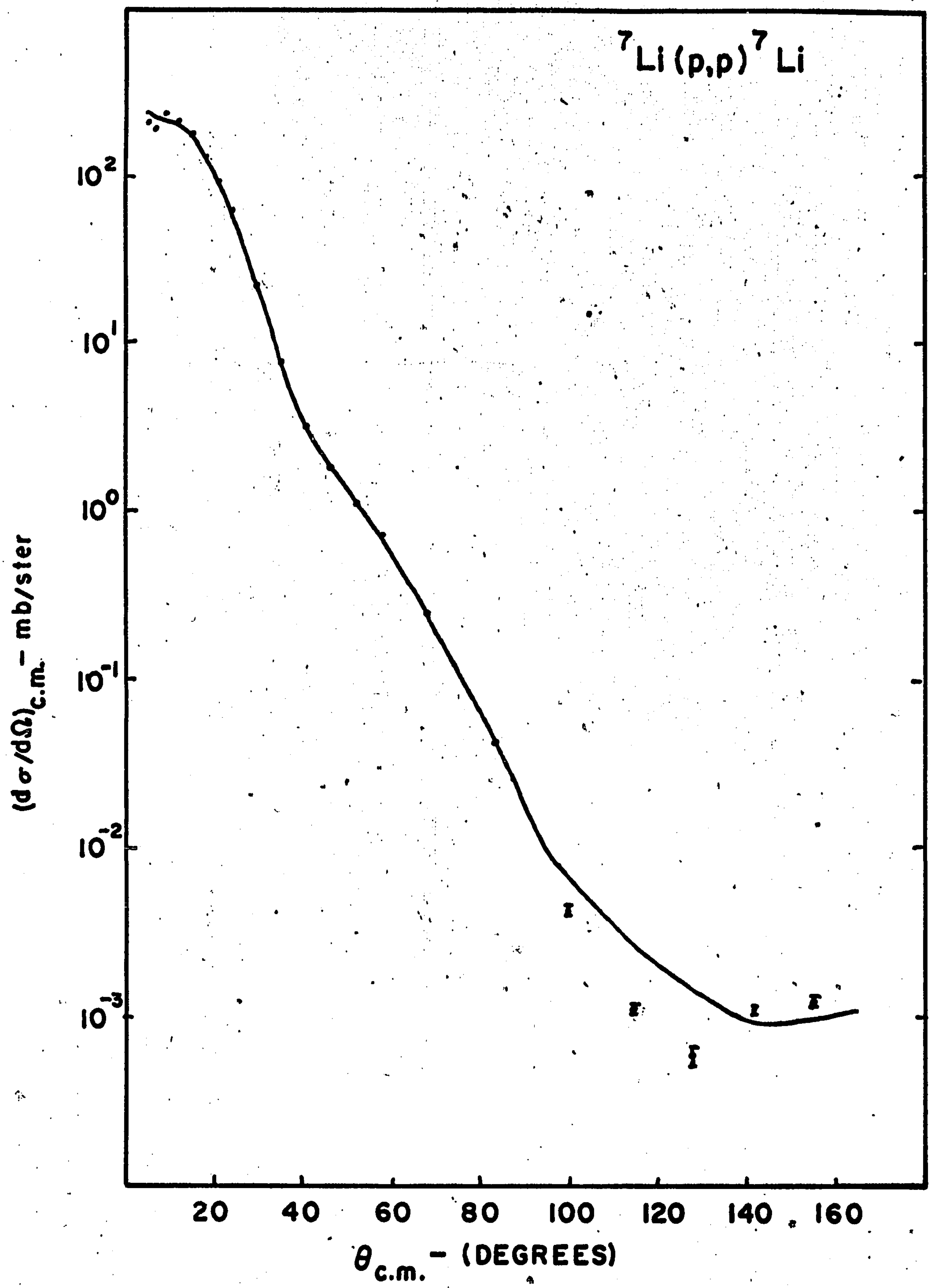

$^7Li(p,p)^7Li$
10^2
10^1
10^0
10^{-1}
10^{-2}
10^{-3}
$(d\sigma/d\Omega)_{c.m.}$ - mb/ster
20
40
60
80
100
120
140
160
$\theta_{c.m.}$ - (DEGREES)

FIGURE 36

OPTICAL MODEL FIT TO ELASTIC SCATTERING FROM ^{7}Li - VOLUME ABSORPTION.

FIGURE 36

Optical model fit to $^{7}Li(p,p)^{7}Li$ using an optical potential containing a volume imaginary term. See text for details.

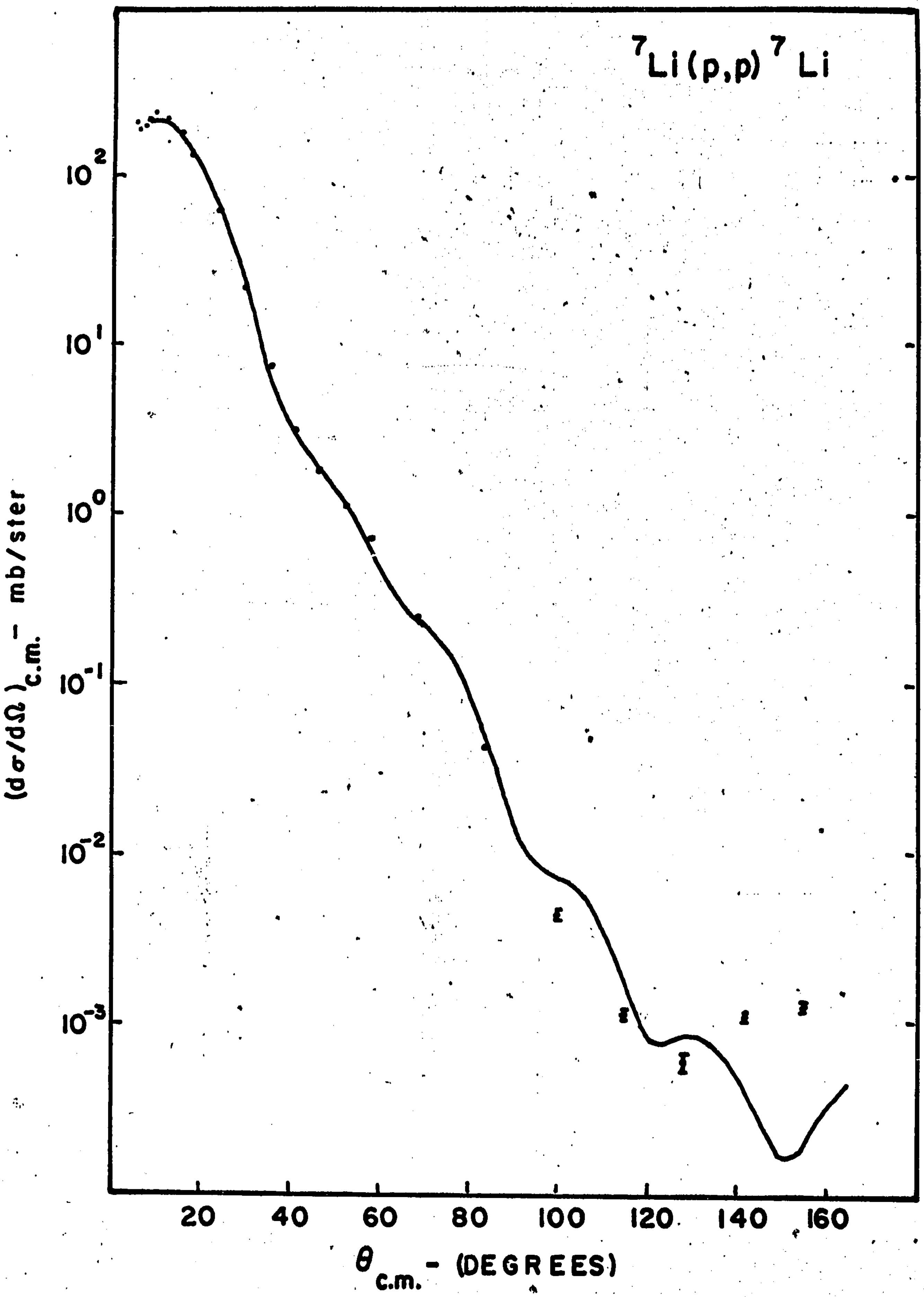

$^7Li(p,p)^7Li$
10^2
10^1
10^0
10^{-1}
10^{-2}
10^{-3}
$(d\sigma/d\Omega)_{c.m.}$ - mb/ster
20
40
60
80
100
120
140
160
$\theta_{c.m.}$ - (DEGREES)

6.2 D.W.B.A. Analysis of (p,t) Reactions on ^{6}Li and ^{7}Li.

This section presents a preliminary distorted wave Born approximation (DWBA) analysis of the two neutron pick up reactions $^{7}Li(p,t)^{5}Li$ and $^{6}Li(p,t)^{4}Li$ described in the previous chapter. The analysis was made by Hardy (Ha67) using the Oxford DWBA code. This program is similar to the code SALLY of Bassel et al (Ba62) in that a "form factor" containing the information describing the effective interaction is kept as a separate term in the radial overlap integral. The differential cross-section is calculated using the zero range approximation and neglecting spin-orbit interactions. The final normalization of the cross-section is arbitrary. All well shapes are assumed to be Saxon-Woods.

Unfortunately, at the time the calculations were made, no appropriate optical model parameters were available and so reasonable estimates had to be used. The optical model parameters used in the analyses of both the $^{7}Li(p,t)^{5}Li$ and $^{6}Li(p,t)^{4}Li$ reactions are given in Table 14.

TABLE 14

Optical Model Parameters used in DWBA Analysis of (p,t) Reactions on ^{6}Li & ^{7}Li

	V (Mev)	r_0 (fm)	a (fm)	W_v (MeV)	r' (fm)	a' (fm)	r_c (fm)
Proton	30	1.2	0.70	15	1.2	0.70	1.3
Triton	120	1.3	0.65	30	1.3	0.65	1.3

The imaginary potential was chosen as volume absorption W_v, the other parameters having the same definition as in section 6.1. The bound state parameters used were a = 0.60 fm and r = 1.3 fm.

DWBA fits were obtained with these parameters and are shown in figs. 37 and 38, arbitrarily normalized to the experimental angular distributions at 10°c.m. The $^{7}Li(p,t)^{5}Li$ reaction was analysed for both $\ell = 0$ and $\ell = 2$ angular momentum transfer and the $^{6}Li(p,t)^{4}Li$ analysis used $\ell = 1$. Qualitatively the fits for the $^{7}Li(p,t)^{5}Li$ reaction are quite good, especially considering the approximate nature of the parameters used. In the case of ^{6}Li, however, the agreement is rather poor, probably reflecting an extremely poor choice of parameters for the ^{4}Li - triton channel.

It is expected that the use of the optical model parameters obtained in section 6.1 for protons scattering elastically on ^{6}Li and ^{7}Li will improve the fits; however the problem of obtaining good optical model parameters for tritons at intermediate and high energies still remains, due to a complete lack of the relevant experimental data. However an improvement in the fits should be possible using the proton parameters determined in the previous section (6.1) and varying the triton parameters systematically.

FIGURE 37

DWBA ANALYSIS FOR $^{6}Li(p,t)^{4}Li$

FIGURE 37

A preliminary DWBA analysis of the ^{6}Li(p,t)^{4}Li reaction is shown. An orbital angular momentum transfer $\ell = 1$ was used.

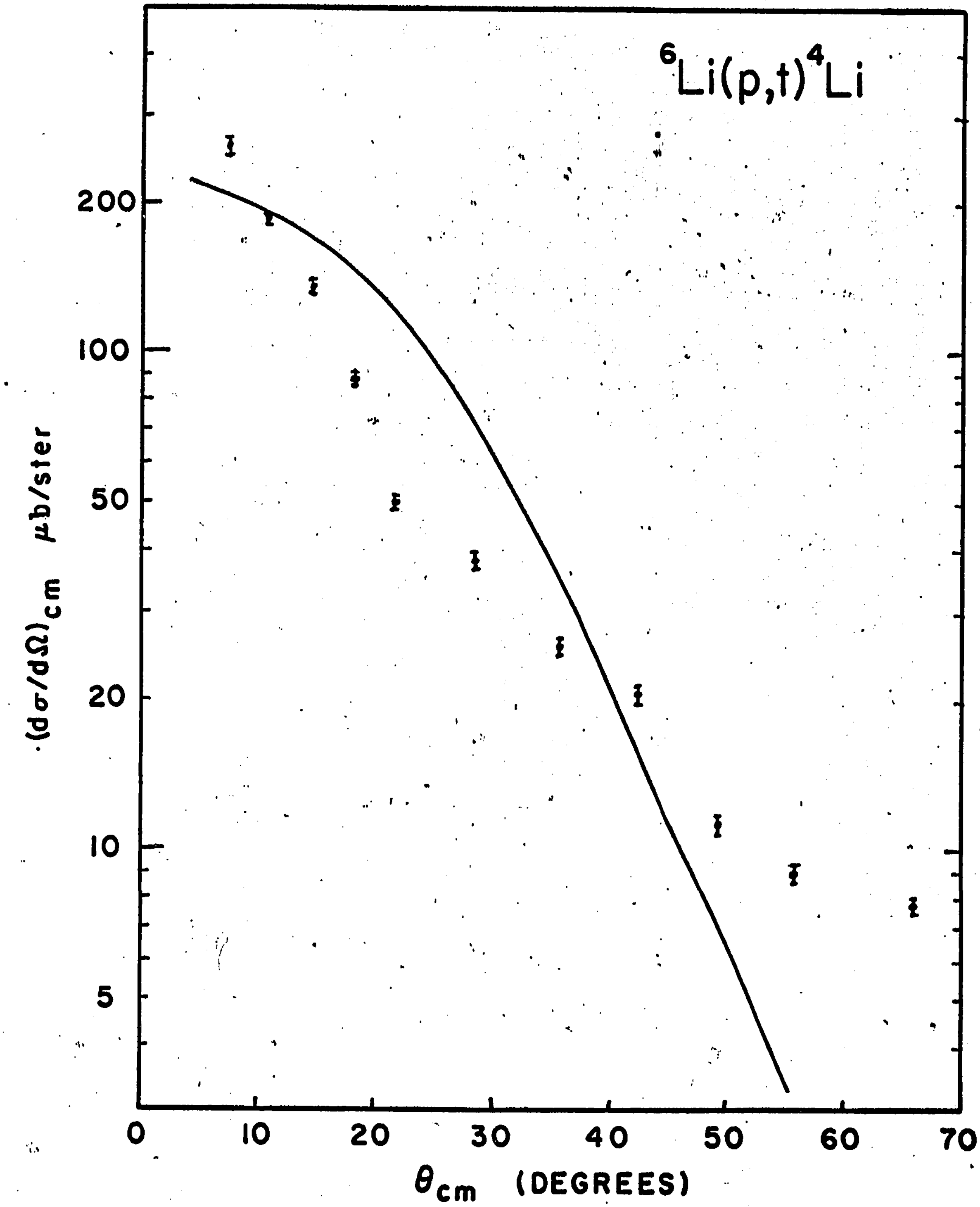

$^6Li(p,t)^4Li$
200
100
50
20
10
5
$(d\sigma/d\Omega)_{cm}$ μb/ster
0
10
20
30
40
50
60
70
θ_{cm} (DEGREES)

FIGURE 38

DWBA ANALYSIS FOR $^{7}Li(p,t)^{5}Li$

FIGURE 38

A preliminary DWBA analysis of the $^{7}Li(p,t)^{5}Li$ reaction is shown. Distributions were calculated for orbital angular momentum transfer $\ell = 0$ and $\ell = 2$.

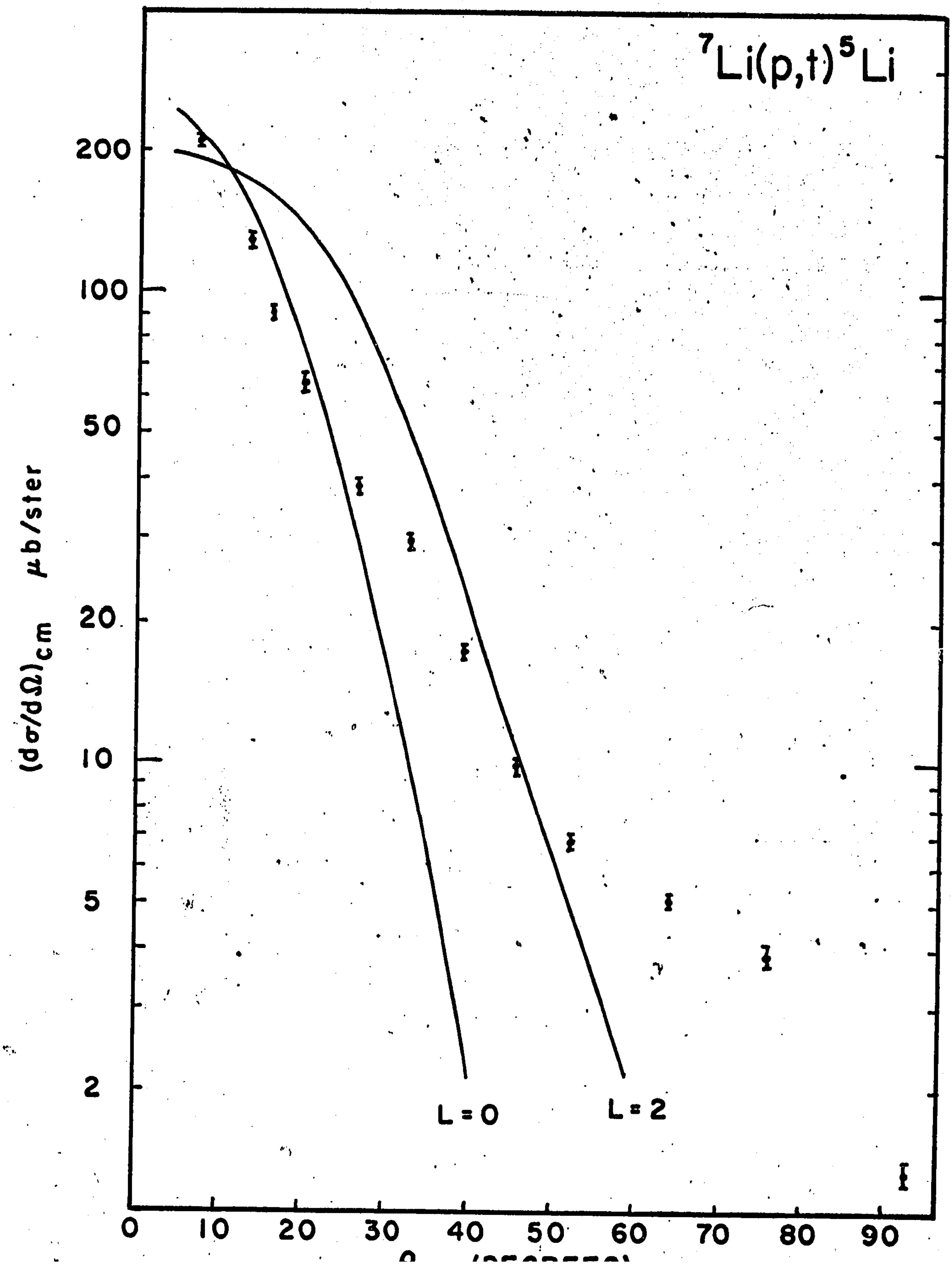

⁷Li(p,t)⁵Li
200
100
50
20
10
5
2
(dσ/dΩ)cm μb/ster
L = 0
L = 2
0
10
20
30
40
50
60
70
80
90

CHAPTER 7. SUMMARY AND CONCLUDING DISCUSSION:

7.1 Experimental System:

The experimental system consisting basically of a 14^{o} sector magnet for "crude" species separation and a fast plastic counter telescope for particle detection, has been found to be very flexible in the study of nuclear reactions. Probably the most significant advantage afforded by the analyser magnet system over other more conventional particle identification systems is related to the fact that the detector only sees a small, selected band of particles. The study of low cross-section reactions is greatly enhanced by this rejection of undesired background. This is particularly relevant for accelerators of low duty cycle (such as synchrocyclotrons) where counting rate limitations based on competing reactions with high cross-section may make the study of a reaction of much lower cross-section impractical by conventional means. A typical example which might be cited is the case of (p,p), (p,d), and (p,t) reactions on ^{6}Li, investigated in this work. In the small angle region the (p,d) cross-section is of the order of 2% of the cross-section for elastic scattering and the (p,t) cross-section is almost three orders of magnitude lower than that for elastic scattering. This immediately imposes a strong limitation on identification systems employing electronic methods. The problem has, to some extent, been alleviated by the recent advent of stochastic extraction for synchrocyclotrons, which has greatly improved the pulsed beam duty cycles.

The most serious limitation of the experimental system is the energy resolution afforded by the plastic scintillators. In spite of the fact that the resolution has been significantly improved over previously reported energy resolutions with plastic counters, the study of anything but light nuclei is precluded. The intrinsically lower light efficiency of plastic for deuterons, tritons, ^{3}He's and alphas compounds this disadvantage. The light output from plastic scintillators for doubly charged particles is of the order of 40% of that for protons. This together with the high rate of ionization of α's and ^{3}He's and consequent energy losses in the path to the detector, makes the present system quite unsuited to their study. A brief investigation of the ^{7}Li$(p,\alpha)^4$He reaction confirmed this fact. Two additional difficulties in the detection of α's (or ^{3}He's) exist: the magnetic selection does not separate alphas and ^{3}He's very well and the lower efficiency of the ΔE scintillator further complicates the distinction between these two doubly charged particles. In addition to this is the problem of a very high background of protons whose magnetic rigidities are very nearly the same as those of the selected alphas.

A possible improvement to the detection system might be a change to a NaI(Tl) E counter. NaI has intrinsically better energy resolution than plastic and even more important, has a slightly increased efficiency for detection of particles heavier than protons. The serious sacrifices in counting rate which could be the consequences of using NaI (due to the slower response and increased sensitivity to gamma background) may well be offset by the use of the presently available stretched beam.

A detailed analysis of the properties of the analyser magnet system has been made, an outline of which has been presented in a previous chapter. A comprehensive set of additional tables of the magnet properties is also available. The necessity of good beam quality to fully utilize the capability of the system is illustrated by the strong dependence of the energy "bite" on the beam spot size, and this may in some cases be a disadvantage (as with an extended target such as the liquid helium target used in part of this experiment). A possible improvement to the analyser magnet would be the installation of a permanent Hall probe in the magnet pole gap, enabling calibration and subsequent setting of the magnetic field which is less susceptible to hysteresis effects.

A liquid helium cryogenic target was designed and constructed. By avoiding weaknesses inherent in previous designs, a cryostat with a ^{4}He consumption rate of about 45 cc/hour was achieved. This represents a considerable improvement over previously reported helium targets.

Finally an improvement in the beam monitoring would be desirable. This could be achieved by the addition to the experimental system of a continuous (transmission) secondary monitor for beam current measurement. An ionization chamber or similar device would allow considerably improved calibration of the Faraday Cup.

7.2 Summary of Results:

The differential cross-sections for elastic scattering from ^{6}Li and ^{7}Li have been measured over a large angular range and the angular distributions have been fitted by an optical model analysis. There is very little data or analysis in this region of energy for light nuclei and a systematic analysis of optical model parameters is not yet possible. There was no evidence in the angular distribution for the strong backward peaking which has been observed in proton scattering from s-shell nuclei and interpreted (Go67) as an exchange effect. However, the exchange amplitude is not expected to be significant in p-shell nuclei.

Angular distributions were also obtained for inelastic scattering from several levels in ^{6}Li and ^{7}Li. A further analysis of the inelastic scattering would require a DWBA or generalized optical model analysis. (Ba62a)

One and two-neutron pick-up reactions have been studied for both lithium isotopes and angular distributions have been obtained for the ground state transitions in the reactions : ^{6}Li(p,d)^{5}Li, ^{6}Li(p,t)^{4}Li and ^{7}Li(p,t)^{5}Li. The (p,d) reaction on ^{6}Li and (p,t) reaction on ^{7}Li, both leading to the same residual nucleus (^{5}Li), have been compared within the framework of the L-S coupling shell model and the cluster model. The (p,t) reaction on ^{6}Li provided new, although inconclusive, evidence for the existence of an unbound ground state in ^{4}Li. A preliminary DWBA analysis was made for the (p,t) reactions on

^{6}Li and ^{7}Li, the results of the analysis being surprisingly good for ^{7}Li and rather poor for ^{6}Li. An improved DWBA analysis using the optical model parameters obtained from the elastic scattering (previously discussed) is indicated.

Several reactions have been studied using a helium target. In a search for unbound levels in ^{4}He via the ^{4}He(p,p')^{4}He* reaction only the known 22 MeV level was observed. An investigation of the ^{4}He(p,d)^{3}He* reaction gave no indication of excited states in ^{3}He, contradicting results of Kim et al (Ki66), but in agreement with most other investigations. The (p,t) reaction on ^{4}He was studied and strong final state interaction effects were observed in the forward angles, with the dominant reaction mechanism appearing to change at larger angles. A more detailed analysis using the Watson-Migdal (Wa52, Mi55) formalism is indicated.

7.3 Future Experiments:

An experiment is now being planned to further investigate the existence of excited states in ^{3}He via inelastic proton scattering, and to extend the study of final state interactions to the ^{3}He(p,d)2p reaction. The proposed experiment will employ a liquid ^{3}He target, providing a significant improvement over previous experiments using gas targets. Apart from the obvious advantages of a liquid target (greater density and consequently increased true event to background ratio), this will eliminate the serious problem of impurities which has beset interpretation of the results of most experiments using gas targets. Liquefication of the ^{3}He gas into a target will be accomplished by small modifications of the cryogenic target constructed for the experiments discussed in this thesis. The target appendage will be isolated from the ^{4}He reservoir and a 1 mm diameter stainless steel feed tube for the ^{3}He gas will extend through the reservoir and out of the top of the cryostat to a closed ^{3}He system. Liquefication of the ^{3}He gas will then be achieved by filling the reservoir (as previously) with liquid ^{4}He and pumping on the ^{4}He liquid to lower its temperature below the boiling point of ^{3}He($\sim 3.2^o$K). The ^{4}He vapour pressure and consequently the ^{4}He temperature will be regulated by the use of a Cartesian manostat so as to maintain a constant ^{3}He vapour pressure above the liquid ^{3}He thus produced. An additional heat shield at the liquid ^{4}He temperature (i.e. in thermal contact with the reservoir) surrounding the target will minimize radiative heat transfer.

Other experiments on one and two neutron pick-up from selected light nuclei are also planned. Further scattering experiments, and a systematic optical model study in this energy region would also be useful.

REFERENCES

Aj59 AJZENBERG-SELOVE, F., LAURITSEN T., Nucl. Phys. 11 (1959) 1

Au60 AUSTERN N, "Proceedings of the International Conference on Nuclear Structure", Kingston, University of Toronto Press (1960) p.323

Ba56 BALDWIN J., CHAMBERLAIN O., SEGRE E., TRIPP R., WIEGAND C., YPSILANTIS T., Phys. Rev. 103 (1956) 1502

Ba62 BASSEL R.H., DRISKO R.M., SATCHLER G.R., Oak Ridge Internal Report ORNL-3240 (1962)

Ba62a BASSEL R.H., SATCHLER G.R., DRISKO R.M., ROST E., Phys. Rev. 128 (1962) 2693

Ba64 BASSANI G., HINTZ N.M., KAVALOSKI C.D., Phys. Rev. 136 (1964) B1006

Ba65 BACHELIER D., BERNAS M., BRISSAUD I., RADVANYI P., ROY M., Phys. Lett. 16 (1965) 304

Ba66 BACHELIER D., BERNAS M., BRISSAUD I., CHAVY F., RADVANYI P., "Colloque sur les Noyaux Legers". Lyon 1966

Ba67 BACHELIER D., BERNAS M., BRISSAUD I., DETRAZ C., LEE J., RADVANYI P., (1967) preprint

Bd66 BALDIN A.M., Soviet Journal of Nucl. Phys. 2 (1966) 151

Be66 BELL R. E., 1966 (private communication)

Be67 BERNAS M., LEE J.K., BACHELIER D., BRISSAUD I., DETRAZ C., RADVANYI P., ROY M., Phys. Lett. 25B (1967) 260

Bi63 BILANIUK O.M., SLOBODRIAN R.J., Phys. Lett. 7 (1963) 77

Bl66 BLUMBERG L.N., GROSS E.E., VAN DER WOUDE A., ZUCKER A., BASSEL R.H., Phys. Rev. 147 (1966) 812

Bo36 BOHR N., Nature 137 (1936) 344

Br60 BREIT G., HULL M.H. Jr., LASSILA K.E., PYATT K.D. Jr., Phys. Rev. 120 (1960) 2227

Bu57 BUTLER S.T., "Nuclear Stripping Reactions", John Wiley and Son Inc., N.Y. (1957)

Ce66 CERNY J., DETRAZ C., PEHL R.H., Phys. Rev. 152 (1966) 950

Ce66a CERNY J., DETRAZ C., PEHL R.H., Phys. Rev. Lett. 15 (1965) 300

Ch58 CHEN S., HINTZ N.M., "Congress International de Physique Nucleaire", Paris 1958 Dunod (Paris) p 387

Ch60 CHEN S., HINTZ N.M., "Proceedings of the International Conference on Nuclear Forces and the Few Nucleon Problem", Pergammon Press (1960) p 683

Ch63 CHESTERFIELD C.M., SPICER B.M., Nuclear Phys. 41 (1963) 675

Cl61 CLEGG A.B., FOLEY K.J., SALMON G.L., SEGEL R.E., Proc. Phys. Soc. 78 (1961) 681

Cl62 CLEGG A.B., Nucl. Phys. 33 (1962) 194

Co62 CORMACK A.M. Nucl. Instr, & Meth. 15 (1962) 268

Da64 DAR A., Nucl. Phys. 55 (1964) 305

De63 DEVINS D.W., FORSTER H.H., Bull. Am. Phys. Soc. 8 (1963) 12

Ei63 EISBERG R., MAYO S., SCHIMMERLING W., Nucl. Instr. & Meth. 21 (1963) 232

Fa67 FANNON J.A., BURGE E.J., SMITH D.A., GANGULY N.K., Nucl. Phys. A97 (1967) 263

Ga55 GAFFNEY J., CLEMENT J.R., Rev. Sci. Instr. 26 (1955) 620

Gl65 GLENDENNING N.K., Phys. Rev. 137 (1965) 102

Go60 GOODING T.J., PUGH H.G., Nucl. Instr. & Meth. 7 (1960) 189

Go64 GOULDING F.S., LANDIS D.A., CERNY J., PEHL R.H., Nucl. Instr. & Meth. 31 (1964) 1

Go66 GOULDING F.S., et al IEEE Trans NS-13 (1966) 514

Go67 GOLDSTEIN N.P., Ph.D. Thesis, McGill University, 1966 (unpublished)

Gr65 GREENLEES G.W., PYLE G.J., Bull. Am. Phys. Soc. 10 (1965) 1203

Gr67 GREENLEES G.W., PYLE G.J., TANG Y.C., (1967) preprint

Ha50 HADLEY J., YORK H., Phys. Rev. 80 (1950) 345

Ha64 HASSELGREN D., INGMARSSON A., RENBERG P.U., SUNDBERG O., TIBELL G., "Comptes Rendus Congres International de Physique Nucleaire, Paris (1964) CNRS (Paris) p 406

Ha65 HASSELGREN D., RENBERG P.U., SUNDBERG O., TIBELL G., Nucl. Phys. 69 (1965) 81

Ha67 HARDY J.C., 1967 (private communication)

He66 HELD A.E., PhD Thesis, McGill University, 1966 (unpublished)

Ho61 HOARE F.E., JACKSON L.C., KURTI N., "Experimental Cryophysics" Butterworths, London (1961) p 361

Ho62 HODGMAN C.D., ed. "Handbook of Chemistry and Physics", Chemical Rubber Publishing Co. (1962)

Im64 IMHOF W.L., VAUGHN F.J., CHASE L.F.,Jr. GRENCH H.A., WALT M., Nucl. Phys. 59 (1964) 81

Ja62 JACKSON D.F., Nucl. Phys. 35 (1962) 194

Ja63 JACMART J.C., GARRON J.P., RIOU M., RUHLA C., "Proceedings of the Conference on Direct Interactions & Nuclear Reaction Mechanisms", Padua 1962, Gordon & Breach (N.Y.) 1963, p 1145

Ja64 JACMART J.C., et al, Phys. Lett. 8 (1964) 269

Ja65 JACKSON D.F., MAHALANABIS J., Nucl. Phys. 64 (1965) 97

Ja67 JARMIE N., STOKES R.H., OHLSEN G.G., NEWSOME R.W. Jr., Phys. Rev. 161 (1967) 1050

Jo58 JOHNSTON L.H., SERVICE D.H., SWENSON D.A., IRE Trans Nucl. Sci., NS 5 (1958) 95

Jo60 JOHANSSON A., TIBELL G., PARKER K., HODGSON P.E., Nucl. Phys. 21 (1960) 383

Jo61 JOHANSSON A., SVANBERG U., HODGSON P.E., Arkiv Fysik 19 (1961) 541

Jo61a JOHANSSON A., et al, Arkiv Fysik 19 (1961) 527

Jo67 JOHANSSON A., Phys. Lett. 24B (1967) 29

Ke42 KEESOM W.H., "Helium", Elsevier Publishing Co., Amsterdam (1942)

Ke66 KERR R.G., Phys. Rev. 148 (1966) 998

Ki65 KIRKBY P., Ph D. Thesis, McGill University 1965 (Unpublished)

Ki66 KIM C.C., BUNCH S.M., DEVINS D.W., FORSTER H.H., Phys. Lett. 22 (1966) 314

Ko59 KOMAROV V.V., NEUDACHIN V.G., POPOVA A.M., TEPLOV I.B., JETP (Soviet Phys.) 8 (1959) 679

Ko65 KOEHLER A.M., MEASDAY D.F., MORRILL D.H., Nucl. Instr. & Meth. 33 (1965) 341

Ku56 KURATH D., Phys. Rev. 101 (1956) 217

Ku67 KULL L.A. (1967) preprint.

La66 LAURITSEN T., AJZENBERG-SELOVE F., Nucl. Phys. 78 (1966) 1

Le58 LEVINSON C.A., BANERJEE M.K. Ann. Phys. 3 (1958) 67

Le65 LEE J.K.P. Ph D. Thesis, McGill University, 1965 (Unpublished)

Li55 LIKELY J.G., Phys. Rev. 98 (1955) 1538 A

Ma57 MAXSON D.R., BENNET E.F., Bull Am. Phys. Soc. 2 (1957) 180

Ma65 MARK S.K., Ph D. Thesis McGill University, 1965 (Unpublished)

Ma66 MARK S.K., PORTNER P.M., MOORE R.B., Can. J. Phys. 44 (1966) 2961

Ma66a MARK S.K., MOORE R.B., Nucl. Instr. & Meth. 44 (1966) 93

Me56 MESHKOV S., UFFORD C.W., Phys. Rev. 101, (1956) 734

Me59 MEYER-BERKHOUT U., FORD K.W., GREEN A.E.S., Ann. Phys. 8 (1959) 119

Me65 MEASDAY D.F., Nucl. Instr. & Meth. 34 (1965) 353

Me66 MEASDAY D.F., SCHNEIDER R.J., Nucl. Inst. & Meth. 42 (1966) 26

Mf65 MEYERHOF W.E., MCELEARNEY J.N., Nucl. Phys. 74 (1965) 533

Mh66 MAHALANABIS J., JACKSON D.F., Proc. Phys. Soc. 87 (1966) 677

Mi55 MIGDAL A.B., JETP (Soviet Phys.) 1 (1955) 2

Mo64 MONTELATICI V., Nucl. Instr. & Meth. 29 (1964) 121

Ne62 NEWTON D., CLEGG A.B., SALMON G.L., FISHER P.S., FOLEY K.J., Proc. Phys. Soc. 79 (1962) 27

Oe67 OERS W.T.H. van, SLAUS I., Phys. Rev. 160 (1967) 853

On61 ONNO P., Rev. Sci. Instr. 32 (1961) 1253

Pa58 PALMIERI J.N., CORMACK A.M., RAMSEY N.F., WILSON R., Ann. Phys. 5 (1958) 299

Pa65 PARKER P.D., DONOVAN P.F., KANE J.V., MOLLENAUER J.F., Phys. Rev. Lett. 14 (1965) 15

Pe61 PENNER S., Rev. Sci Instr. 32 (1961) 150

Po61 POSTMA H., WILSON R., Phys. Rev., 121 (1961) 1229

Po64 PORTNER P.M., M.Sc. Thesis, McGill University, 1964 (Unpublished)

Po67 PORTNER P.M., MOORE R.B., Bull. Am. Phys. Soc. 12 (1967) 632

Ri61 RITSON D.M., ed. "Techniques of High Energy Physics", Interscience publishers Inc., (N.Y.) 1961 p 348

Ru62 RUHLA C., RIOU M., GARRON J.P., JACMART J.C., MASSONET L., Phys. Lett. 2 (1962) 44

Sa64 SATCHLER G.R., HAYBRON R.M., Phys. Lett. 11 (1964) 313

Sa64a SATCHLER G.R., Nucl. Phys. 55 (1964) 1

Sa67 SATCHLER G.R., Nucl. Phys. A92 (1967) 273

Se47 SERBER R., Phys. Rev. 72 (1947) 1114

Se56 SELOVE W., Phys. Rev. 101 (1956) 231

Se58 SELOVE W., TEEM J.M., Phys. Rev. 112 (1958) 1658

Sh60 SHELINE R.K., WILDERMUTH K., Nucl. Phys. 21 (1960) 196

Sl67 SLOBODRIAN R.J., MCKEE J.S.C., TIVOL W.F., CLARK D.J., TOMBRELLO. T.A., Phys Lett. 25B (1967) 19

St55 STREIB J.F., Phys. Rev. 100 (1955) 1797

St56 STRAUCH K., TITUS F., Phys. Rev. 103 (1956) 200

Su67 SUELZLE L.R., YEARIAN M.R., CRANNELL H., Phys. Rev. 162 (1967) 992

Ta62 TANG Y.C., WILDERMUTH K.W., PEARLSTEIN L.D., Nucl. Phys. 32 (1962) 504

Ta64 TATISCHEFF B., MARTY N., DE BOUARD X., FOX J.G., GEOFFRION B., ROLLAND C., Phys. Lett. 8 (1964) 54

Th67 THOMSON D.R., TANG Y.C., Phys. Rev. Lett. 19 (1967) 87

Ti62 TIBELL G., SUNDBERG O., MIKLAVIZIC U., Phys. Let. 1 (1962) 172

To61 TOBOCMAN W., "Theory of Direct Nuclear Reactions" Oxford Univ. Press. (1961) p 1

To65 TOMBRELLO T.A., BACHER A.D., SPIGER R.J., Bull. Am. Phys. Soc. 10 (1965) 423

To65a TOMBRELLO T.A., BACHER A.D., Phys. Lett. 17 (1965) 37

To65b TOMBRELLO T.A., Phys. Rev. 138 (1965) B40

Ty58 TYREN H., MARIS TH. A.J., Nucl. Phys. 6 (1958) 82

Wa52 WATSON K.M., Phys. Rev. 88 (1952) 1163

Wi66 WILLIAMS L.E., Phys. Rev. 144 (1966) 815

APPENDIX I:

Momentum Selection with a Wedge Magnet:

The following section presents a summary of the treatment given by Lee (Le65) for the operation of the magnet analyser.

For a uniform field sector magnet with normal entry and exit pole faces (see Fig. A1), using transfer matrix theory of beam optics (Pe61) it can be shown that (including second order correction for momentum deviation):

$$\begin{bmatrix} x \\ \phi \\ \Delta p/p \end{bmatrix} = \begin{bmatrix} 1 & L & 0 \\ 0 & 1 & 0 \\ 0 & 0 & 1 \end{bmatrix} \begin{bmatrix} \cos\theta & \rho\sin\theta & \rho(1-\cos\theta) \\ -\sin\theta/\rho & \cos\theta & \dfrac{\sin\theta}{(1-\Delta p/p)} \\ 0 & 0 & 1 \end{bmatrix} \begin{bmatrix} 1 & L_o & 0 \\ 0 & 1 & 0 \\ 0 & 0 & 1 \end{bmatrix} \begin{bmatrix} x_o \\ \phi_o \\ \Delta p/p \end{bmatrix}$$

where the quantities are defined as follows:

x_o, ϕ_o, $\Delta p/p$ are the co-ordinatesof a trajectory from the target;being the displacement, angular divergence and momentum deviation from the central path respectively.

x, ϕ, $\Delta p/p$ are similar co-ordinates for the trajectory at the detector.

L_o and L are the distances to the effective pole face edges on the target and detector sides respectively.

θ is the deflection angle of the central path (which makes normal exit and entry).

ρ is the radius of curvature of the central path.

At a distance L_s from the target centre, in front of the entrance pole face (see Fig. A1) the displacement x_s of the trajectory described above is given by:

$$x_s = x_o + 0_o L_s$$

For fixed geometry the displacement x_s is a function of x_o, x, and $\Delta p/p$. (This can be seen by eliminating ϕ_o from the definition of x_s and the matrix equation above). This can be represented by $x_s(x_o, x, \Delta p/p)$. If the source size (beam spot size)extends from x_{omin} to x_{omax} (as shown in the figure) and the image size, which is limited by the detector dimensions, extends from x_{min} to x_{max}; the quantities S_{max} and S_{min} can be defined as follows:

$$S_{max}(\Delta p/p) = x_s(x_{omax}, x_{max}, \Delta p/p)$$

$$S_{min}(\Delta p/p) = x_s(x_{omin}, x_{min}, \Delta p/p)$$

Particles with a given momentum deviation $\Delta p/p$ which originate from the beam spot (i.e. $x_{omin} \leq x \leq x_{omax}$) and reach the detector (i.e. $x_{min} \leq x \leq x_{max}$) must satisfy the condition:

$$S_{min} \leq x_s \leq S_{max}$$

If a slit is now placed perpendicular to and centered on the central path at a distance L_s from the target, it can be seen that a range of magnetic rigidities transmitted from the target to the detector will so be defined. To obtain the magnet momentum selection characteristics, $S_{min}(\Delta p/p)$ and $S_{max}(\Delta p/p)$ are calculated for a range of values of $\Delta p/p$ using the geometrical constants appropriate to the physical set-up. A plot of these quantities as a function of $\Delta p/p$ is shown in fig. 5 of Chapter 2 (calculated using the more exact method described in Appendix II). The regions of $\Delta p/p$ which are fully transmitted and partially transmitted are evident in the figure.

APPENDIX II:

Improved Calculations of Momentum Selection Characteristics:

This section presents the modifications to the treatment given in Appendix I, so as to include the fringing field effects.

The matrix equation given in Appendix I and representing a drift space followed by a region of uniform magnetic field, followed again by a drift space (target to detector) is here replaced by the matrix equation:

$$\begin{bmatrix} x \\ \phi \\ \Delta p/p \end{bmatrix} = [M_{15}][M_{14}] \ldots\ldots [M_1] \begin{bmatrix} x_o \\ \phi_o \\ \Delta p/p \end{bmatrix}$$

where the matrices M_1 to M_{15} represent the transfer matrices obtained from the field shape as described in chapter 2 and illustrated in fig. 4. The product $M_{15}\ M_{14} \cdots M_1$ is the total effective transfer matrix for the path from the target to the detector. The equation defining the displacement x_s is replaced here by:

$$\begin{bmatrix} x_s \\ \phi_s \\ \Delta p/p \end{bmatrix} = [M_6][M_5] \ldots\ldots\ldots [M_1] \begin{bmatrix} x_o \\ \phi_o \\ \Delta p/p \end{bmatrix}$$

The function $x_s(x_o, x, \Delta p/p)$ is then obtained by solving the above two matrix equations for x_s. S_{max} and S_{min} are then obtained as previously described in Appendix I. These calculations were performed using the McGill IBM 7044 computer and a comprehensive set of tables obtained for the magnet properties. Typical momentum selection characteristics for the.magnet-slit combination are shown in fig. 5 of Chapter 2.

FIGURE A 1

ANALYSER MAGNET GEOMETRY

FIGURE A-1

This diagram shows, schematically, the geometric details used in the magnet analysis.

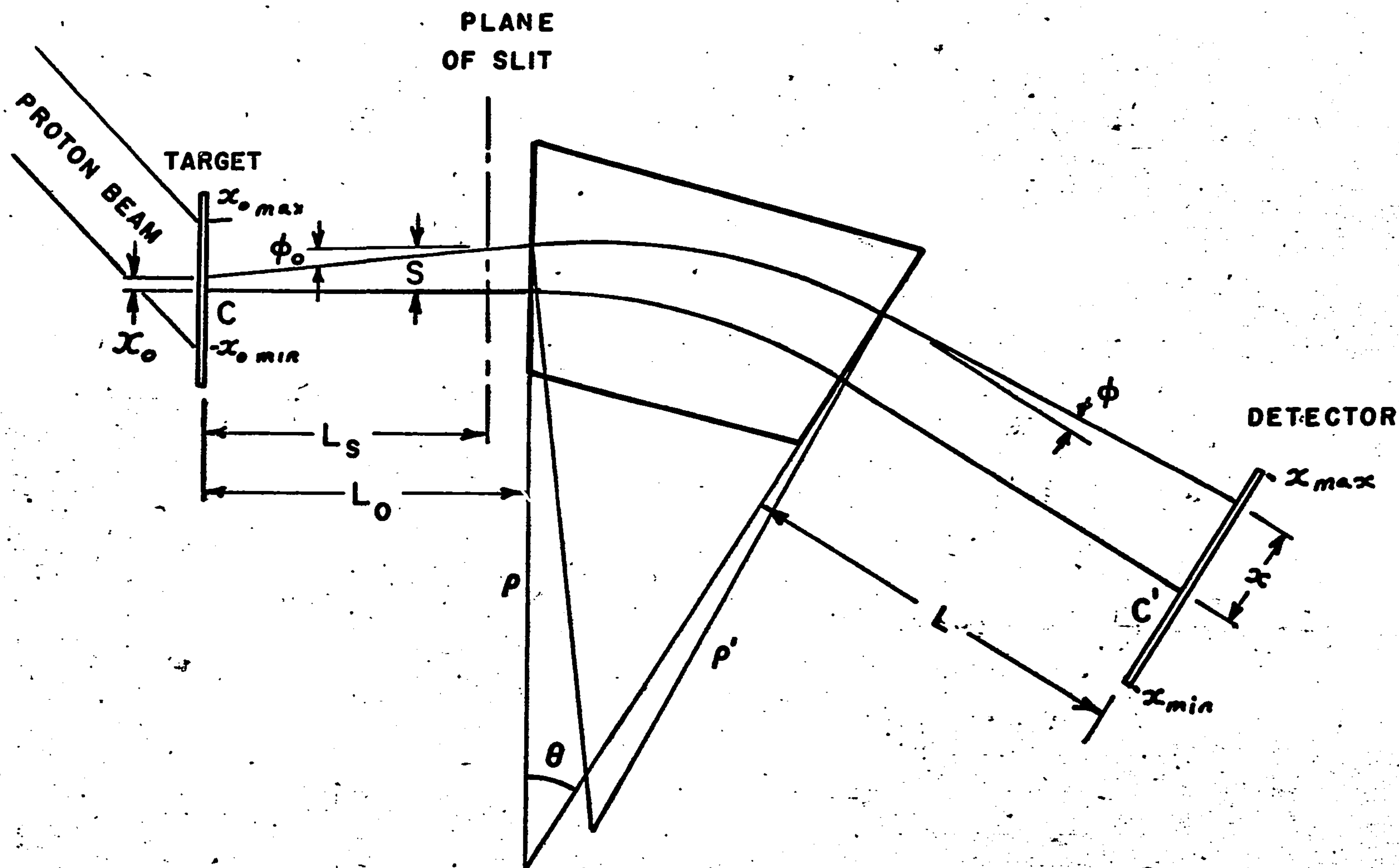

PLANE
OF SLIT
PROTON BEAM
TARGET
$x_{o\,max}$
ϕ_o
S
C
x_o
$-x_{o\,min}$
L_S
L_O
ρ
θ
ρ'
ϕ
DETECTOR
x_{max}
x
C'
L
x_{min}